Experimental Studies of Spin, Charge and Orbital Order at Extreme Conditions

Sandra J. E. Carlsson

For the degree of Doctor of Philosophy
School of Chemistry
University of Edinburgh

June 2008

Abstract

Spin, charge and orbital ordering in various crystalline compounds have been studied under extreme conditions. The main techniques used were synchrotron X-ray and neutron powder diffraction. High-pressure conditions were obtained by using a diamond anvil cell and the Paris-Edinburgh cell.

Changes in the valence state of $BiNiO_3$ perovskite under pressure have been investigated by a neutron powder diffraction study and bond valence sum (BVS) calculations. At ambient pressure, $BiNiO_3$ has the unusual charge distribution $Bi^{3+}_{0.5}Bi^{5+}_{0.5}Ni^{2+}O_3$ with ordering of Bi^{3+} and Bi^{5+} charges on the A sites of a highly distorted perovskite structure. High pressure neutron diffraction measurements show that the pressure-induced melting of the charge disproportionated state leads to a simultaneous charge transfer from Ni to Bi, so that the high pressure phase is metallic $Bi^{3+}Ni^{3+}O_3$. This exceptional charge transfer between A and B site cations coupled to electronic instabilities at both sites gives rise to a remarkable variety of ground states. Furthermore, Rietveld analysis of low temperature neutron powder diffraction data shows that the structure of $BiNiO_3$ remains triclinic (space group $P\bar{1}$) throughout the temperature range 5 to 300 K. BVS calculations confirm that the charge distribution is $Bi^{3+}_{0.5}Bi^{5+}_{0.5}Ni^{2+}O_3$ down to 5 K. The magnetic cell is identical to that of the triclinic superstructure and a G-type antiferromagnetic model gives a good fit to the magnetic intensities, with an ordered Ni^{2+} moment of 1.76(3) μ_B at 5 K. However, $BiNiO_3$ is ferrimagnetic due to the inexact cancellation of opposing, inequivalent moments in the low symmetry cell.

The effect of high pressure on the structural properties of $(EDT\text{-}TTF\text{-}CONH_2)_6[Re_6Se_8(CN)_6]$, a conducting, molecular, mixed-valence, π-conjugated radical, cation salt has been examined using synchrotron X-ray diffraction and a diamond anvil cell set-up. It has previously been shown that this compound undergoes a low temperature phase transition from a rhombohedral (space group $R\bar{3}$) to a triclinic (space group $P\bar{1}$) structure at ~150 K. This transition is caused by a charge ordering. A LeBail profile fitting of powder diffraction data revealed a change in compressibility at 0.7 GPa indicative of a phase transition. This was confirmed by single crystal data which showed that the structure remains rhombohedral $(R\bar{3})$, up

to 0.4 GPa but is triclinic ($P\bar{1}$) at 0.8, 1.2 and 1.8 GPa. Hence, high pressure, as well as low temperature, can drive the charge ordering in (EDT-TTF-$CONH_2$)$_6$[$Re_6Se_8(CN)_6$]. The transition pressure is between 0.5-0.7 GPa at 300 K.

The crystal and magnetic structures of the orbitally ordered perovskite $KCrF_3$ have been determined from neutron powder diffraction measurement at temperatures from 3.5 to 300 K. A phase transition from a tetragonal to a monoclinic structure occurs at 250 K but the orbital ordering is sustained. Long range antiferromagnetic order of the A-type occurs below T_N = 46 K and the refined magnetic moment for the Cr^{2+} sites was found to be 4.39(7) μ_B.

Declaration

I declare that this thesis was composed by myself and that the work detailed herein is my own, except where otherwise stated, and no part of it has been submitted for any other degree or professional qualification. Prior to submission of this thesis some work has been published as listed in Appendix C.

Sandra J. E. Carlsson

Acknowledgements

I would like to thank everyone who helped me throughout the course of this PhD. First and foremost, Professor Paul Attfield for being such a supportive and enthusiastic supervisor.

The Attfield group members past and present: in particular Tony and Luis for teaching me everything I know about GSAS, Jenny for reading this thesis, Wei-Tin, George, Simon, Richard, Falak, Jan-Willem and everyone else for all their advice and making the last four years so enjoyable.

I'm very grateful to Dr. Dave Allan and Dr. Iain Oswald for their help with the single-crystal data collection and refinements, and also Dr. Alan Hewat, Dr. Matt Tucker and Dr. John Warren for providing help with data collection at the ILL, ISIS and Daresbury respectively.

Thanks to my collaborators: Professor M. Azuma, Dr P. Batail and Dr S. Margadonna for giving me the opportunity to work on such interesting compounds.

I also acknowledge the University of Edinburgh for providing me with funding for this PhD.

Last but most importantly: Gaétan, Sofia, mamma, pappa and mormor, I can't thank you enough for your affection and encouragement and for always being there for me. I couldn't have done it without you!

Contents

Chapter 1

Introduction

The chemistry and most properties of both inorganic and organic crystalline solids are strongly dependent on their structure. It is therefore important to have accurate knowledge of the atomic arrangement in order to gain a correct understanding of the physical properties exhibited by solid materials. In the solid state, all crystalline materials adopt a regular arrangement of atoms or ions in space, with the smallest repeating unit that shows the full symmetry defined as the *unit cell*. The unit cell contains the basis set of atoms and pack together following the *crystal lattice* to completely fill space. The distribution of atoms or ions and electrons in the crystal lattice and the coupling between them can give rise to various forms of long-range order, all of which will have an effect on the physical properties. For example, in transition metal compounds, numerous different couplings are possible between the charge on the metal ions, their *d* orbital occupancy and *d* electron spins (magnetic moment). Long range ordering may occur for some or all of these parameters generating charge, orbital or magnetic ordering.

1.1 Charge, orbital and spin ordering

In this work, it is intended to study charge and spin (magnetic) order and how these properties are affected by pressure. However, both charge and spin order are closely coupled to orbital ordering and so this also needs to be taken into consideration in some cases. An overview of the various types of ordering phenomena and examples of interesting and important materials that exhibit these effects will be given here. A more detailed description of the materials studied in this thesis and their related compounds is to be found at the beginning of each experimental chapter.

1.1.1 Charge order

Charge ordering is a phenomenon where electrons are arranged periodically in a crystal lattice. It is often found in transition metal compounds, as well as organic conductors and has major effect on the electronic properties. At the transition to the low temperature charge ordered state, the material becomes insulating or semiconducting as the resistivity is increased and the crystallographic symmetry is usually broken.

1.1.1.1 Transition metal compounds

For transition metal compounds, charge ordering means the long range order of different metal valence states in the crystal lattice. Above the charge ordering transition temperature, T_{CO}, only one crystallographic metal site with an average charge state exists. Below the $T_{CO,}$ two different charge ordering schemes can be considered. Firstly, ordering of delocalised electrons from semi-valent cations:

$$(La_{0.5}Ca_{0.5})Mn^{3.5+}O_3 \rightarrow (La_{0.5}Ca_{0.5})(Mn^{3+}{}_{0.5}Mn^{4+}{}_{0.5})O_3 \text{ [1, 2]}$$

And secondly, valence disproportionation from an unstable oxidation state to two more stable oxidation states:

$$BaBi^{4+}O_3 \rightarrow Ba(Bi^{3+}{}_{0.5}Bi^{5+}{}_{0.5})O_3 \text{ [3]}$$

The idea of charge ordering in solids was first visualised in the late 1930s by Eugene Wigner[4] and shortly after E. J. W. Verwey applied the phenomenon to the transition that occurs in magnetite (Fe_3O_4) at 120 K, the so called Verwey transition[5, 6]. Magnetite is a ferrimagnet with moderate electrical conductivity and an inverse spinel type crystal structure. The formula is written as $Fe^{3+}[Fe^{2+}Fe^{3+}]O_4$ to distinguish between the first (A type) tetrahedrally coordinated Fe^{3+} and the second (B type) site with octrahedral coordination occupied by the Fe^{2+} and Fe^{3+} ions. On cooling below ~120 K, magnetite undergoes a first order transition at which there is a sharp significant increase in the resistivity and a structural distortion form the cubic symmetry[6]. Verwey proposed that below the transition temperature, the electrons on the Fe^{2+} and Fe^{3+} ions are ordered over the octrahedral sites, or B sublattice, and an orthorhombic superstructure model was suggested[5]. However, 60 years of research later, Verwey's original charge-ordering theory is still very much debated.

Whilst some argue that results from Synchrotron X-ray and neutron diffraction studies provide direct evidence for charge ordering[7, 8], supported by NMR data[9], others claim that clear proof for distinct Fe^{2+} and Fe^{3+} charge states have never been found [10, 11].

The importance of charge order has lately increased following the intense research on doped manganite perovskites, $T_{1-x}D_xMnO_3$, where T is a trivalent rare earth cation (e.g. La, Pr, Nd, Sm) and D is a divalent cation (e.g. alkaline-earth Ca, Sr, Ba). These compounds attract much interest as they can have many different ground states and exhibit colossal magnetoresistance[12, 13]. The several magnetic structures displayed by manganites were determined in 1955[14] and considering this work, Goodenough proposed the existence of charge and orbital order[1]. In several half doped materials such as $La_{0.5}Ca_{0.5}MnO_3$[2] and $Pr_{0.5}Ca_{0.5}MnO_3$[15] the localised Mn^{3+} and Mn^{4+} states are ordered in alternate "chessboard" planes directly above each other forming a "striped" model as illustrated in Figure 1.1. There have also been observations of charge ordered stripes in the cuprates and it has been proposed that the high T_c superconductivity in these compounds is related to dynamic fluctuations of disordered charge stripes[16, 17]. Evidence of charge ordering has also been seen in the half-doped $RBaMn_2O_6$ (R = Sm, Y and Tb) series where the ordering occurs on the A-site with the R^{3+} and Ba^{2+} cations arranged in alternating [001] perovskites layers[18-20]. However, the charge order model in manganites is disputed and some studies suggests that the difference between the manganese charge or magnetic moment on different sites is very small and also that a different model is needed to understand the physics of these systems[21-23].

When the manganese is substituted by other metals as in $YBaMn_2O_5$[24], $TbBaFe_2O_5$[25] and $YBaCo_2O_5$ [26] a charge ordered state is still present. For all of the above compounds the charge ordering occurs within a simple cubic lattice but it can also be present in materials with more complicated structures such as the spinel in Fe_3O_4 mentioned earlier or layered oxides. One example is $Na_{0.5}CoO_2$[27], which has been widely studied because the related material $Na_{0.35}CoO_2 \cdot 1.3H_2O$ is a superconductor[28].

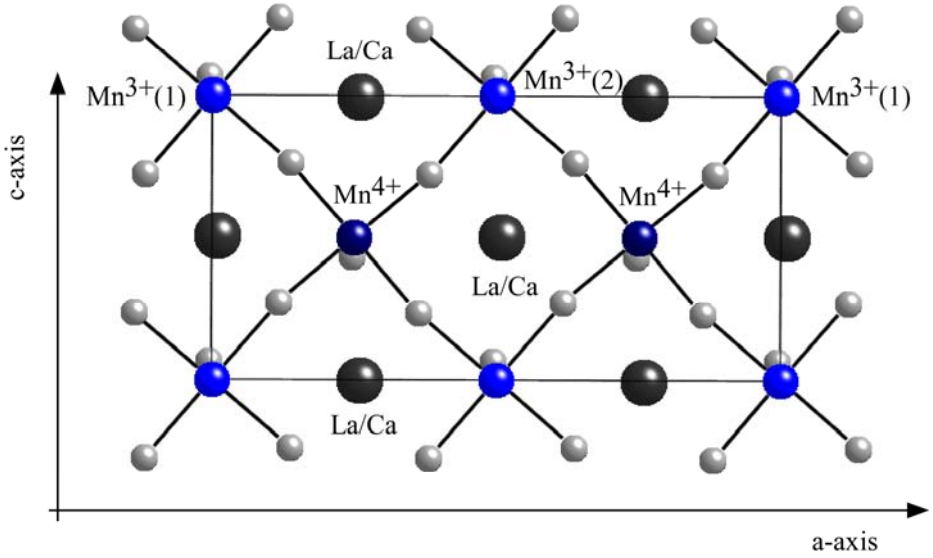

Figure 1.1 The striped charge ordered model found in $La_{0.5}Ca_{0.5}MnO_3$ and other half doped manganites where the Mn3+ and Mn4+ are ordered in alternating layers along the *c* direction.

Charge ordering of the valence disproportionation type, as explained above, is seen in many undoped perovskites such as the nickelates $RNiO_3$ (R = Pr, Nd, Sm, Eu)[29], $CaFeO_3$[30], and $BaBiO_3$[3]. In the latter, the charge ordering can be broken by K or Pb doping and superconducting properties are induced[31, 32].

To obtain evidence of long range charge order (CO), a reliable structure determination is essential and hence, high resolution diffraction data is needed to determine correct CO structures. The lattice distortions that occur at the CO transition are often subtle and the problem of micro twinning in many materials makes single crystal studies difficult. Most structure determinations are therefore based on neutron powder diffraction experiments which also offer the benefit of higher sensitivity to oxygen positions. Performing a joint refinement of X-ray and neutron powder diffraction data combines the advantages of the two techniques and can be used to resolve complex CO structures[33]. Bond valence sum (BVS) calculations based on the metal-oxygen bond lengths can be used to identify the oxidation states of the metal ions on different crystallographic sites.

It should be noted that the degree of charge ordering observed in transition metals, as calculated from BVS's, is never 100%. Many materials have 20-60% CO and although the difficulties in resolving the CO structures may be responsible for part of the reduction from the ideal values, other underlying physical causes are likely[7].

There are also other techniques available for studying charge ordered material such as Mossbauer spectroscopy[34], NMR[35] and resonant X-ray diffraction[36]. The latter technique can be used as a direct probe for determining the valence in a particular compound utilising a wavelength at or near the absorption edge where different oxidation states scatter differently.

1.1.1.2 Organic conductors

In molecular crystals, such as those of organic conductors, where there are several identical molecules in a unit cell, charge ordering phenomena can be expected to exist if the molecules are positioned and arranged in different non-equivalent sites. This type of charge ordering is often referred to as charge disproportionation[37] and is a manifestation of the strong Coulomb interaction between the conducting electrons[38, 39]. The most extensively studied organic conductors are 2:1 cation radical salts, such as $(TMTCF)_2X$ and $(BEDT\text{-}TTF)_2X$. Since the anion is monovalent, X^-, in these compounds, the averaged valence of the organic molecule becomes + ½ and the resulting π-band is quarter-filled for holes[39]. In other compounds, such as $(DCNQI)_2Ag$, the valence of the organic molecule is -½ so that the π-band is quarter filled in terms of electrons. For both types of compound, a metal to insulator (MI) transition is often observed as the temperature is lowered. The transition to the insulating phase may occur as a consequence of dimerisation, a so called Mott-Hubbard type insulating state, where the holes are localised and shared between two molecules forming a dimer (Figure1.2(a)). It can also occur due to charge disproportionation between the organic molecules resulting in two inequivalent molecules with unequal electron densities, as shown in Figure 1.2(b), below a charge-ordering temperature T_{CO}[40].

The charge disproportionation in organic compounds can be investigated using C-NMR Spectroscopy [41], IR absorption experiments, as well as bond length analysis[39]. However, it is still difficult to determine the pattern of charge disproportionation in some materials.

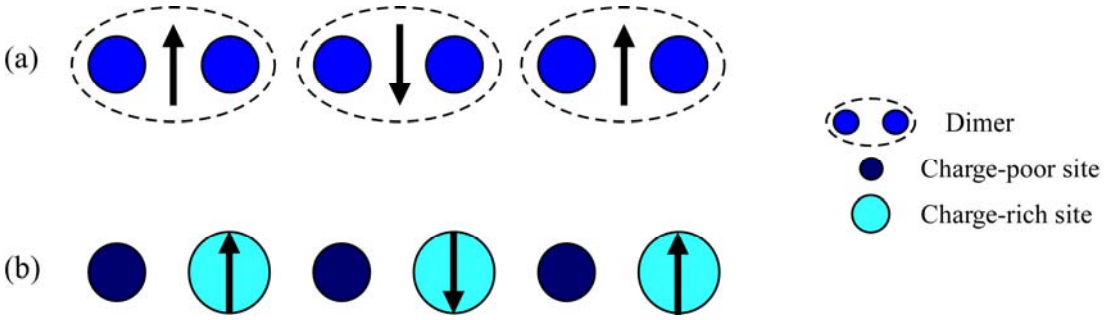

Figure 1.2 Schematical representation of the dimerised insulating state (a) and the charge disproportionated state (b) with the arrows indicating the spin moments in an antiferromagnetically ordered phase. N.B. The magnetic moments may be located on either the charge rich or charge poor sites.

1.1.2 Orbital order

In transition-metal complexes, the *d* orbitals are not degenerate but are split into groups of different energies by the surrounding ligands. The energy ordering of the split *d* orbitals is decided by the ligand geometry. For example, in an octahedral crystal field, the *d* orbitals are split into two groups, three orbitals are contained in the t_{2g} set which is lower in energy than the two orbitals in the e_g set as shown in Figure 1.3(a). The three t_{2g} orbitals (d_{xy}, d_{xz}, d_{yz}) do not point in the direction of the ligands and form π anti-bonding combinations whereas the two e_g orbitals, d_{z^2} and $d_{x^2-y^2}$, form σ bonds as they point directly towards the ligands. Because σ interactions are stronger the e_g pair are higher in energy. In accordance with Hund's rule,

electrons will, if possible, singly occupy orbitals. Hence, for the d^4 to d^7 atoms or ions there are two possible configurations, the low spin (LS) or high spin (HS) state, illustrated in Figure 1.3(b) and (c). Which one occurs depends on the metal (in particular to which row it belongs) and the strength of the ligand field. The high spin configuration is observed mainly in 3*d*-metals and in the presence of weak field ligands or anions.

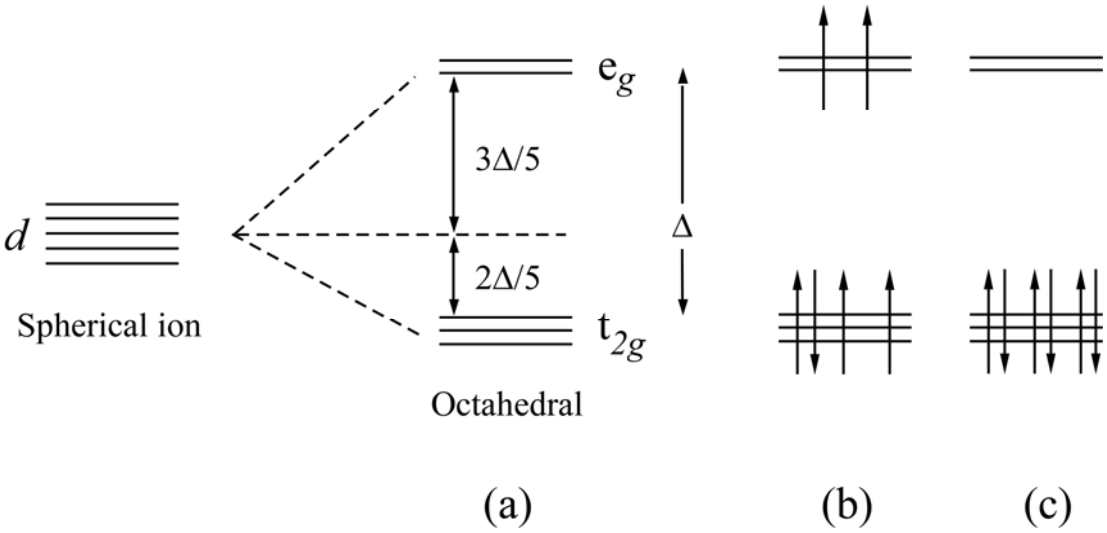

Figure 1.3 The splitting of energy levels in an octahedral environment (a) and the electron configurations of the high-spin (b) and low-spin (c) states for a d^6 transition metal ion.

Orbital ordering (OO) can arise when a set of degenerate orbitals are unevenly occupied by electrons. These systems are unstable due to the unsymmetrical charge distribution and at low temperatures a distortion of the local coordination is induced which lifts the orbital degeneracy[43]. This is referred to as the Jahn-Teller (JT) effect[44] and is usually accompanied by a lowering in the lattice symmetry often in the form of a structural phase transition, associated with, or brought on by, the orbital ordering.

In transition metal compounds with octahedral geometries, orbital ordering can occur when the t_{2g} or the e_g orbitals are partially filled, but the JT effect is usually much more pronounced with the latter. The distortion normally involves a tetrahedral lengthening of the octahedron resulting in two long bonds and four short ones and the splitting of the t_{2g} or e_g levels [45] as in Figure 1.4.

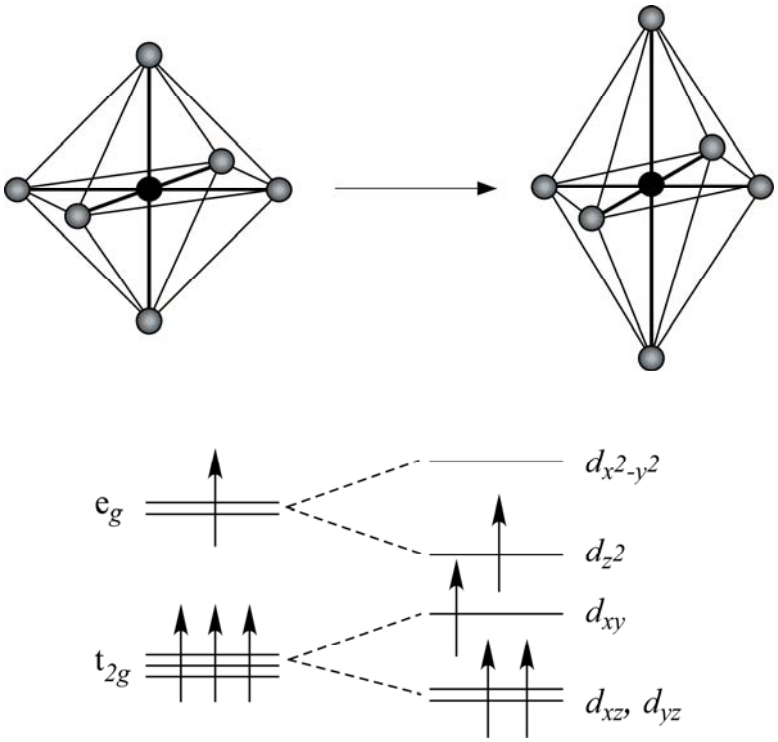

Figure 1.4 The Jahn-Teller distortion of an octahedral complex and the associated splitting of the t_{2g} and e_g relevant to a d^4 ion, e.g. Cr^{2+}.

Typical examples of transition metal ions with strong Jahn-Teller effects are $Cr^{2+}(d^4)$, $Mn^{3+}(d^4)$, $Cu^{2+}(d^9)$ and low spin $Ni^{3+}(d^7)$ etc. JT distortions are also observed in ions where only the t_{2g} orbitals are occupied such as $Ti^{3+}(d^1)$ and $V^{3+}(d^2)$ but are much more difficult to detect. In solid state systems, the distortions around each ion will be orientated to fit into the crystal lattice, leading to so called cooperative Jahn-Teller distortions and long range orbital ordering. An example of this is seen in the perovskites $LaMnO_3$[1] and $KCuF_3$[46] which contain $Mn^{3+}\left(t_{2g}^3 e_g^1\right)$ or Cu^{2+} $\left(t_{2g}^6 e_g^3\right)$ ions at every lattice site forming simple cubic lattices. Figure 1.5 depicts examples of orbital ordering patterns observed in $LaMnO_3$ and other perovskites. Layered materials such as the cuprate K_2CuF_4[47] and the chromite Rb_2CrCl_4[48] have a packing of local distortions corresponding to an alternating pattern of the empty (hole) orbitals $d_{y^2-z^2}$ and $d_{x^2-z^2}$ [49] in what can be described as antiferro-ordering meaning an equal number of orbitals point in perpendicular directions. However, in other layered systems, ferro-orbital ordering

occurs, i.e. the orbitals are aligned parallel, exemplified by the $d_{x^2-z^2}$ ordering in La_2CuO_4[50] and the Mn^{3+} d_{z^2} order in the charge ordered $La_{1-x}Sr_{1+x}MnO_4$[49]. Orbital order also occurs in charge ordered systems such as $La_{0.5}Ca_{0.5}MnO_3$[2] and $Pr_{0.5}Ca_{0.5}MnO_3$[7]. An illustration of the charge and orbital ordering that occur in most half-doped manganites are shown in Figure 1.6. The ordering is of the C-E type[51], normally used for describing antiferromagnetic ordering, but is also applied to denote the related charge and orbital structures. Other complex patterns of orbital ordering has been shown to exist in the spinels, for example $MgTi_2O_4$ and $CuIr_2O_4$[52].

Orbital ordering can be described much in the same way as magnetic (spin) ordering (Section 1.1.3) in that the orbitals align parallel or antiparallel to each other in chains or planes etc. The way in which the orbitals are occupied and hence ordered, has a profound effect on the magnetic properties of a material as explained by the Goodenough-Kanamori rules[1, 53, 54]. Therefore, states with different orbital order have very different magnetic behaviour as observed in $Pr(Sr_{0.1}Ca_{0.}9)Mn_2O_7$[55]. Other interesting effects are demonstrated in the materials $LaVO_3$[56] and YVO_3[57] where the change of orbital ordering is associated with temperature-induced magnetisation reversals[58].

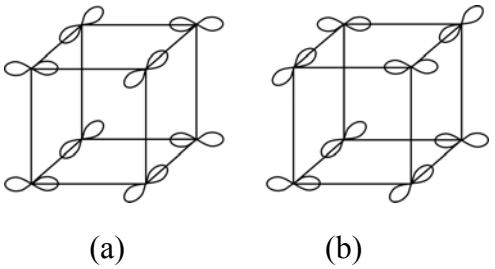

Figure 1.5 Two different types of orbital ordering in cubic manganites: (a) in-phase and (b) out of phase stacking of antiferro-ordered planes in the *c*-direction.

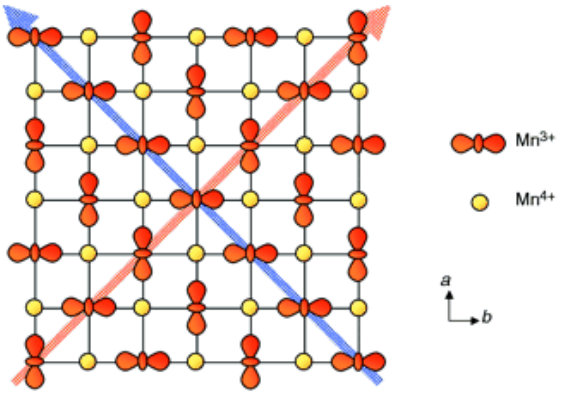

Figure 1.6 Charge and orbital orderings in the half doped manganites e.g. $La_{0.5}Sr_{0.5}MnO_4$ displaying the so-called CE structure with direction of the ferro- and antiferro-distortive ordering indicated by blue and red arrows respectively[59].

The most common way of studying long-range orbital order is by comparing the metal-oxygen bond lengths from the structural model obtained from diffraction experiments (X-ray or neutron). By looking for the pattern of elongated metal-oxygen bonds, the Jahn-Teller distortions can be identified and a model of orbital ordering constructed. It is also possible to observe orbital order (both short and long range) using the techniques resonant X-ray diffraction and X-ray absorption spectroscopy.

1.1.3 Spin (magnetic) order

An inorganic solid that shows magnetic behaviour other than diamagnetism, which is characteristic of all substances, must have unpaired electrons present. As these are normally situated on metal cations, magnetic effects are mainly limited to compounds containing transition metals or lanthanides. Most of these elements have partially filled *d*- and *f*-orbitals, respectively. The magnetic moment of an atom or ion in free space arises from both the spin and the orbital motion of the unpaired electrons and is given by:

$$\mu_J = -g_J \mu_B J \qquad (1.1)$$

where the total angular momentum, J, is the sum of the spin, S, and the orbital, L, angular momenta, μ_B is the Bohr magneton $(e\hbar / 2m)$ and g_J is the gyromagnetic ratio:

$$g_J = \frac{3}{2} + \frac{S(S+1) - L(L+1)}{2J(J+1)} \qquad (1.2)$$

When the unpaired electrons are oriented at random on the different atoms, the associated magnetic field is known as paramagnetism and partial alignment of the moments will occur only under the application of a magnetic field. However, cooperative magnetic phenomena can occur in solid materials when there is interaction between the unpaired electrons, resulting in alignment of electron spins. If these spins are aligned parallel, the material will have an overall magnetic moment and is described as ferromagnetic. The moments on the neighbouring atoms can also align antiparallel to each other giving rise to antiferromagnetic behaviour with zero overall magnetic moment. In solids that contain more than one type of magnetic ions

other types of magnetic ordering can be found such as ferrimagnetism, where the magnetic moments are aligned antiparallel but with unequal magnitude in the two directions resulting in a net magnetic moment.

1.1.3.1 Behaviour of a substance in a magnetic field

Applying a magnetic field to any substance will result in an induced magnetisation, M, proportional to the field, H:

$$M = \chi H \tag{1.3}$$

The magnetic susceptibility, χ, represents the response of a sample to an applied magnetic field. Diamagnetic materials are repulsed by a magnetic field and have a very small and negative values of χ. Superconductors are perfect diamagnets as a magnetic field is completely expelled by them and hence, χ has the value -1. For paramagnetic compounds χ is small and positive as they are attracted to magnetic fields. Antiferromagnets have a positive χ comparable to or less than paramagnets whereas in ferromagnetic substance, $\chi >> 1$.

The magnetic susceptibility is temperature dependant and many paramagnetic materials, where there is no spontaneous interaction between neighbouring unpaired electrons, follow the simple Curie law,

$$\chi = \frac{C}{T} \tag{1.4}$$

where T is the temperature and C is the Curie constant defined as:

$$C = \frac{N\mu_{eff}{}^2 \mu_B{}^2}{3k} \tag{1.5}$$

where N is Avogrado's number, k is the Boltzmann constant and μ_{eff} is the effective magnetic moment.

$$\mu_{eff} = g_J \sqrt{J(J+1)} \tag{1.6}$$

The local environment of an ion has a strong effect on the orbital component of the magnetic moment and for the first row transition metals the orbital angular momentum is normally quenched by crystal field effects[60]. Other factors such as

Jahn-Teller distortions can further reduce the orbital angular momentum. The effective magnetic moment can then be approximated using the spin only formula:

$$\mu_{eff} = g_J \sqrt{S(S+1)} \qquad (1.7)$$

This permits the determination of the number of unpaired spins on each cation from susceptibility measurements.

The Curie law is only valid for magnetic ions that are in effect isolated from each other but in most solids there is always some interaction between the ions and the magnetic properties are more complex. For ferro- and antiferromagnetic materials there is a temperature below which a transition takes place to a state where all the moments are aligned. This transition temperature is dependant on the material and is known as the Curie temperature, T_C for ferromagnets and results in a surge in the magnetic susceptibility as all the magnetic moments become aligned parallel to each other. Correspondingly, there is a decrease in the magnetic susceptibility for antiferromagnetic compounds at the Néel temperature, T_N because the moments line up antiparallel to one another. Above these transition temperature the behaviour is paramagnetic and can be described using a modification of Equation 1.1, the Curie-Weiss law:

$$\chi = \frac{C}{(T-\theta)} \qquad (1.8)$$

Where the Weiss constant, θ depends on the interactions between the magnetic moments and is negative for antiferromagnets and positive for ferromagnets. Figure 1.7 shows the variation of susceptibility with temperature for three different types of magnetic solids.

Numerous metals are paramagnetic but their susceptibility does not conform to the Curie-Weiss law. The paramagnetism in these materials arise from electrons contained in comparatively broad bands associated with the magnetic state and instead follows the Pauli susceptibility.

$$\chi = 2\mu_0 {\mu_B}^2 N(E_F) \qquad (1.9)$$

In contrast to the Curie-Weiss law, changes in temperature have almost no effect and Pauli paramagnetism is, whilst field dependent, essentially independent of temperature.

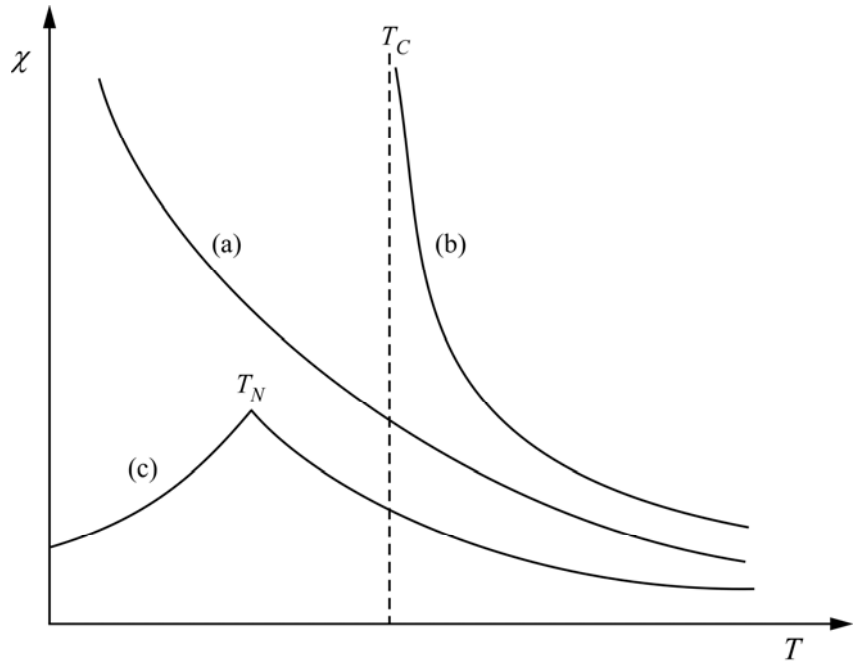

Figure 1.7 Variation of magnetic susceptibility with temperature for (a) paramagnetic, (b) ferromagnetic and (c) antiferromagnetic solids.

1.1.3.2 Exchange mechanisms

Long range magnetic order occurs at lower temperatures as a result of interactions between magnetic moments in the crystal lattice. The interactions between Heisenberg (isotropic) magnetic spins, S_i and S_j, can be expressed by the Hamiltonian:

$$H = -\sum_{i,j} J_{ij} S_i \times S_j \qquad (1.10)$$

where J_{ij} is the exchange constant. For ferromagnetic interactions, this parameter is positive and for antiferromagnetic interactions it is negative. The alignment of magnetic moments occurs spontaneously in the ferro- and antiferromagnetic states and there must therefore be some positive energy of interaction between neighbouring spins. Direct exchange relies on the overlap of the cation *d* orbitals as it

is a direct dipole-dipole interaction between magnetic moments. If there is significant orbital overlap an antiferromagnetic ground state will exist [61]. However, there is a critical minimum distance at which considerable overlap occurs and in non-metallic transition metal compounds the cations are too far apart for the direct exchange interactions to work. Instead, the long range magnetic order is formed via a superexchange mechanism[62], an indirect interaction dependant on the covalent bonding of the metal ions with their bridging anion ligands. It tends to promote antiferromagnetic ordering.

If the cation-anion-cation pathway has a linear bond angle of 180˚, as in Figure 1.8, then strongest interactions are predicted to be antiferromagnetic. An excited state is formed in which a double charge transfer occurs between the ligand and the metal sites with the net effect being that neighbouring metal ions are coupled antiparallel. However, the ferromagnetic ground state can be stabilised by superexchange when the cation-anion-cation pathway is at 90˚, illustrated in Figure 1.9, as a result of mutually orthogonal anion orbitals in the exchange pathway. After the double ligand to metal charge transfer, the ferromagnetic excited state on the orthogonal ligand orbitals is lower in energy than the antiferromagnetic exited state due to Hund's rule. Hence, the strength of the exchange coupling via a bridging ligand is highly dependant on the M-O-M bond angle. The crossover from antiferromagnetic to ferromagnetic superexchange occurs at ~96˚. In the presence of co-operative Jahn-Teller distortions, ferromagnetic alignment can exist via superexchange also in the case of a linear M-O-M array as shown in Figure 1.10. This is explained through the interaction of the bridging ligand with a half filled *d* orbital on one metal site and an empty orbital on the other. If the first cation has a spin up, there will be a net transfer of spin-up electron density to the empty orbital of the second atom. Due to spin correlation between the different orbitals in this second cation, the electron spin in an occupied orbital is driven to become parallel to that of the transferred density and hence parallel to the spin of the first metal ion. An example is the ferromagnetic interactions between neighbouring Cr^{2+} ions in Rb_2CrCl_4[48].

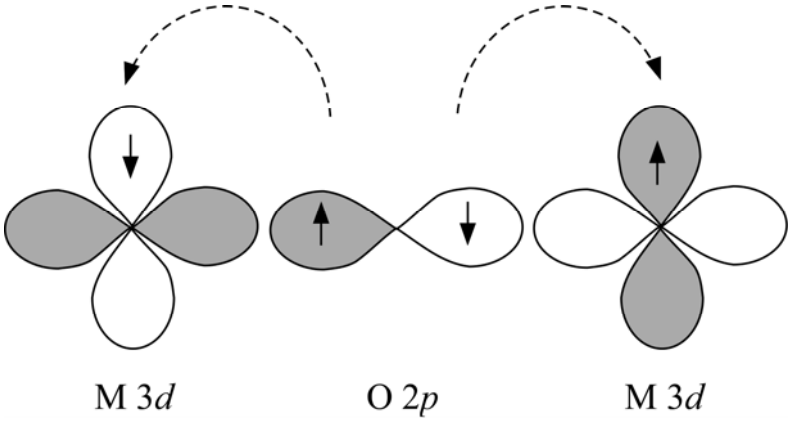

Figure 1.8 A simple view of superexchange in a linear M-O-M system giving antiferromagnetic alignment of ions with a bridging oxygen ligand.

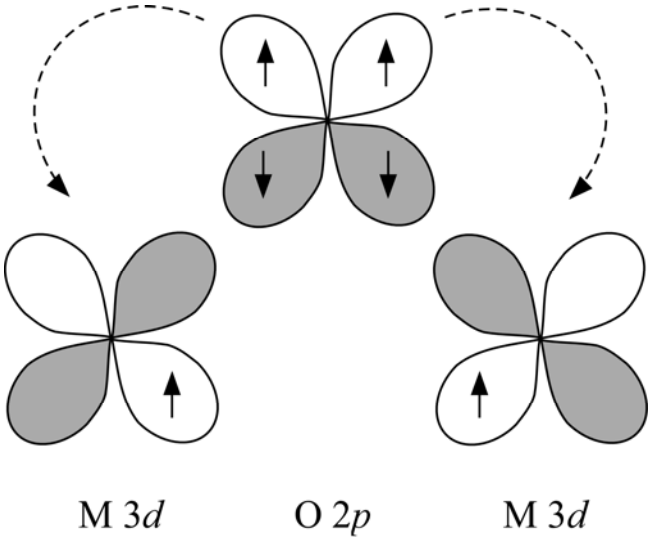

Figure 1.9 The superexchange pathway stabilising ferromagnetic coupling in a 90° M-O-M array.

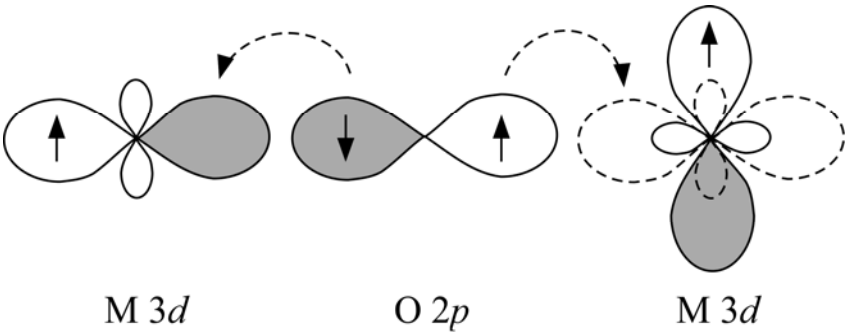

Figure 1.10 The superexchange pathway stabilising ferromagnetic coupling in an 180° M-O-M array.

The magnetic interactions described above are dominating in insulating or semiconducting materials. Other exchange pathways are possible when the adjacent cations have different oxidation states or orbital occupancies due to orbital order. For example, double exchange interactions[63, 64], which are seen in metallic materials, predicts that the movement of an electron from one ion to the another is made easier if it does not have to change spin direction in order to comply with Hund's rule when received on the other ion. Delocalisation of electrons between neighbouring ions reduces the kinetic energy and will therefore favour a ferromagnetic alignment of the magnetic moments. This can be seen in the mixed-valent manganites between the spins of the Mn^{3+} and Mn^{4+} ions[65, 66].

1.1.3.3 Types of magnetic order

Although an indication of the type of magnetic ordering in a material can be obtained by magnetic susceptibility measurements, it does not provide any details about the arrangement of spins. This information is best obtained through neutron diffraction techniques as neutrons are scattered by unpaired electrons.

For antiferromagnets, there are numerous ways in which the equal number of up and down spins can be arranged on the lattice[51]. What arrangements are possible depends also on the type of crystal lattice in which the spins are situated. Some examples are given in Figure 1.11. The G-type ordering is very common in cubic perovskites, which have the magnetic atoms arranged on a simple cubic lattice, because all nearest neighbour atoms are forced into an antiferromagnetic alignment by the superexchange interactions that occur via the oxygen atoms. This type of ordering is found in $LaFeO_3$[67] and $LaCrO_3$[68]. Other cubic perovskites, such as $LaMnO_3$[14], has alternately aligned ferromagnetic planes or the A-type ordering. In the latter case, this order is a result of the Jahn-Teller distortion of the Mn^{3+} ions. Ferrimagnets do not follow the Curie Weiss law as the magnetic structure is made up of sublattices with different molecular fields and hence different temperature dependence of the magnetisations. Ferrites are a group of compounds with the chemical formula MFe_2O_4, where M is a divalent cation such as Zn^{2+}, Co^{2+} or Cu^{2+}, that show ferrimagnetic ordering[69]. They have two non-equivalent sublattices due to their spinel crystal structure which contains two types of crystallographic lattice

site, octahedral and tetrahedral, with two different ions. There are also other more complex forms of magnetic order such as helical order and spin glasses[70] but that will not be discussed here as it is not applicable to the work in this thesis.

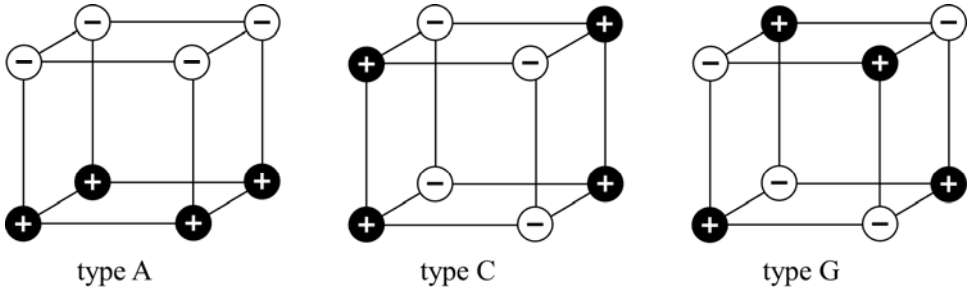

Figure 1.11 Three types of antiferromagnetic order for simple cubic lattices with the two possible spin states represented by + and –.

1.2 High Pressure

As mentioned at the beginning of this chapter, the physical properties of solid materials are strongly dependant on the crystal structure and interatomic distances. The atomic distances in a solid can be considerably more varied by pressure than by for example temperature; therefore pressure offers a very powerful method of tuning the volume and the consequent properties of a sample in a controllable and reversible manner. The application of high pressure can bring about structural, electrical and other phase transitions making it possible to study the correlation between these transitions and changes in certain properties, this allows the possibility of gaining a better fundamental understanding of the underlying phenomena as well as improving the design of applied materials. Another advantage of using pressure is that it is a "clean" tool, in that it can cause significant changes in the structural and physical properties without changing the thermal energy or chemical composition of a system. In addition, high pressure can be used to synthesise compounds with, for example, very distorted structures that can not be stabilised under ambient conditions, opening up the possibility of finding new materials with interesting and unusual structural and physical properties[71, 72].

As a result of the development of new techniques and efficient diffractometric equipment, high-pressure crystallography has, during the last two decades, become a powerful technique that can be routinely used in laboratories and dedicated neutron and synchrotron facilities[73-75] at both low and high temperature conditions. In particular, the invention of the diamond anvil cell (DAC) has led to a constant rise of the number of structural determinations at high pressures each year. The DAC is also used to perform complimentary studies like magnetic, electrical and optical behaviour, Raman, X-ray absorption and other spectroscopy measurement [75-77].

Application of external pressure normally results in a suppression of the charge-ordered state or a decrease in the charge-ordering transition temperature, T_{CO}, as observed in the perovskites manganites[78, 79] and nickelates[80]. Analogously, pressure-induced insulator to metal (MI) transitions or decreased MI transition temperature, illustrated in Figure 1.12, are observed in many compounds[81, 82] and it is generally believed that at sufficiently high pressures, all substances become metallic[83]. The variation of the electronic bandwidth is the driving force for the evolution of the insulator-to-metal transition as a function of "chemical" and applied pressure. Pressure can also induce superconductivity in some substances (e.g. boron, silicon, sulphur and organic superconductors etc.[84-86]) and enhance[87] or suppress[88] it in others.

The magnetic properties of materials are very sensitive to structural distortions as the exchange mechanisms between the magnetic atoms, and hence the magnetic order, depend on the interatomic distances. Much interest has been shown in compounds with related electronic and magnetic properties such as the perovskite manganites where colossal magnetoresistance (CMR) occur at temperatures near the magnetic transition temperature. For example, it has been shown that in doped $LaMnO_3$ compounds, applying pressure leads to an increase in the Curie temperature[89] and in $Pr_{0.7}Ca_{0.3}MnO_3$ high pressure brings about a change from an antiferromagnetic insulating state to a ferromagnetic metallic state[78]. Pressure induced magnetic phase transitions have also been observed in several transition metal compounds, other alloys and intermetallic compounds[90-92]. The objective of

this thesis was to study the effect of pressure and temperature on the charge, spin and orbital ordering in new crystalline materials. This was achieved by utilising diffraction techniques to investigate the structural properties of three different compounds under varying pressure and temperature conditions. Firstly, the charge order in the perovskite $BiNiO_3$ was studied by means of neutron powder diffraction in both high pressure and low temperature environments. Neutrons were also used to determine the magnetic structure of $BiNiO_3$ as well as the magnetic and orbital order in the fluoride $KCrF_3$ at low temperatures. Finally, synchrotron X-ray diffraction has been used to study the charge order in the molecular conductor $(EDT\text{-}TTF\text{-}CONH_2)_6[Re_6Se_8(CN)_6]$ at high pressure.

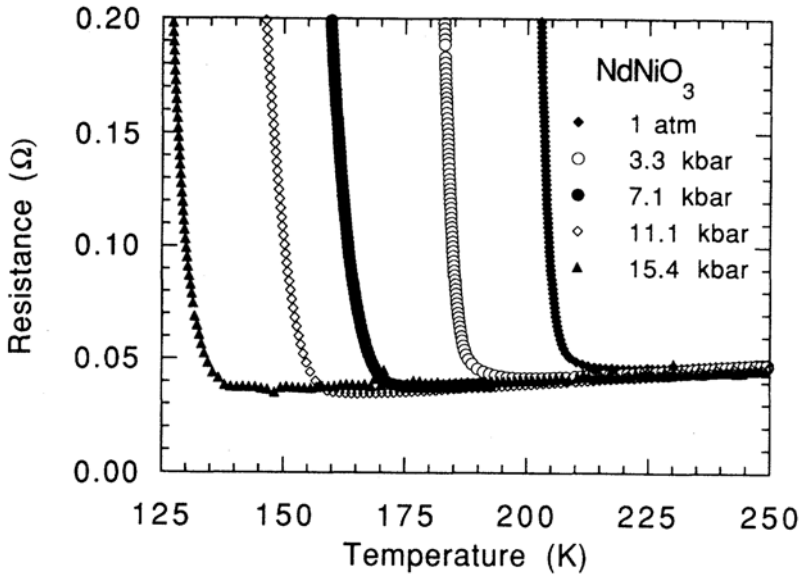

Figure 1.12 Resistance of $NdNiO_3$ as a function of temperature at different pressures showing that the transition temperature T_{MI} strongly decreases with increasing pressure. From [82].

1.3 References

1. J.B. Goodenough, *Phys. Rev.*, **100**, 564 (1955).
2. P.G. Radaelli, D.E. Cox, M. Marezio and S.W. Cheong, *Phys. Rev. B*, **55**, 3015 (1997).
3. D.E. Cox and A.W. Sleight, *Acta Cryst. B*, **35**, 1-10 (1979).
4. E. Wigner, *Trans.Far. Soc.*, **34**, 0678 (1938).
5. E.J.W. Verwey and P.W. Haayman, *Physica*, **8**, 979 (1941).
6. E.J.W. Verwey, *Nature*, **144**, 327 (1939).
7. J.P. Attfield, *Solid State Sci.*, **8**, 861 (2006).
8. J.P. Wright, J.P. Attfield and P.G. Radaelli, *Phys. Rev. B*, **66**, 214422 (2002).
9. P. Novák, J. Englich, J. Kohout and V.A.M. Brabers, *Phys. Rev. B*, **61**, 1256 (2000).
10. J. Garcia and G. Subias, *J. Phys.: Condens. Matter*, **16**, R145 (2004).
11. G. Subias, J. Garcia, J. Blasco, M.G. Proietti, H. Renevier and M.C. Sanchez, *Phys. Rev. Lett.*, **93**, (2004).
12. C. Zener, *Phys. Rev.*, **82**, 403 (1951).
13. M. Uehara, S. Mori, C.H. Chen and S.W. Cheong, *Nature*, **399**, 560 (1999).
14. E.O. Wollan, *Phys. Rev.*, **100**, 545 (1955).
15. R.J. Goff and J.P. Attfield, *Phys. Rev. B*, **70**, (2004).
16. J.M. Tranquada, B.J. Sternlieb, J.D. Axe, Y. Nakamura and S. Uchida, *Nature*, **375**, 561 (1995).
17. M.I. Salkola, V.J. Emery and S.A. Kivelson, *Phys. Rev. Lett.*, **77**, 155 (1996).
18. T. Nakajima, H. Kageyama and Y. Ueda, *J. Phys. Chem. Solids*, **63**, 913 (2002).
19. A.J. Williams and J.P. Attfield, *Phys. Rev. B*, **72**, 024436 (2005).
20. A.J. Williams and J.P. Attfield, *Phys. Rev. B*, **66**, 220405 (2002).
21. J. Herrero-Martin, J. Garcia, G. Subias, J. Blasco and M.C. Sanchez, *Phys. Rev. B*, **70**, (2004).
22. J. Garcia, M.C. Sanchez, G. Subias and J. Blasco, *J. Phys.: Condens. Matter*, **13**, 3229 (2001).

23. A. Daoud-Aladine, J. Rodríguez-Carvajal, L. Pinsard-Gaudart, M.T. Fernández-Díaz and A. Revcolevschi, *Phys. Rev. Lett.*, **89**, 097205 (2002).
24. F. Millange, E. Suard, V. Caignaert and B. Raveau, *Mat. Res. Bull.*, **34**, 1 (1999).
25. P. Karen, P.M. Woodward, J. Lindén, T. Vogt, A. Studer and P. Fischer, *Phys. Rev. B*, **64**, 214405 (2001).
26. T. Vogt, P.M. Woodward, P. Karen, B.A. Hunter, P. Henning and A.R. Moodenbaugh, *Phys. Rev. Lett.*, **84**, 2969 (2000).
27. M.L. Foo, Y. Wang, S. Watauchi, H.W. Zandbergen, T. He, R.J. Cava and N.P. Ong, *Phys. Rev. Lett.*, **92**, 247001 (2004).
28. K. Takada, H. Sakurai, E. Takayama-Muromachi, F. Izumi, R.A. Dilanian and T. Sasaki, *Nature*, **422**, 53 (2003).
29. J.B. Torrance, P. Lacorre, A.I. Nazzal, E.J. Ansaldo and C. Niedermayer, *Phys. Rev. B*, **45**, 8209 (1992).
30. P.M. Woodward, D.E. Cox, E. Moshopoulou, A.W. Sleight and S. Morimoto, *Phys. Rev. B*, **62**, 844 (2000).
31. R.J. Cava, B. Batlogg, J.J. Krajewski, R. Farrow, L.W. Rupp, A.E. White, K. Short, W.F. Peck and T. Kometani, *Nature*, **332**, 814-816 (1988).
32. A.W. Sleight, J.L. Gillson and P.E. Bierstedt, *Solid State Comm.*, **17**, 27-28 (1975).
33. J.P. Attfield, *J. Res. Nat. Inst. Stan. Tech.*, **109**, 99 (2004).
34. F.J. Berry, S. Skinner and M.F. Thomas, *J. Phys.: Condens. Matter*, **10**, 215 (1998).
35. A. Yakubovskii, A. Trokiner, S. Verkhovskii, A. Gerashenko and D. Khomskii, *Phys. Rev. B*, **67**, 064414 (2003).
36. J.P. Attfleld, A.W. Sleight and A.K. Cheetham, *Nature*, **322**, 620 (1986).
37. T. Takahashi, *J. Phys. Chem. Solids*, **62**, 105 (2001).
38. H. Kino and H. Fukuyama, *J. Phys. Soc. Jpn.*, **65**, 2158 (1996).
39. H. Seo, *J. Phys. Soc. Jpn.*, **69**, 805 (2000).
40. D.S. Chow, E. Zamborszky, B. Alavi, D.J. Tantillo, A. Baur, C.A. Merlic and S.E. Brown, *Phys. Rev. Lett.*, **85**, 1698 (2000).
41. T. Takahashi, *Synthetic Metals*, **133**, 261 (2003).

42. H. Seo and H. Fukuyama, *J. Phys. Soc. Jpn.*, **66**, 1249 (1997).
43. D.I. Khomskii and M.V. Mostovoy, *J. Phys. A. Math. Gen.*, **36**, 9197 (2003).
44. H.A. Jahn and E. Teller, *Proc. R. Soc. A*, **161**, 220 (1937).
45. P.A. Cox, *The Electronic Structure and Chemistry of Solids*; Oxford University Press: Oxford, 1987.
46. N. Binggeli and M. Altarelli, *Phys. Rev. B*, **70**, 085117-10 (2004).
47. Y. Ito and J. Akimitsu, *J. Phys. Soc. Jpn.*, **40**, 1333 (1976).
48. M.T. Hutchings, M.J. Fair, P. Day and P.J. Walker, *J. Phys. C. Sol. State. Phys.*, **9**, L55 (1976).
49. D.I. Khomskii and K.I. Kugel, *Phys. Rev. B*, **67**, 134401 (2003).
50. D. Vaknin, S.K. Sinha, D.E. Moncton, D.C. Johnston, J.M. Newsam, C.R. Safinya and H.E. King, *Phys. Rev. Lett.*, **58**, 2802 (1987).
51. E.O. Wollan and W.C. Koehler, *Phys. Rev.*, **100**, 545 (1955).
52. P.G. Radaelli, *New. J. Phys.*, **7**, 53 (2005).
53. J. Karle, *Phys. Today*, **42**, 22 (1989).
54. J.B. Goodenough, *Magnetism and the Chemical Bond*; Interscience: New York, 1963.
55. B. Keimer, *Nat Mater*, **5**, 933 (2006).
56. A.V. Mahajan, D.C. Johnston, D.R. Torgeson and F. Borsa, *Phys. Rev. B*, **46**, 10966 (1992).
57. Y. Ren, T.T.M. Palstra, D.I. Khomskii, A.A. Nugroho, A.A. Menovsky and G.A. Sawatzky, *Phys. Rev. B*, **62**, 6577 (2000).
58. Y. Ren, T.T.M. Palstra, D.I. Khomskii, E. Pellegrin, A.A. Nugroho, A.A. Menovsky and G.A. Sawatzky, *Nature*, **396**, 441 (1998).
59. http://folk.uio.no/ravi/activity/ordering/chargeordering.html [cited 2008 May].
60. S. Elliot, *The physics and chemistry of solids*; Wiley: Chichester, 1998.
61. J.B. Goodenough, *Phys. Rev.*, **117**, 1442 (1960).
62. P.W. Anderson, *Phys. Rev.*, **79**, 350 (1950).
63. P.G. de Gennes, *Phys. Rev.*, **118**, 141 (1960).
64. C. Zener, *Phys. Rev.*, **82**, 403 (1951).
65. A.P. Ramirez, *J. Phys.: Condens. Matter*, **9**, 8171 (1997).

66. A.J. Millis, P.B. Littlewood and B.I. Shraiman, *Phys. Rev. Lett.*, **74**, 5144 (1995).
67. W.C. Koehler, E.O. Wollan and M.K. Wilkinson, *Phys. Rev.*, **1**, 58 (1960).
68. M.A. Gilleo, *Acta Crys.*, **10**, 161 (1957).
69. L. Neel, *Ann. Phys.*, **3**, 137 (1948).
70. S. Blundell, *Magnetism in condensed matter*; Oxford University Press: Oxford, 2001.
71. G. Demazeau, *J. Phys.: Condens. Matter*, **14**, 11031 (2002).
72. J.A. Rodgers, A.J. Williams and J.P. Attfield, *Zeits. F. Naturf. Sect. B*, **61**, 1515 (2006).
73. R.M. Wilson, J.S. Loveday, R.J. Nelmes, S. Klotz and W.G. Marshall, *Nucl. Inst. Meth. in Phys. Res. Sect. A*, **354**, 145 (1995).
74. L. Merrill and W.A. Bassett, *Rev. Sci. Inst.*, **45**, 290 (1974).
75. A. Katrusiak, *Acta Crys. A*, **64**, 135 (2008).
76. H.K. Mao and P.M. Bell, *Rev. Sci. Inst.*, **52**, 615 (1981).
77. A. Jayaraman, *Rev. Mod. Phys.*, **55**, 65 (1983).
78. Y. Moritomo, H. Kuwahara, Y. Tomioka and Y. Tokura, *Phys. Rev. B*, **55**, 7549 (1997).
79. J.M.D. Coey, M. Viret and S. von Molnar, *Adv. Phys.*, **48**, 167 (1999).
80. J.L. Garcia-Munoz, M. Amboage, M. Hanfland, J.A. Alonso, M.J. Martinez-Lope and R. Mortimer, *Phys. Rev. B*, **69**, (2004).
81. M. Imada, A. Fujimori and Y. Tokura, *Rev. Mod. Phys.*, **70**, 1039 (1998).
82. X. Obradors, L.M. Paulius, M.B. Maple, J.B. Torrance, A.I. Nazzal, J. Fontcuberta and X. Granados, *Phys. Rev. B*, **47**, 12353 (1993).
83. E. Wigner and H.B. Huntington, *J. Chem. Phys.*, **3**, 764 (1935).
84. L. Brossard, M. Ribault, L. Valade and P. Cassoux, *J. de Physique*, **50**, 1521 (1989).
85. H. Fujiwara, E. Fujiwara, Y. Nakazawa, B.Z. Narymbetov, K. Kato, H. Kobayashi, A. Kobayashi, M. Tokumoto and P. Cassoux, *J. Am. Chem. Soc.*, **123**, 306 (2001).
86. V.V. Struzhkin, R.J. Hemley, H.K. Mao and Y.A. Timofeev, *Nature*, **390**, 382 (1997).

87. C.W. Chu, L. Gao, F. Chen, Z.J. Huang, R.L. Meng and Y.Y. Xue, *Nature*, **365**, 323 (1993).

88. R.D. McDonald, A.K. Klehe, J. Singleton and W. Hayes, *J. Phys.:Condens. Matter*, **15**, 5315 (2003).

89. H.Y. Hwang, T.T.M. Palstra, S.W. Cheong and B. Batlogg, *Phys. Rev. B*, **52**, 15046 (1995).

90. F. Ishikawa, T. Goto and H. Fujii, *Physica B*, **329-333**, 657 (2003).

91. M. Matsushita, S. Endo, K. Miura and F. Ono, *J. Magn. Magn. Mat.*, **265**, 352 (2003).

92. M.P. Pasternak, G.K. Rozenberg, W.M. Xu and R.D. Taylor, *Int. J. High Press. Res.*, **24**, 33-44 (2004).

Chapter 2

Experimental Techniques

2.1 Theory of diffraction

Diffraction techniques are some of the most powerful tools available for the characterisation and determination of crystalline materials. The structure of a crystalline material can be thought of as an arrangement of atoms extending in three directions with the unit cell being the repeating unit that fills the space. If the incident radiation has a wavelength that is comparable to the inter-atomic spacings in the crystals, these can act as a diffraction grating. In a diffraction experiment, the radiation will then be scattered in directions determined by the size and shape of the unit cell with an intensity dependant on the position of the atoms within it. Both neutrons and X-rays have wavelengths suitable for diffraction.

In the Bragg approach, crystals are regarded as being made out of parallel lattice planes all acting like semi-transparent mirrors. Some of the beams will be reflected off a plane with the same angle of reflection as the angle of incidence but others are transmitted and then subsequently reflected by succeeding planes. The derivation of Bragg's law, equation 2.1, can be obtained by considering two beams in phase with an angle of incidence, θ, reflected by two adjacent planes spaced a distance, d, apart. For constructive interference to occur, the beams must stay in phase and hence the path difference, $2x$, must be equal to a whole number of wavelengths. From Figure 2.1 it can be seen that $x = d_{hkl}\sin\theta$ giving rise to the Bragg law.

$$\lambda = 2d_{hkl}\sin\theta \qquad (2.1)$$

where λ is the wavelength of the radiation, d_{hkl} is the spacing between the planes and θ is the angle of incidence, or *Bragg angle*. When Bragg's law is satisfied, the

reflected beams will be in phase and give rise to constructive interference. At all angles different to the Bragg angle, the beams are out of phase and interfere destructively.

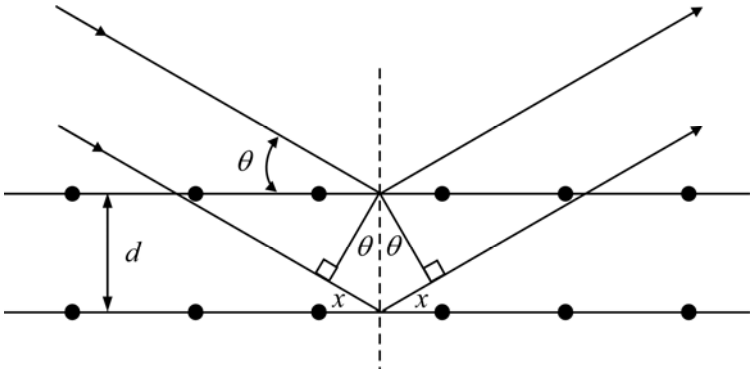

Figure 2.1 Diffraction from a set of lattice planes, separated by a distance, *d*.

The size and symmetry of the lattice can be obtained from analysing the position of the Bragg peaks whereas the position of the atoms within the cell is dependant on the intensity. The intensity of the diffracted beam I_{hkl} is proportional to $|F_{hkl}|^2$, where F_{hkl} is the structure factor or structure amplitude for the *hkl* reflection which is defined as

$$F_{hkl} = \sum_i f_i \exp(2\pi i(hx_i + ky_i + lz_i)) \exp(-(8\pi^2 U_{iso,i} \sin^2 \theta / \lambda^2)) \qquad (2.2)$$

The sum is over all the atoms in the unit cell, f_i is the scattering factor or form factor for X-rays (scattering length, b_i for neutrons) of the i^{th} atom, *hkl* are the Miller indices of the particular plane and x_i, y_i, z_i are the fractional coordinates of the atoms within the unit cell. Thermal motion is taken into account through the temperature factor, $U_{iso,i} = \overline{u_i^2}$, which is the mean isotropic square thermal displacement parallel to the diffraction vector of the i^{th} atom from its equilibrium position. However, if the thermal motion of the atoms is anisotropic the correction to the structure factor is:

$$F_{hkl} = \sum_i f_i \exp(2\pi i(hx_i + ky_i + lz_i)) \exp(-(2\pi^2 (U_{11}(ha^*)^2 + ... + U_{12} ha^* kb^* + ...)) \qquad (2.3)$$

There are two techniques available for studying crystalline materials, single-crystal or powder diffraction. The latter is often preferred because it is faster and it is difficult to grow large good quality single crystals of certain materials. Furthermore, doing measurements under extreme conditions is often easier using powder methods than single crystals.

In a single crystal experiment, the orientation of the crystal can be adjusted so that a complete pattern is obtained and the diffraction data are collected using a detector or film covering two dimensions. The result is a pattern of spots of varied intensity and size. From the position of the spots, information about the unit cell geometry and symmetry is obtained whilst the intensities provide key information about the position of the atoms in the unit cell. This means that the intensities of all the individual reflections can be obtained and used to determine the full crystal structure.

2.1.1 Powder diffraction

A powder sample consists of an enormous number of very small randomly ordered crystallites, usually of the dimension 10^{-7}-10^{-4} m, so that every possible orientation exists within the sample. Therefore, an X-ray or neutron beam hitting the sample will be diffracted in all possible directions as determined by the Bragg law. As a result of this, each lattice spacing in the crystal will give rise to a cone of diffraction Figure 2.2. Every cone is composed of a group of closely spaced dots that each represents the diffraction from a single crystallite within the sample. With a great number of crystallites, there will be enough dots to join together to form the cone. If the Bragg angle is θ, then the angle between the diffracted beams is 2θ. To obtain data that will be useful for analysis, the position of the different cones need to be determined. Despite the compression of the data from three into one dimension, structural information can be obtained with powder diffraction using high resolution instruments.

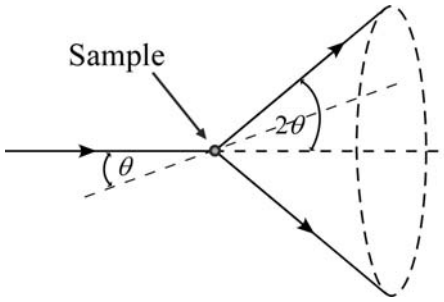

Figure 2.2 The formation of a cone of diffracted radiation by a polycrystalline sample.

2.2 X-ray diffraction

X-rays have wavelengths that are similar to the interatomic spacings in a crystal and are therefore ideal for conducting diffraction studies. An X-ray beam can be described as an electromagnetic wave and therefore interacts with electrons in atoms. The electrons act as secondary point sources of X-rays and will interact elastically with the wave by emitting radiation which is in phase or coherent with the incident X-ray beam. However, incoherent scattering, or Compton scattering, also occurs as an effect of inelastic interactions between the X-rays and the electrons. In this case the scattered radiation will be out of phase with the incident beam and, will contribute to the background radiation in X-ray diffraction experiments.

In the direction of the incident beam, all X-rays will be scattered in phase and the intensity is then the sum of all the scattered beams. Hence, the atomic scattering factor, or form factor, f, is directly proportional to the atomic number, Z, or more correctly, the number of electrons in the atom. For scattering at some angle, 2θ from the incident beam there will be a phase difference between the diffracted beams. Because of the finite size of the electron cloud, this phase difference is normally less than one wavelength and consequently, only partial destructive interference occurs between the beams. This results in a gradual reduction of the scattering intensity with increasing angle, 2θ. The wavelength of the X-rays also has an effect on the net intensity and the scattering factor is usually given as a function of $(\sin\theta)/\lambda$. The consequences of the dependence of the scattering factor on this expression is that powder patterns are usually weak at high angles and that it can be difficult to locate very light atoms in the presence of heavy atoms. Furthermore, it is

hard to distinguish between neighbouring elements in the periodic table using X-ray diffraction.

Single crystal X-ray diffraction is arguably the most important technique for determining the structures of crystalline materials. The unit cell parameters and the space group can be relatively easily obtained directly from the experimental measurements. To locate the position of the atoms in the unit cell is however, more difficult. The arrangement and nature of atoms in a crystal are related to the intensities of the diffraction pattern by a Fourier synthesis. If the amplitude and phase of all of the individual waves (or structure factors) are known, Fourier transformation will give the electron density, and thus the crystal structure. Unfortunately, the observed intensities only provide information about the amplitude of the scattered radiation and the knowledge about the phase is lost. This gives rise to the so-called phase problem, a fundamental challenge in X-ray crystallography. Structure solution methods have been developed to overcome this problem[1]. The single crystal data in this thesis was solved using direct-space methods[2] and the refinement was performed using the program CRYSTALS[3]. More details are provided in Chapter 5.

In laboratories, the most common source of X-rays is an X-ray tube in which electrons are generated from a cathode, accelerated to high velocities and bombarded onto a metal target. The interaction of the electrons with the metal target atoms generates a spectrum of X-rays with almost monochromatic wavelengths, superimposed on a broad spectrum background, characteristic of the target. A single wavelength can then be selected by using a crystal monochromator or metal filter. One of the most common target metals is copper which gives a characteristic X-rays of wavelength 1.5418 Å.

2.2.1 Synchrotron X-ray diffraction

Much more intense X-rays than from conventional sources, as well as other parts of the electromagnetic spectrum, can be produced by a synchrotron radiation source. In a synchrotron, electrons are accelerated to move at relativistic velocities and are constrained to move in a circular orbit of very large radius by a series of

bending magnets. An illustration of the main constituents of a synchrotron radiation source is shown in Figure 2.3. To prevent electrons from being lost through collision with atoms, the ring cavity is kept under extremely high vacuum. Before the particles are injected into the ring they are accelerated by a linear accelerator (linac), and then a booster. If the velocity of the electrons is below the operating energy when they are inserted into the ring, the machine is used as a true synchrotron as an additional short period of acceleration is needed after injection. If the operating energy has already been reached at the time of injection, the ring is used as a storage ring as no acceleration is needed, and the particles can be kept circulating for a period of time. Insertion devices such as undulators and wigglers are inserted into the electron beam to preserve the collimation in both the horizontal and vertical direction. They consist of a sequence of small magnets with well defined strength and polarity and help produce radiation of extremely high brilliance.

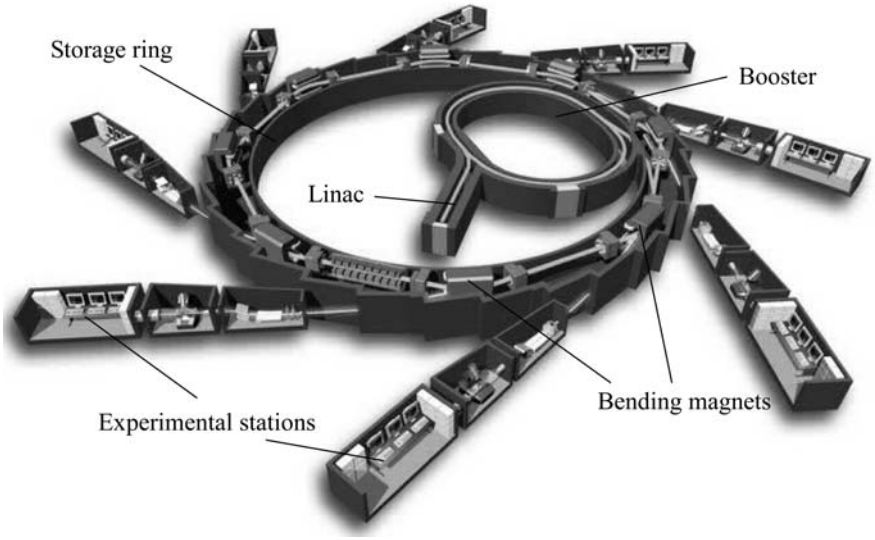

Figure 2.3 The production of synchrotron radiation in a particle accelerator.

When the electrons pass the bending magnets in the synchrotron, their path is deflected and they lose energy which is emitted as photons in a narrow cone in the forward direction tangentially from the ring. The radiation emitted from a bending magnet is a broad white beam with a continuous spectrum ranging from infra-red to short wavelength X-rays from which a single wavelength can be chosen using a

monochromator. This beam will have an intensity of many orders of magnitude higher than the output from an X-ray tube.

Examples of synchrotron X-ray sources are the United Kingdom Synchrotron Radiation Source (SRS) in Daresbury, Cheshire, the new Diamond light source in South Oxfordshire, UK, and the European Synchrotron Radiation Facility (ESRF) in Grenoble, France.

2.2.1.1 Station 9.5 and 9.8 at the SRS

All the synchrotron X-ray diffraction work reported in this thesis was carried out on the stations 9.5 and 9.8 at the SRS. Station 9.5 has a set-up especially developed for high-pressure powder diffraction crystallography and it provides a focussed monochromatic X-ray beam of ~0.5 Å for studies using diamond anvil cells. A white X-ray beam is taken into the station and a silicon crystal in Laue geometry is used to produce monochromatic beams[4]. The beam is focused over a distance of four meters which intensifies the radiation and the diffraction data can be collected using A4-sized image plates. A Molecular Dynamics "storm" scanner is then used to produce .dat or .gel files from the image plates. Alternatively, data can be recorded online with a mar345b image plate detector[4, 5]. The former method was used for the experiments in this thesis. The intensity of the beam means that high quality data can be collected in only 10 minutes on very small samples contained in diamond anvil cells. Pressure measurements are made off-line using spectral measurements of ruby fluorescence. During the experiments the width of the beam was reduced by a pinhole of 80 μm diameter.

Station 9.8 is a high flux single crystal facility with a Bruker-Nonius APEXII CCD detector and D8 diffractometer[5]. Data can be collected in the temperature region 85 to 600 K at wavelengths between 0.30 Å and 1.45 Å and at high pressure using a diamond anvil cell. A monochromatic beam is received from either a 111 or 220 silicon crystal which gives an optimum sample focus for a wavelength of 0.7 Å and 0.3 Å, respectively. There is a choice of four standard collimators (0.8, 0.5, 0.3, 0.2 mm) and during the single crystal experiments on this station the 0.2 mm

collimator was used. A standard structural data collection takes around 1 hour and 30 minutes. As with station 9.5 the pressure has to be measured off-line.

2.2.1.2 The diamond anvil cell (DAC)

The Diamond Anvil Cell (DAC) is an excellent device for generating hydrostatic high pressure. Because diamond is a very hard material and relatively transparent to X-rays and light it allows for a variety of optical studies to be carried out and pressures of up to 400 GPa have been obtained[6]. The assembly of the DAC is illustrated in Figure 2.4. Pressure is generated by applying a force to the large flat parallel faces of two opposed diamond anvils. A gasket that consists of a thin metal foil, e.g. tungsten or steel, with a small hole drilled through it, typically 100-250μm in diameter, is placed between the diamonds. This stops the diamonds from crushing the crystals (during single crystal experiments) and also provides a sample chamber. The sample, some pressure gauge and a pressure transmitting medium are placed in the hole in the metal gasket which is sealed as the small culet faces are pushed together. Because pressure is defined as force divided by the area over which the force is applied, the level of pressure generated depends on the size and shape of the diamond culets. There are various types of cells available[7] but the tool used for the high pressure synchrotron diffraction studies presented in this thesis was the Merrill-Bassett gasketed DAC[8-10] Figure 2.5. With this design, pressure is generated by tightening the Allen screws. The diamond culets can only be corrected laterally so the parallel alignment has to be controlled during the mounting of the diamonds on the beryllium backing plates. Poor alignment can lead to failure in the diamonds.

Beryllium is the material used for the backing plates as it has a relatively low absorption cross-section for X-rays allowing for wide angle X-ray access to the sample. It also has a high tensile strength and so it can be used for pressures of more than 20 GPa. However, a disadvantage is that the scattering of beryllium contributes to a high background in single crystal diffraction experiments. In addition, it is toxic so and therefore beryllium is gradually being replaced by tungsten carbide seats.

As the pressure in a DAC is applied uniaxially, a pressure-transmitting medium has to be used in order for the sample to be subjected to hydrostatic

pressure. This medium can be a liquid, solid or a gas but should be chosen so that it does not react with the sample or interfere with the measurement. It should also remain its hydrostatic properties at elevated pressures.

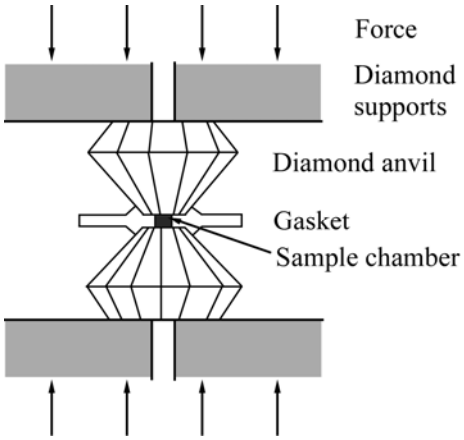

Figure 2.4 Assembly of the diamond-anvil cell.

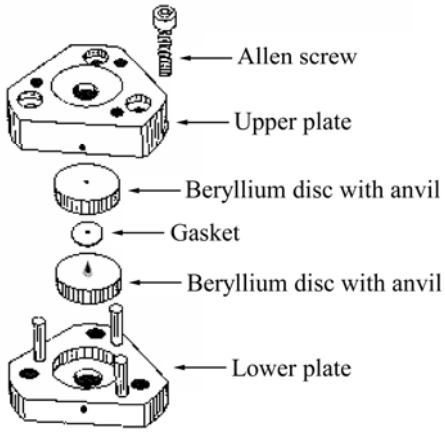

Figure 2.5 Cross-section of the Merrill-Bassett diamond-anvil cell[8].

To obtain a measurement of the pressure inside the cell, a pressure gauge has to be placed in the gasket hole next to the sample. The most convenient method, which was used for the DAC experiments in this work, is based on the ruby fluorescence[11]. Ruby has two distinct fluorescence emission lines that shift linearly with pressure up to 25 GPa. In practice, a ruby chip is put in the gasket hole with the sample and a laser is used to excite the fluorescence which is measured by a spectrometer. This method however, is only suitable for room temperature measurements as the emission lines shift with temperature. An alternative way of determining the pressure is to use a crystal, such as NaCl, with a known equation of state. From the diffraction pattern the volume can be established and from the equation of state, the pressure.

X-ray diffraction data collected at high pressures using diamond anvil cells, are of lesser quality than data obtained at ambient conditions. This is a result of the increased absorption, Compton scattering and extinction effects caused by the diamond anvils. Furthermore, because of the small sample volume the signal is very

weak and it is often necessary to use synchrotron sources with high flux in order to detect subtle structural details, such as weak superstructures and small distortions of symmetry. There is also a limitation to the access of the reciprocal space as the sample is enclosed by steel which absorbs X-rays. The wavelength and sample to detector distance can be adjusted to ensure maximum coverage.

It is also important that the hydrostatic conditions are retained throughout the whole experiment as non-hydrostaticity leads to broadening of the diffraction peaks and consequently a decrease in the signal-to-noise ratio. Non-hydrostatic conditions can occur if the pressure medium starts to freeze.

2.3 Neutron diffraction

In addition to X-rays, neutrons can be used as an alternative tool to study the structures of crystalline materials. The de Broglie equation relates the momentum, p, of a free particle to the wavelength of the corresponding quantum-mechanical wave representation as:

$$\lambda = \frac{h}{p} = \frac{h}{mv} \qquad (2.4)$$

Therefore, neutrons with average thermal velocities of 2500 m/s will have a wavelength of 1.5 Å and can therefore be used in diffraction. Whilst X-rays interact with the electron cloud, neutrons interact with the nuclei of the atoms and the unpaired electron spins which provides several advantages[4]. Firstly, there is no fall off in the intensity with Bragg angle θ as the distance at which the interaction between the neutron and the nucleus occurs is much shorter than the wavelength of the neutron. Secondly, in contrast to the Z^2 dependence for X-rays, the scattering power of an atom is not strongly related to its atomic number. This means that neutron diffraction makes it possible to detect lighter elements in the presence of heavier ones, which is very useful when determining oxygen positions, and to distinguish between elements with similar atomic numbers as well as isotopes of the same element. The variation in scattering amplitude between elements is illustrated in Figure 2.6. Finally, the interaction between the neutron's magnetic moment and

those of the atoms/ions with unpaired electron spin provides information about magnetic order. With magnetic scattering however, there is a fall off with intensity with $(\sin\theta)/\lambda$ like that of X-ray scattering as the interactions are with electrons.

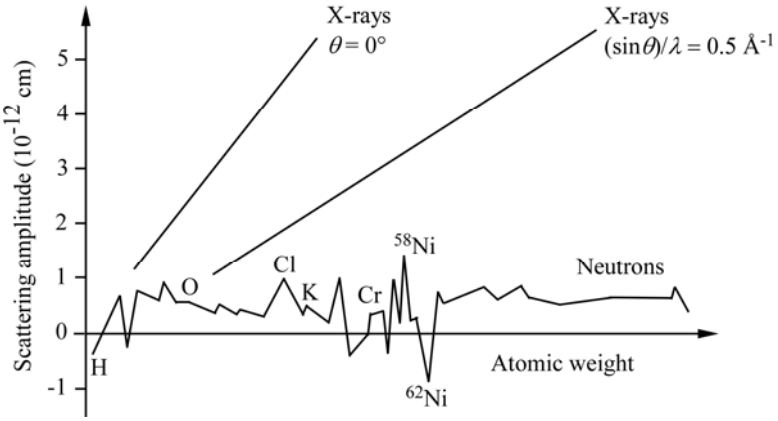

Figure 2.6 Variation of neutron scattering amplitude with atomic weight compared with the regular increase of X-rays[12].

The interaction between the neutron and the nucleus of an atom is weak, making it a highly penetrating, non-destructive probe which enables complex sample environments such as cryostats, furnaces and pressure cells to be used. However, the weak interactions and the lower intensity generally produced by neutron sources (compared to X-ray sources) means that larger samples are necessary. Because it is often very difficult to grow single crystals larger than the required size of at least 1 mm^3, powder diffraction methods are most commonly employed.

2.3.1 Magnetic neutron diffraction

Neutron diffraction can be used to study magnetic structures as neutrons, with spin quantum number of ½, possess a magnetic moment which can interact with unpaired electrons on cations in a crystal structure. The magnetic structure can be determined by collecting data below and above the magnetic ordering temperature, which makes it possible to identify of the peaks that are a result of coherent diffraction from magnetic spins. Paramagnetic materials scatter neutrons incoherently, as the magnetic spins are randomly orientated in all directions, and provide no contribution to the Bragg peaks, only to the background. Magnetic

scattering will occur when there is an ordered array of magnetic atoms. Ferromagnets generate magnetic peaks that are superimposed on the nuclear peaks since the atoms and the magnetic moments have the same periodicity. Antiferromagnets give rise to additional reflections on a supercell of the nuclear cell. The magnetic peaks can be indexed with *hkl* values and the magnetic unit cell, which may be of the same size or bigger than the crystallographic unit cell, can be determined. For example, if the antiferromagnetic ordering results in a doubling of the unit cell in all three directions one of the additional peaks will be (*hkl*) = (½,½,½). The magnetic peaks are normally observed at long *d*-spacings because of the fall off in the magnetic scattering length with θ. A magnetic model should be created that is in agreement with the symmetry, and the saturated magnetic moment for each atom in the magnetic structure can then be calculated by refinement of this model.

For unpolarised neutrons, where the neutron beam contains all directions of spin, the effective intensity for the *(hkl)* reflection is given by the sum of two terms that represent the nuclear and magnetic intensity:

$$F_{hkl}^2 = F_{nucl}^2 + F_{magn}^2 \qquad (2.5)$$

where F_{nucl} is the nuclear structure factor described earlier and and F_{magn} is the magnetic structure defined as:

$$F_{magn} = p\sum_j f_j q_j \exp^{2\pi i(hx+ky+lz)} \qquad (2.6)$$

where $p = e^2\gamma/2mc^2 = 0.2696 \times 10^{-12}$, f_j is the magnetic form factor and q_j is the magnetic interaction vector determined by the relative orientation of the magnetic moment, *m*, and the unit or scattering vector, ε**,** perpendicular to the scattering plane as show in Figure 2.7. This also illustrates that vector q_j lies in the plane of ε and *m*, normal to ε**,** with a magnitude of sinα. Magnetic diffraction will only occur if some component of the magnetic spin is parallel to the scattering plane as otherwise the value of *q* would be zero[13].

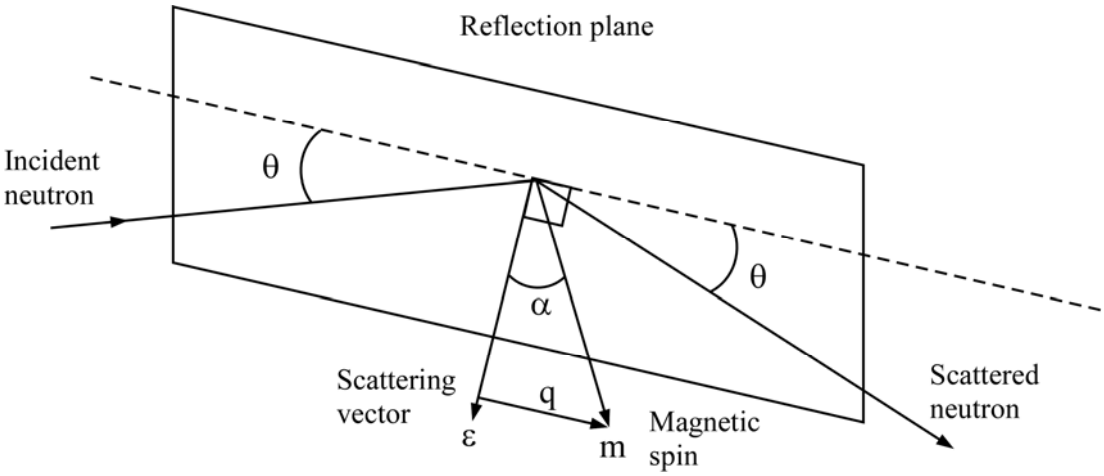

Figure 2.7 The relationship between the various vectors in magnetic neutron scattering.

Similarly to the form factor for X-ray scattering, the magnetic form factor, f_j, arises as a result of the electrons which determine the magnetic moment being distributed over a volume of space equivalent to the neutron wavelength. However, only a few electron orbits in an outer shell contributes to the magnetic moment and therefore the magnetic form factor falls off more rapidly with angle than the factor for X-ray scattering. This in turn leads to a severe limitation on the range of θ over which significant magnetic intensities can be detected. The magnetic form factor is characteristic to each magnetic ion, e.g. Mn^{2+} and in order to calculate the magnetic cross section and solve the magnetic structure it is necessary to know its angular variation.

2.3.2 Constant wavelength (angle dispersive) neutron diffraction

From the Bragg law, Equation 2.1, it is evident that neutron diffraction experiments can be performed in two ways. Either by having a fixed wavelength of the neutrons and varying the detector angle (angle dispersive) or varying the wavelength with a set detector angle (wavelength dispersive or time-of-flight).

Furthermore, neutrons can be generated from two sources; nuclear reactors and spallation sources. Constant wavelength neutron diffraction can utilise neutrons from a reactor source, which are in effect produced continuously in time. The

neutron beam from the reactor contains a distribution of wavelengths and is monochromised by using a single crystal, as for X-rays. The monochromated beam is then directed towards the sample. The most intense neutron source in the world can be found at the Institute Laue-Langevin (ILL) situated in Grenoble, France. The high-flux reactor produces 1.5×10^{15} neutrons per second per cm^2 by fission, with a thermal power of 58.3 MW. In order to provide a high flux at a wide range of wavelengths, three moderators at different temperatures are used. There is a peak for the thermal neutron flux at 1.2 Å in the Maxwellian distribution. The experimental layout of the ILL can be seen in Figure 2.8.

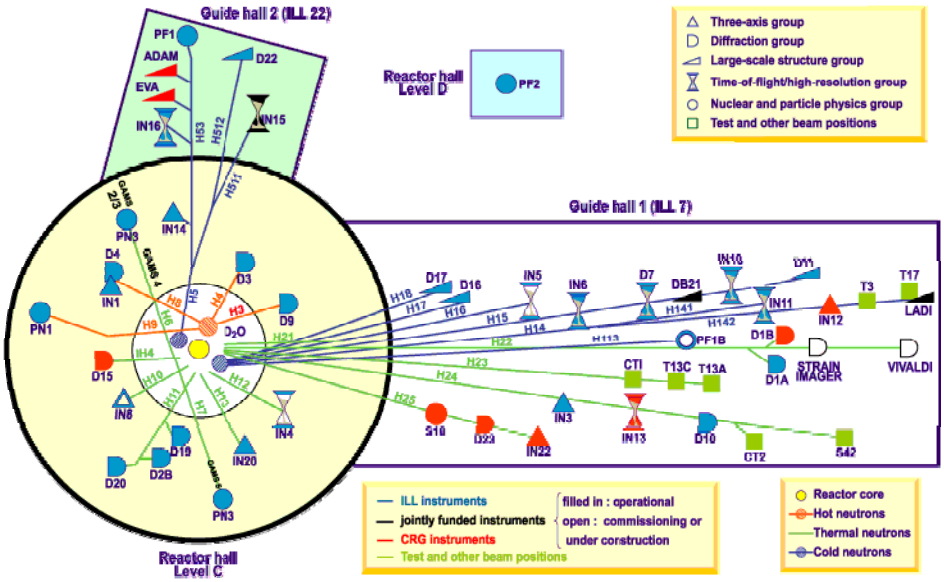

Figure 2.8 The experimental layout at the ILL[14].

2.3.2.1 The Super D2B diffractometer

D2B is a powder diffractometer designed to achieve the ultimate resolution, limited only by particle size. There is also an alternative high flux option, with lower resolution, available. The layout of the instrument is shown in Figure 2.9. The instrument is located on a beam tube in the reactor hall and it is characterised by the very high take-off angle of 135˚ for the Ge[115] monochromator. There are 128 detectors, 200 mm high, spaced at 1.25˚ intervals and a complete diffraction pattern can be obtained over the angular range $5^\circ < 2\theta < 165^\circ$ after about 25 steps of 0.05˚ in 2θ. To improve statistics, the scans are usually repeated several times. The optimum

flux is achieved at a wavelength of 1.594 Å, but by rotating the Ge crystals several different wavelengths in the range 1.051-3.152 Å are available. D2B was also designed for work on magnetism and very large *d*-spacings can be accessed using wavelengths of between 2.4 Å and 6 Å. Temperatures as low as 1.5 K and as high as 1000 K can be achieved using a He cryostat or a furnace, respectively. The new detector means that it is now possible to measure small samples of about 200 mg with high resolution.

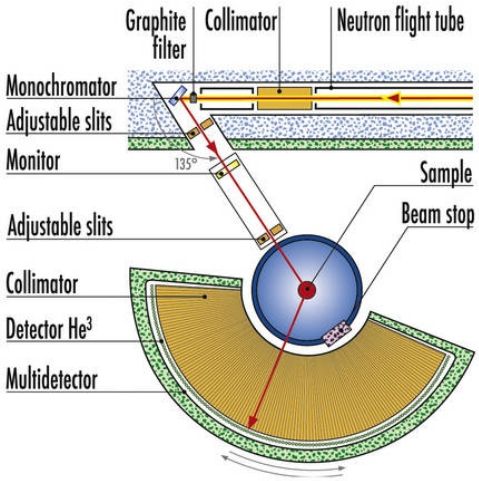

Figure 2.9 Instrument layout of D2B[15]

2.3.3 *Pulsed (time of flight) neutron diffraction*

In spallation sources, neutrons are usually generated in a pulsed manner by bombarding a heavy metal target with high energy protons. A specific wavelength can be selected however, in a time-of-flight (TOF) experiment, all wavelengths are used, and a complete diffraction pattern can be collected from each pulse of neutrons.

The wavelength and the velocity of the neutron are related through the de Broglie equation (2.3). If the total flight path from source to detector is L and the total time of flight is t, the neutrons have a velocity $\frac{L}{t}$ and a momentum $\frac{mL}{t}$. Using equation 2.3 gives the wavelength:

$$\lambda = \frac{ht}{mL} \qquad (2.7)$$

where m is rest mass of the neutron. Applying the Bragg equation (2.1) the total time of flight can be expressed as:

$$t = \frac{2mL}{h} d \sin\theta \qquad (2.8)$$

where d is the is the interplanar spacing and 2θ is the Bragg scattering angle. Therefore, by having a fixed detector angle and scanning the wavelength, a range of d-spacings can be measured in a TOF experiment. In order to collect simultaneous diffraction patterns, the diffractometers often have several detector banks at different set angles.

At the Rutherford Appleton Laboratory, ISIS, neutrons are produced by bombarding a tantalum target with pulses of highly energetic protons. This creates an extremely intense neutron pulse with only very little heat production at the target. The energies and velocities of the neutrons produced in this way are too high to be useful for condensed matter studies so small hydrogenous moderators are placed around the target to slow them down. The moderators are ambient temperature water (43˚C), liquid hydrogen (20 K) and liquid methane (100 K). These temperatures determine the spectral distribution of the produced neutrons. The experimental layout of ISIS is illustrated in Figure 2.10.

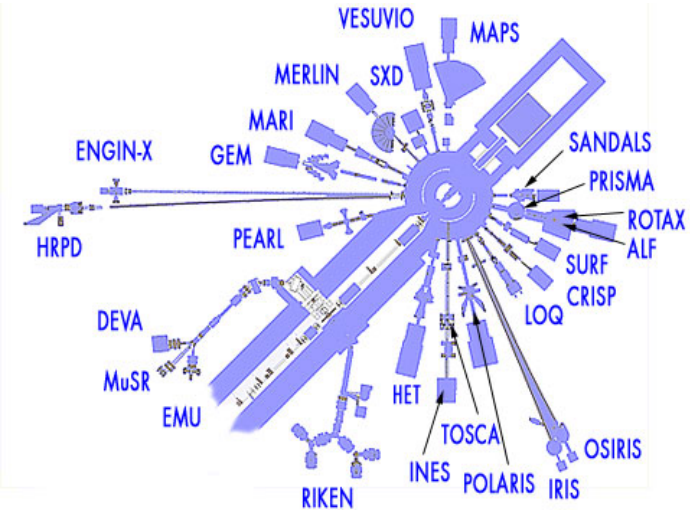

Figure 2.10 The experimental layout at ISIS[15].

2.3.3.1 The HiPr: PEARL Diffractometer [16]

The PEARL High Pressure Facility is a medium resolution and high flux diffractometer that has been especially adapted for data collection from the Paris-Edinburgh pressure cell. A schematic drawing of the instrument is shown in Figure 2.11. There are eleven detector modules in total, each comprising 120 Li-doped ZnS scintillators, which are divided between two separate banks. The main detector bank consist of nine of these modules covering $83^\circ < 2\theta < 97^\circ$, giving access to a *d*-spacing range of ~0.5-4.1 Å. This bank is used for the transverse, or through-anvil, scattering geometry of the Paris-Edinburgh cell. The remaining 2 modules make up the longitudinal bank detector which is accessed in the longitudinal or through-gasket setting covering $20^\circ < 2\theta < 40^\circ$ and $100^\circ < 2\theta < 120^\circ$ allowing a d-spacing range of ~0.5-10 Å to be studied. For the experiments in this thesis only the main detector bank was used. Measurements can be performed at pressures up to 25 GPa at temperatures between 90 and 350 K.

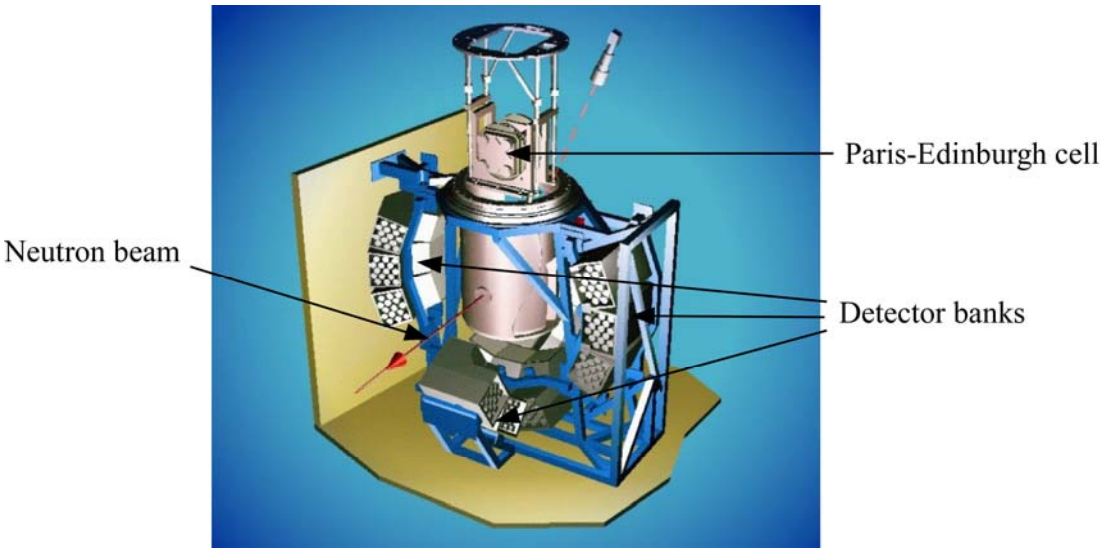

Figure 2.11 The instrument set-up at HiPr:PEARL[16].

2.3.3.2 The Paris-Edinburgh Cell

The pressure cell used for the neutron diffraction experiments in this work is the Paris-Edinburgh cell (PEC). It was developed in 1992[17] which meant that pressures above 5 GPa could be obtained for the first time despite the large sample

volume required for neutron diffraction (around 10^6 more than for powder X-ray diffraction). Pressures of up to 10 GPa can be generated on sample volumes of ~100 mm^3 and, pressures of up to 30 GPa can be achieved on sample volumes of ~30 mm^3[18]. The PEC is adapted to time-of-flight techniques at a fixed scattering angle which means that it is possible to collect powder patterns with minimal contamination signals from the parts of the cell. Structural information can then be obtained from the data by Rietveld refinement techniques. Furthermore, in the last few years, a new PEC has been developed that can be used at facilities with continuous neutron sources for angle-dispersive powder diffraction methods[18, 19].

The PEC consists of a portable hydraulic press, weighing about 50 kg, with the capacity of supplying a load of 250 tonnes *in situ* onto a sample of 100 mm^3 placed in a gasket between two opposed anvils. A schematic of the cell is given in Figure 2.12. The gasket is made from a 1:1 titanium-zirconium alloy, which is a null scatterer, and is of an encapsulated design that prevents the pressure-transmitting medium from coming into contact with the anvils. The pressure media used in PEC's are similar to those used for DAC's, although any media containing hydrogen has to be deuterated.

There are two types of anvils available depending on the pressure requirement. Tungsten carbide anvils are the standard used for pressures up to 10 GPa. To achieve higher pressures, these have to be replaced by anvils made from dies of sintered diamond[20]. Because the WC anvils are opaque it is not possible to use the ruby fluorescence method for pressure calibration. Instead, a pressure marker made from NaCl or Pb is loaded into the TiZr gasket along with the sample. Both of these compounds have known high-pressure equations of state and adopt cubic structures with the space group $Fm\bar{3}m$. The cell volume is obtained from refinement of the diffraction patterns and the pressure is then calculated by the equation of state.

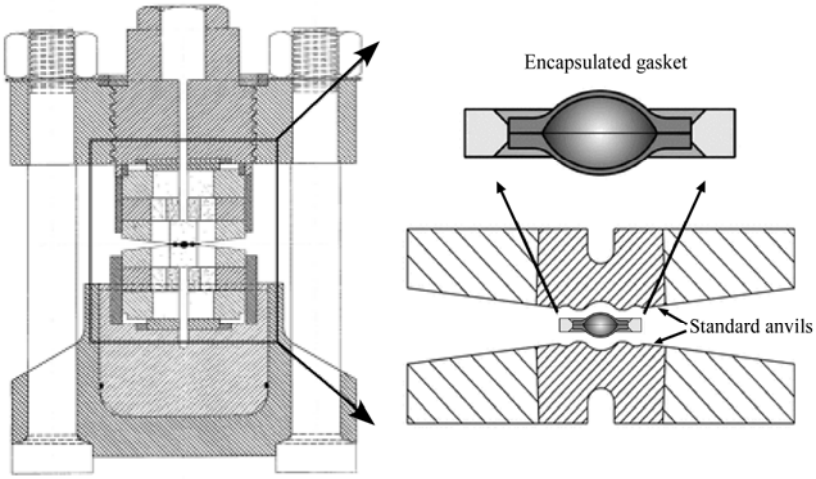

Figure 2.12 The Paris-Edinburgh cell with a standard anvil and gasket configuration.

2.4 The Rietveld Method

The Rietveld method[21, 22] is a technique utilised to refine crystal structures from X-ray and neutron powder diffraction data. Due to the random orientation of crystallites in a polycrystalline sample, a large amount of overlap of independent Bragg peaks occur and information is lost, particularly in low symmetry materials. In a Rietveld refinement the individual reflections are not analysed. Instead, a curve fitting procedure is used over the entire pattern, where the observed intensity is described as:

$$y_i = y_{i\,back} + \sum_i y_{i\,bragg}^{(i)} \qquad (2.9)$$

where y_i and y_{iback} is the observed and background intensity, respectively and $\sum_i y_{i\,bragg}^{(i)}$ is the sum of the contributions of reflections close to the powder pattern step i. A mathematical expression that includes factors relating to both the crystal structure and other non-diffraction terms is used to calculate the contribution from reflections.

The difference between the observed and calculated profiles is minimised by least squares refinement and it is therefore very important to have a good structural starting model including space group, lattice parameters and atomic co-ordinates.

The powder diffraction data must be in digitised form so that a numerical intensity value, y_i, is recorded at each of several thousand equal steps, i, in the pattern. In the least-squares refinement, a best fit to all of the y_i's is sought simultaneously and the quantity minimised is the residual, S_y:

$$S_y = \sum w_i (y_{i,obs} - y_{i,calc})^2 \qquad (2.10)$$

where $w_i = 1/y_{i,obs}$, $y_{i,obs}$ is the observed intensity at the i^{th} step and $y_{i,calc}$ is the calculated intensity of the i^{th} step.

At any randomly chosen point, i, in the pattern, there is generally a contribution from many Bragg peaks to the intensity, $y_{i,obs}$. The calculated intensity, $y_{i,calc}$, at the point i is therefore determined by summing the contributions from all the Bragg reflections, K, close to the step and it also includes a background intensity[23].

$$y_{i,calc} = s\sum_K L_K |F_K|^2 \phi(2\theta_i - 2\theta_K) P_K A + y_{i,back} \qquad (2.11)$$

where

s is the scale factor,

K correspond to the Miller indices, $h\ k\ l$, for a Bragg reflection,

L_K contains the Lorentz, polarization and multiplicity factor,

ϕ is the reflection profile function,

P_K is the preferred orientation factor,

A is an absorption factor,

F_K is the structure factor for the Bragg reflection with miller indices $h\ k\ l$,

$Y_{i,back}$ is the background intensity at the i^{th} step

There are many ways to model the background intensity at the i^{th} step. For example, from a linear interpolation between two points, by using a specified background function such a Chebychev polynomial[24] or by manually inserting a table of background intensities. In this work the background was modelled with the Chebyshev and linear interpolation functions.

In Rietveld refinement it is important to have accurate peak shape fitting as both the instrument and sample affects the shape and position of the Bragg peaks. For constant wavelength experiments the instrumental broadening is almost fully Gaussian and the Full Width at Half Maximum(FWHM) is given by:

$$\tau_K = U\tan^2\theta_K + V\tan\theta_K + W \qquad (2.12)$$

Where *U*, *V* and *W* are refinable parameters.

A pseudo-Voight[25] function was used in the refinements of the neutron diffraction data in this work. It takes into account both the instrumental (Gaussian, *G*) and sample (Lorentzian, *L*) broadening which is essential as high-resolution X-ray and neutron diffractometers have a narrow instrument profile and broadening due to sample defects becomes significant.

$$\phi(2\theta_i - 2\theta_K) = \eta L + (1-\eta)G \qquad (2.13)$$

where η is a complex function which depends on the Full Width at Half Maximum for the Gaussian (Γ_{GK})and Lorentzian (Γ_{LK}) broadening of the K^{th} bragg reflection:

$$\tau_{GK} = (U\tan^2\theta_K + V\tan\theta_K + W + \frac{Z}{\cos^2\theta_K})^{1/2} \qquad (2.14)$$

$$\tau_{LK} = X\tan\theta_K + \frac{Y}{\cos\theta_K} \qquad (2.15)$$

Z is the Scherrer coefficient for Gaussian particle size broadening whilst *X* and *Y* model the Lorentizian strain and the Scherrer broadening respectively.

The parameters that can be refined by the Rietveld method, in addition to those already mentioned include the cell parameters, the atomic coordinates, the temperature factors, site occupancies and intensity corrections. In the refinement process the parameters will be adjusted until S_y is minimised i.e. when the best fit between the calculated and observed pattern is obtained. Having a starting model close to the correct one will prevent the system from diverging or reaching a false minimum. The goodness of fit of the least-square refinement and whether a true minimum has been achieved can be evaluated from the residual *R*-values.

$$R_f = \frac{\sum \left| (I_{K,obs})^{1/2} - (I_{K,calc})^{1/2} \right|}{\sum (I_{K,obs})^{1/2}} \qquad R\text{-structure factor} \qquad (2.16)$$

$$R_p = \frac{\sum (y_{i,obs} - y_{i,calc})^2}{\sum (y_{i,obs})} \qquad R\text{-pattern} \qquad (2.17)$$

$$R_{wp} = \left| \frac{\sum w_i (y_{i,obs} - y_{i,calc})^2}{\sum w_i y_{i,obs}^2} \right| \qquad R\text{-weighted pattern} \qquad (2.18)$$

$$\chi^2 = \sum_I \frac{w_i (y_{i,obs} - y_{i,calc})^2}{N - p + C} \qquad \text{Goodness of fit parameter} \qquad (2.19)$$

Where $I_{K,obs}$ and $I_{K,calc}$ are the observed and calculated intensities assigned to the K^{th} bragg reflection at the end of the refinement cycle and N, p and C are the number of observations, refined parameters and constraints respectively. It should be noted that, as well as having low residual R factors from the refinement, the refined model has to make sense both chemically and physically. All magnetic and structural refinements of powder diffraction data in this thesis were performed with the General Structure Analysis System (GSAS) program suite[24].

2.4.1 Magnetic symmetry

Describing magnetic ordering is more complex than describing structural ordering and because of overlap of symmetry related reflections, the power of powder diffraction is limited with regards to determining the details of a magnetic structure. For example, in tetragonal systems the diffraction patterns from a set of atoms with spins in the *ab*-plane will all be the same at all angles. Only from a single crystal measurement would it be possible to determine at which angle the moments are arranged in the *ab*-plane[26].

As mentioned previously, the magnetic unit cell may be doubled in one or more directions compared to the chemical unit cell. This can also be seen as an extension of the symmetry through the inclusion of anti-translation leading to an expansion from the 14 standard Bravais lattices in ordinary crystallography to 36

magnetic Bravais lattices[12]. From these, 1421 space groups can be developed by addition of a new antisymmetry operation, designated *R*, which reverses the direction of the magnetic moment. Including the 230 standard crystallographic space groups, this gives a total of 1651 so called 'Shubnikov groups' applicable to materials with ferromagnetic and antiferromagnetic structures[27].

Any symmetry operation, *s*, can be combined with *R* resulting in the new operation *s*' which applies the same symmetry but also adds a spin flip. The spin flip is also sometimes referred to as time-reversal and the pre-fix "anti" is often used to differentiate between unprimed and primed operations. In magnetic symmetry, the spin is described as an axial vector connected with a current loop. The symmetry operations are applied to the current loop and the direction of the moment will be given by the right hand screw rule. Examples of the effect of the primed and unprimed version on the magnetic moment for the rotation and mirror symmetry operations are given in Figure 2.13.

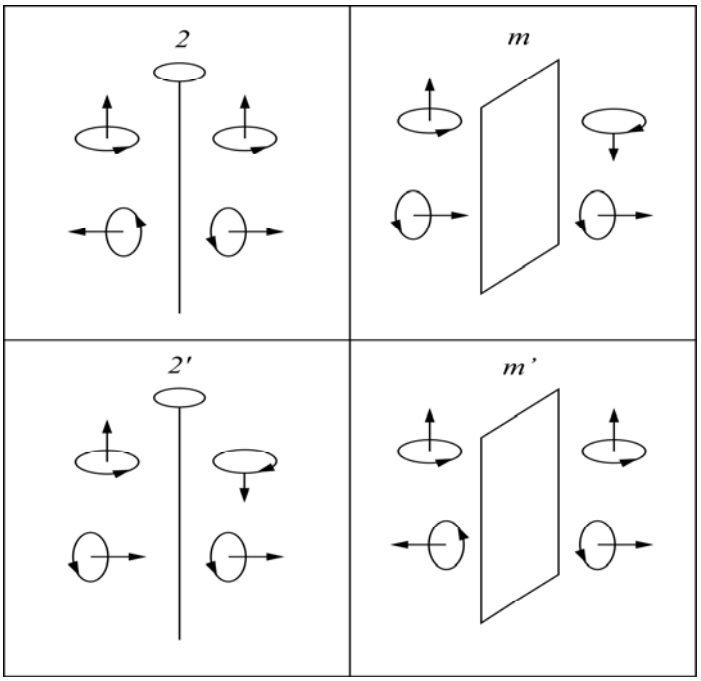

Figure 2.13 The correlation between magnetic moments related by the unprimed (upper) and primed (lower) for the mirror plane (right) and rotation (left) operations[12].

2.5 Bond Valence Sums (BVS)

Bond valences determined from experimentally measured bond lengths can be used to derive atomic valences which can be helpful in several ways when determining and evaluating crystal structures. Although it is possible to distinguish charges of atoms (and hence the charge ordered model) for a material by comparing the average metal-oxygen distances for each of the crystallographically distinct metal ions, bond valence sums (BVSs) provides a more accurate estimate of the different metal ion valences.

The modern bond valence sum method was developed from Pauling's concept of valences from ionic radii and bond numbers of metals and intermetallic compounds[28, 29], later extended to include metal oxides[30, 31]. It implies that the sum of the bond valences around an atom is equal to the formal valence of the atom[32] and it can be used to assess both ionic and covalent bonds. However, a closer correlation between the bond lengths and bond valences are observed for ionic compounds.

As stated by Brown[33, 34], the relationship between the bond valence sum, V_i, for an atom and the length of its bonds d_{ij} is

$$V_i = \sum_j \exp\left(\frac{R_0 - d_{ij}}{B}\right) \qquad (2.20)$$

where B is a global constant equal to 0.37 Å and R_0 is the derived bond valence parameter[33] characteristic of the atom pair i and j . Both parameters are empirically determined[35]. Because the value of the bond valence parameter varies for different oxidation states of the same metal, e.g. Cu^{2+} and Cu^{3+}, two BVSs will be obtained; one for the lower, V_L, and one for the higher, V_H, oxidation state. An intermediate valence state, V, may be estimated from these obtained BVSs by using the formula[36]

$$V = \frac{L(V_H - V_L) - (H - L)V_L}{(V_H - V_L) - (H - L)} \qquad (2.21)$$

with H and L represent the higher and lower formal oxidation states. There are also computer programmes available for calculating average valances e.g. Valence[37]. In

this work the BVSs and average valences were calculated manually using the above formulae.

2.6 References

1. W. Massa, *Crystal structure determination*; Springer-Verlag: Berlin, 2000.
2. V. Favre-Nicolin and R. Cerny, *J. Appl. Cryst.*, **35**, 734 (2002).
3. W.I.F. David, K. Shankland, L.B. McCusker and C. Baerlocher, *Structure determination from powder diffraction data*; OUP: Oxford, 2002.
4. http://www.srs.ac.uk/srs/stations/station9.5hpt.htm [cited 2008 May].
5. http://www.srs.ac.uk/srs/stations/station9.8.htm [cited 2008 May].
6. E. Eremets, *High Pressure Experimental Methods*; Oxford University Press inc.: New York, 1996.
7. A. Jayaraman, *Rev. Sci. Instr.*, **57**, 1013 (1986).
8. R. Miletich, D.R. Allan and W.F. Kuhs, *Rev. Min. Geochem.*, **41**, 445 (2000).
9. L. Merrill and W.A. Bassett, *Rev. Sci. Instr.*, **45**, 290 (1974).
10. D.R. Allan, R. Miletich and R.J. Angel, *Rev. Sci. Instr.*, **67**, 840 (1996).
11. G.J. Piermarini, S. Block, J.D. Barnett and R.A. Forman, *J. Appl. Phys.*, **46**, 2774 (1975).
12. G.E. Bacon, *Neutron diffraction*; Clarendon Press: Oxford, 1975.
13. R.P.O. Y. A. Izyumov, *Magnetic Neutron Diffraction*; Plenum Press: New York, 1970.
14. http://www.ill.eu/instruments-support/ [cited 2008 May].
15. http://www.isis.rl.ac.uk/instruments/index.htm [cited 2008 may].
16. http://www.isis.rl.ac.uk/crystallography/hipr/index.htm [cited 2008 May].
17. J.M. Besson, R.J. Nelmes, G. Hamel, J.S. Loveday, G. Weill and S. Hull, *Physica B*, **180**, 907 (1992).
18. S. Klotz, T. Strassle, G. Rousse, G. Hamel and V. Pomjakushin, *Appl. Phys. Lett.*, **86**, 031917 (2005).
19. S. Klotz, G. Hamel and J. Frelat, *High Press. Res.*, **24**, 219 (2004).

20. S. Klotz, J.M. Besson, G. Hamel, R.J. Nelmes, J.S. Loveday, W.G. Marshall and R.M. Wilson, *Appl. Phys. Lett.*, **66**, 1735 (1995).
21. H.M. Rietveld, *Acta Cryst.*, **22**, 151 (1967).
22. H.M. Rietveld, *J. Appl. Cryst.*, **2**, 65 (1969).
23. R.A. Young, *The Rietveld Method*; Oxford University Press: Oxford, 1995.
24. A.C. Larson and R.B.V. Dreele, *General Structureal Analysis System (GSAS)*; Los Alamos National Laboratory: Los Alamos, 1990.
25. P. Thompson, D.E. Cox and J.B. Hastings, *J. Appl. Cryst.*, **20**, 79 (1987).
26. G. Shirane, *Acta Cryst.*, **12**, 282 (1959).
27. A.V. Shubnikov and N.V. Belov, *Colored Symmetry*; Oxford Pergamon Press: New York, 1964.
28. L. Pauling, *J. Am. Chem. Soc.*, **51**, 1010 (1929).
29. L. Pauling, *J. Am. Chem. Soc.*, **69**, 542 (1947).
30. A. Bystrom and K.A. Wilhelmi, *Acta Chem.Scan.*, **5**, 1003 (1951).
31. W.H. Zachariasen, *Acta Cryst.*, **16**, 385 (1963).
32. I.D. Brown and R.D. Shannon, *Acta Cryst. A*, **A 29**, 266 (1973).
33. I.D. Brown and D. Altermatt, *Acta Cryst. B*, **41**, 244-247 (1985).
34. I.D. Brown, *J. Chem. Edu.*, **77**, 1070 (2000).
35. M. O'Keeffe and A. Navrotsky, *Structure and bonding in crystals*; Academic Press Inc.: New York, 1981.
36. J.P. Attfield, *Solid State Sci.*, **8**, 861 (2006).
37. I.D. Brown, *J. Appl. Cryst.*, **29**, 479 (1996).

Chapter 3

Diffraction experiments on the charge-ordered perovskite $BiNiO_3$

3.1 Introduction

Transition metal oxides make up quite a remarkable group of materials which offer a fascinating field of research. They exhibit a wide variety of unusual electronic and magnetic properties and have generated much interest, in particular since the discovery of high temperature superconductivity in the layered cuprates such as $La_{2-x}Sr_xCuO_4$[1]. In these materials the electrical resistance drops to zero below a transition temperature, T_c. Another exciting phenomenon is Colossal Magnetoresistance (CMR), i.e. a large change in the electronic resistivity at the Curie temperature upon the application of a magnetic field, which is observed in the manganese oxides[2, 3]. Some transition-metal oxides, for example $BaTiO_3$[4], have ferroelectric properties that arise from a displacement of cations with an electrical charge, generating a net electrical dipole moment. Other compounds, such as $BiFeO_3$[5], show a combination of magnetic and ferroelectric functionalities.

The electronic and magnetic properties of transition metals are strongly affected by structural changes. One of the most common structures seen among the materials described is that of the ABO_3 perovskite type, where A is a large cation like alkali, alkali-earth or rare-earth elements and B is usually a transition metal. The crystal lattice consists of corner sharing BO_6 octahedra with the 12-coordinate A cations filling the central sites between them. The relationship between the ionic radii, *r*, of A, B and O determines the crystal structure and the perovskites will have the ideal cubic symmetry, space group $Pm\bar{3}m$, if

$$r_A + r_O = \sqrt{2}\,(r_B + r_O) \qquad (3.1)$$

However, in general the A cations are too small to satisfy this condition and the BO_6 octahedra are tilted to fill the voids around them. These rotations lower the symmetry and for distorted perovskites a tolerance factor[6], *t*, is introduced to equation 3.1

$$r_A + r_O = t\sqrt{2}\,(r_B + r_O) \qquad (3.2)$$

For the ideal perovskites, *t* is equal to 1, but as the distortion increases, *t* becomes smaller than 1. Structural distortions strongly affect the physical properties of perovskite materials and these can therefore be varied by chemical substitution, temperature or pressure. It is relatively well known how temperature and chemical substitution influences the phase transitions of perovskites. A rise in temperature and replacing the A cation with another one of larger radius reduces the tilting of the octahedra and the symmetry increases. Many materials undergo a series of phase transitions as the temperature is increased until the ideal cubic structure is finally obtained. The effect of pressure on the perovskite structure is less studied.

Charge ordering in mixed valence transition metal oxides is a common phenomenon but it is of great interest because of its association with exotic conducting properties such as superconductivity in K- and Pb-doped $BaBiO_3$[7, 8] and colossal magnetoresistance (CMR) in layered manganites, for example $La_{0.5}Ca_{0.5}MnO_3$[9]. In addition, charge disproportionation of high-transition metal valence states also occur on the B-sites in the perovskites $CaFeO_3$[10, 11] and $RNiO_3$ (R = Y, Pr-Lu)[12-15]. The latter is one of the rare groups of oxides to exhibit metallic conductivity. Furthermore, except for $LaNiO_3$[16], they show a metal to insulator transition with decreasing temperature. The transition temperature (T_{MI}) is strongly influenced by the degree of structural distortion and application of pressure[12, 17, 18]. As the size of the R cation is reduced, the Ni-O-Ni bond angle, which determines the degree of overlapping of the Ni *3d* and O *2p* orbitals (Figure 3.1), becomes smaller[16] and T_{MI} is increased. The opposite occurs when an external pressure is applied. At low temperatures, $RNiO_3$ compounds with R ≠ La also exhibit an intricate antiferromagnetic order with the Ni ions coupled ferromagnetically and antiferromagnetically in an alternating manner[19, 20]. For larger R-cations (Pr and Nd), the magnetic ordering temperature (T_N) coincides with T_{MI} but as the size of R is reduced the difference between the two increases and $T_N < T_{MI}$, indicating the

decoupling of the electronic and magnetic behaviours. The whole series of $RNiO_3$ compounds (except for those containing Ce, Pr and Tb) were first prepared in 1971[21], but with the exception of $LaNiO_3$, no further studies were published up until 1989[22]. The reason for this was the extreme experimental conditions required for the synthesis which meant that only very small sample volumes could be produced. In $RNiO_3$ perovskites, Ni is in its 3+ oxidation state and increasingly high pressure is required to stabilise the Ni^{3+} ion as the size of the rare earth cation is reduced. However, the development of new high-pressure solid state reactions, using a piston-cylinder press, allowed for synthesis under moderately high pressures, which meant that larger sample volumes of even the compounds with the smallest rare earth cations, could be obtained[23]. High-pressure/high-temperature techniques have also made it possible to synthesise perovskites that have a low tolerance factor at ambient pressure but can be stabilised at high pressure and then quenched. Furthermore, high-pressure reactions in the presence of an oxidizing agent, such as $KClO_4$, may be used to stabilise transition metals in high oxidation states.

In contrast to other $RNiO_3$ compounds, $BiNiO_3$ does not contain Ni^{3+} but high pressure and temperature is required to stabilise the much distorted perovskite structure. It was first reported to have been synthesised in 1967 under high pressure with cubic symmetry but no detailed structural data were provided[24-26]. However, more recently, it was successfully prepared under a pressure of 6 GPa using a conventional cubic anvil-type high pressure apparatus[27]. The quality of the samples was strongly affected by the heating rate and to minimise the amount of impurities a rapid heating up to a 1000˚C in 1 min was required. Unfortunately, this process yields very small sample volumes, and the synthesis has to be repeated numerous times to provide a sufficient amount of sample for neutron diffraction and physical properties measurements.

Bond Valence Sum (BVS)[28, 29] calculations based on the metal oxygen distances taken from a synchrotron X-ray powder diffraction study[27] of $BiNiO_3$ showed that the oxidation state distribution is $Bi^{3+}_{0.5}Bi^{5+}_{0.5}Ni^{2+}O_3$ (Figure 3.2) with ordering of Bi^{3+} and Bi^{5+} charges on the A-site. The Ni^{2+} was also confirmed by photoemission and X-ray absorption experiments[30].

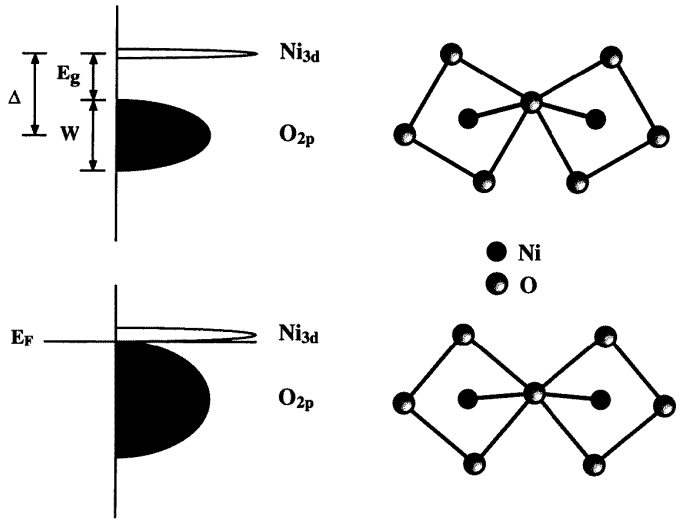

Figure 3.1 Representation of the narrowing of the O 2*p*-derived valence band below T_{MI} caused by less efficient overlap of the O 2*p* and Ni 3*d* orbitals as the Ni–O–Ni superexchange angle decreases[17].

This is very unusual as other bismuth containing perovskites such as $BiCrO_3$[31], $BiCoO_3$[32], $BiMnO_3$[33] and Bi_2NiMnO_6[34], which are also prepared under high pressure, all contain Bi^{3+} on the A-site. At ambient pressure, $BiNiO_3$ has a centrosymmetric triclinic structure (space group $P\bar{1}$) with two inequivalent Bi and four Ni sites and lattice parameters a = 5.3852(20, b = 5.6498(2), c = 7.7083(3) Å, α = 91.9529(10) °, β = 89.8097(9) °, γ = 91.5411(9)°[35]. Consequently, $BiNiO_3$ has been shown to be an insulating antiferromagnet. However, although NiO does not metallise below 50 GPa[36], $BiNiO_3$ undergoes a pressure-induced insulator to metal transition at a moderate pressure of 3-4 GPa[37]. Synchrotron X-ray diffraction studies have shown that this transition is accompanied by a structural change to an orthorhombic GdFeO3-type perovskite superstructure and subsequently a suppression of the charge disproportionation. However, it was not clear from this study whether the transition involves melting of the charge order (Bi^{3+}+Bi^{5+}→2Bi^{4+}) or if some charge transfer from Ni to Bi takes place. A similar structural change to the orthorhombic metallic symmetry can also be induced by La[35] or Pb[38] substitution of the bismuth.

Magnetic susceptibility measurements[27] on $BiNiO_3$ showed that the system becomes magnetically ordered below 300 K with a negative Weiss constant

(θ = -262 K) indicating that the dominant spin-spin interactions are antiferromagnetic. The estimated value of the Curie constant (C = 1.05 emuKmol^{-1}) was close to that expected for S = 1 Ni^{2+}, confirming the divalent nature of the Ni ions as suggested from the structural data. In addition, ferromagnetic hysteresis was observed in the *M-H* data and this was ascribed to weak ferromagnetism as a result of spin canting.

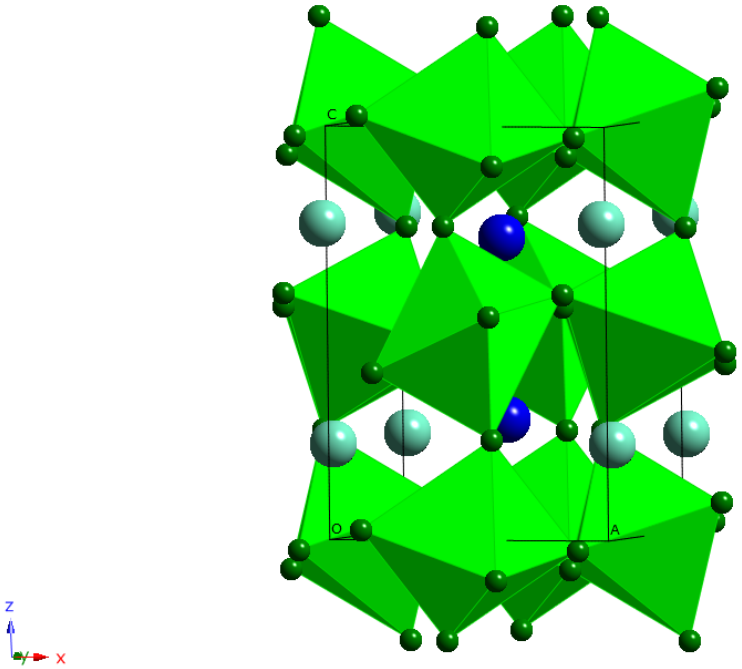

Figure 3.2 Crystal structure of $BiNiO_3$, with light and dark blue spheres corresponding to Bi^{3+} and Bi^{5+}, respectively, and the NiO_6 octahedra in green.

In this work, neutron powder diffraction in combination with high pressure has been used to obtain accurate atomic coordinates from which bond valence sums can be calculated and the charge distribution in the high pressure phase examined. Furthermore, as a continuation of the work to characterise this compound, a second neutron diffraction study was undertaken to determine the magnetic structure and examine the crystal structure at low temperatures.

3.2 Experimental

3.2.1 Synthesis

Polycrystalline samples of $BiNiO_3$ were prepared by high pressure synthesis by S. Ishiwata at the Institute for Chemical Research at Kyoto University in Japan[27]. A precursor was obtained by dissolving stoichiometric amounts of Bi_2O_3 and Ni in Nitric acid and heating the mixture at 750°C in air for 12 h. The resulting fine powders were sealed in a gold capsule together with the oxidising agent $KClO_4$ in a weight ration of 4:1. The sample was then put in a conventional cubic anvil-type high pressure apparatus and treated at 6 GPa and 1000°C for 30 minutes. Finally, the sample was removed from the capsule, crushed and washed with distilled water to dissolve the KCl.

3.2.2 Neutron diffraction measurements

Time-of-flight neutron powder diffraction patterns were recorded at room temperature on the PEARL High Pressure instrument at the ISIS facility to examine the effect of high pressure on the A-site charge ordering in $BiNiO_3$. About 90 mm^3 of the sample was loaded into a Paris-Edinburgh cell[39] using a 4:1 methanol:ethanol mixture as a pressure medium and a pellet of lead as pressure calibrant. Data were collected at pressures up to 7.6 GPa in the transverse geometry giving access to the scattering angle range $83° \leq 2\theta \leq 97°$.

A low temperature structural and magnetic study was carried out using neutron diffraction data from the instrument Super-D2B at the Institute Laue-Langevin. The 3 g sample was contained in a cylindrical vanadium can and neutron powder diffraction data were collected in the angular range $10° \leq 2\theta \leq 150°$ at temperatures of 5, 100, 200 and 300 K using $\lambda = 2.39$ Å. This instrument features a bank of 128 collimated, linear-wire, position sensitive detectors separated by 1.25°, stepped in 0.05 intervals. All of the neutron diffraction patterns were fitted by the Rietveld method[40] using the GSAS program[41].

3.3 Results and discussion

3.3.1 Room temperature and high pressure neutron diffraction studies

Time-of-flight neutron diffraction patterns of $BiNiO_3$ were collected at increasing pressures up to 7.6 GPa. The diffraction patterns below 4 GPa were similar to the ambient pressure profile (0.1 MPa) and they were all fitted with the triclinic $P\bar{1}$ symmetry, using the structure previously determined from synchrotron X-ray diffraction data[27], as a starting model. This has a $\sqrt{2}a_p \times \sqrt{2}a_p \times 2a_p$ superstructure, a_p being the cubic perovskite lattice parameter, with two distinct crystallographic Bi sites and four Ni sites. The sample consisted of 79.3% $BiNiO_3$, 3.6% NiO and 17.1% Pb pressure standard by weight, with small contributions from WC and Ni in the anvils which were also fitted. A good fit to the data was obtained and the refined structural model was in good agreement with that of the previous X-ray study[27]. A drastic change in the diffraction pattern was observed above 4 GPa as illustrated in Figure 3.3 with the merging of peaks showing that the higher symmetry, orthorhombic phase is formed. This high pressure phase was indexed in space group *Pbnm*, the same $GdFeO_3$ type structure as the metallic phase of $RNiO_3$[23] with one site each for the bismuth and nickel atoms, and this gave good fits to the data. The starting values for the lattice parameters, were taken from a synchrotron X-ray diffraction study by Ishiwata *et al*[35]. The possibility of a distorted $GdFeO_3$ type superstructure found in other Bi and Ni containing perovskites was also examined, assuming the acentric $BiInO_3$ model, space group $Pna2_1$[32], and a Ni-dispropotionated monoclinic $P2_1/n$ $YNiO_3$ structure[15]. However, there was no improvement to the fits and the additional atomic displacements were insignificant. Figures 3.4 and 3.5 show the calculated, observed and difference plots for all data sets. Refinement results for the 0.1 and 7.6 GPa data sets are given in Tables 3.1-3.4. Listings of results for the other pressure points can be found in Appendix A.

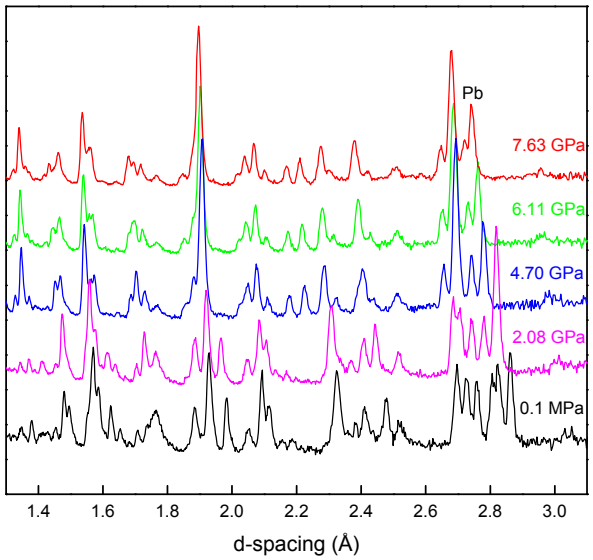

Figure 3.3 Diffraction patterns of $BiNiO_3$ at increasing pressure showing the triclinic to orthorhombic phase transition with the peak from the Pb pressure standard indicated.

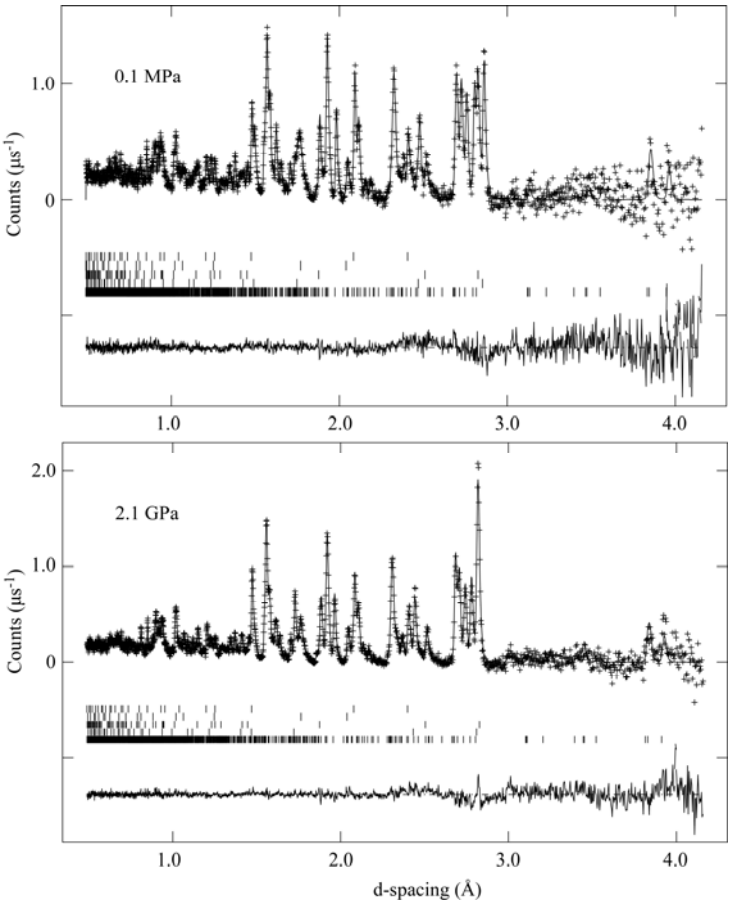

Figure 3.4 The observed, calculated and difference plots for $BiNiO_3$ at ambient pressure and 2.1 GPa. The reflection markers are $BiNiO_3$, Pb, WC, Ni and NiO from bottom to top.

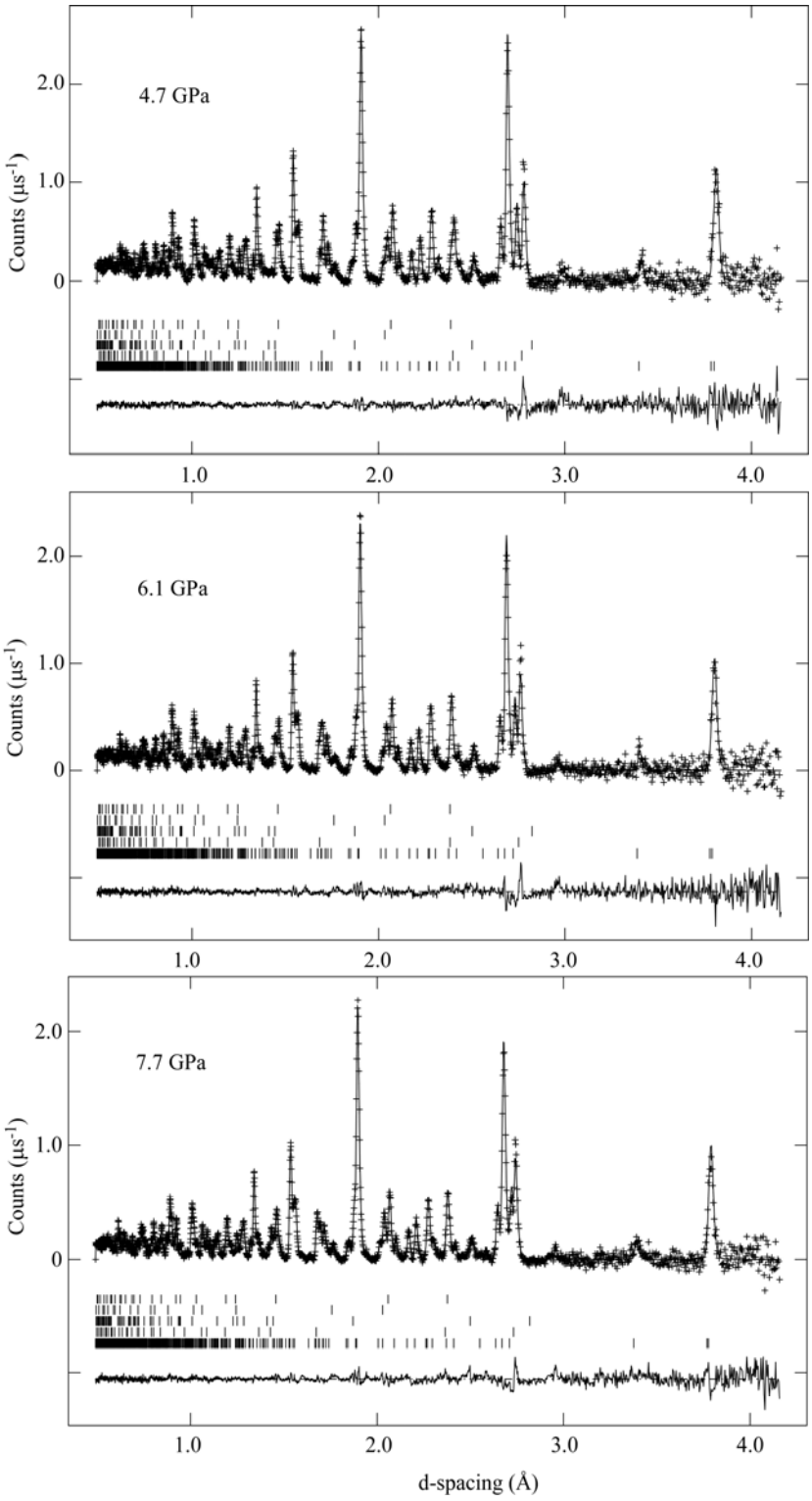

Figure 3.5 The observed, calculated and difference plots for $BiNiO_3$ at ambient pressure 4.7, 6.1 and 7.6 GPa. The reflection markers are $BiNiO_3$, Pb, WC, Ni and NiO from bottom to top.

Table 3.1

Crystallographic parameters and Rietveld reliability factors for $BiNiO_3$ at 0.1 MPa and 300 K.

Space group *P-1*, with a = 5.3946(5) Å, b = 5.6524(5) Å, c =7.7136(6) Å, α = 92.182(7)°, β = 89.777(6)° and γ = 91.703(5)°					
Atom	Site	x	y	z	$U_{iso}\times100$ (Å^2)
Bi1	2i	0.0029(15)	0.0447(12)	0.2324(9)	0.41(11)
Bi2	2i	0.5089(15)	0.4442(14)	0.7217(9)	0.41(11)
Ni1	1d	0.5	0	0	0.28(6)
Ni2	1c	0	0.5	0	0.28(6)
Ni3	1f	0.5	0	0.5	0.28(6)
Ni4	1g	0	0.5	0.5	0.28(6)
O1	2i	-0.1450(19)	0.4712(18)	0.2547(15)	0.03(6)
O2	2i	0.3925(19)	0.0847(17)	0.7555(13)	0.03(6)
O3	2i	0.8403(19)	0.1796(17)	-0.0291(13)	0.03(6)
O4	2i	0.3183(19)	0.3291(17)	0.0876(14)	0.03(6)
O5	2i	0.2203(19)	0.7665(18)	0.4109(13)	0.03(6)
O6	2i	0.6602(19)	0.6844(16)	0.5471(13)	0.03(6)
Reliability factors: χ^2 = 1.77, R_{wp} = 2.75%, R_p = 4.85%, R_{F2} = 4.17%					

Table 3.2

Crystallographic parameters and Rietveld reliability factors for $BiNiO_3$ at 7.6 GPa and 300K.

Space group *Pbnm*, with a = 5.2835(3) Å, b = 5.4336(4) Å and c = 7.5551(5) Å					
Atom	Site	x	y	z	$U_{iso}\times100$ (Å^2)
Bi1	4c	-0.0074(8)	0.0489(3)	0.25	0.41(5)
Ni1	4b	0	0.5	0	0.09(4)
O1	8d	0.6778(5)	0.2977(5)	0.0369(4)	0.50(4)
O2	4c	0.0845(8)	0.4802(8)	0.25	0.48(4)
Reliability factors: χ^2 = 2.543, R_{wp} = 2.42 %, R_p = 3.72 %, R_{F2} = 5.16 %					

Table 3.3

Calculated bond distances and angles for $BiNiO_3$ at 0.1 MPa and 300 K.

Distances (Å)					
Bond	Length	Bond	Length	Bond	Length
Bi1-O1	3.326(13)	Bi2-O1	2.040(13)	Ni1-O2 (x2)	2.054(9)
Bi1-O1	2.561(13)	Bi2-O1	3.455(14)	Ni1-O3 (x2)	2.087(10)
Bi1-O2	2.237(13)	Bi2-O2	2.134(12)	Ni1-O4 (x2)	2.210(10)
Bi1-O2	3.366(13)	Bi2-O2	3.692(11)	Ni2-O1 (x2)	2.122(11)
Bi1-O3	2.365(13)	Bi2-O3	3.087(13)	Ni2-O3 (x2)	1.988(9)
Bi1-O3	2.165(11)	Bi2-O3	3.676(12)	Ni2-O4 (x2)	2.120(10)
Bi1-O4	2.586(13)	Bi2-O4	3.086(13)	Ni3-O2 (x2)	2.094(10)
Bi1-O4	3.603(12)	Bi2-O4	2.115(12)	Ni3-O5 (x2)	2.078(11)
Bi1-O5	2.456(12)	Bi2-O5	3.467(13)	Ni3-O6 (x2)	2.051(9)
Bi1-O5	3.160(12)	Bi2-O5	2.144(11)	Ni4-O1 (x2)	2.049(12)
Bi1-O6	3.684(12)	Bi2-O6	2.095(13)	Ni4-O5 (x2)	2.030(11)
Bi1-O6	2.864(12)	Bi2-O6	2.349(12)	Ni4-O6 (x2)	2.158(10)
Average	*2.86(2)*	*Average*	*2.80(2)*	*Average*	*2.09(2)*
Angles (˚)					
Bond	Angle	Bond	Angle	Bond	Angle
O2-Ni1-O3	91.3(4)	O2-Ni3-O5	103.4(4)	Ni2-O1-Ni4	135.2(5)
O2-Ni1-O4	94.5(4)	O2-Ni3-O6	97.4(4)	Ni1-O2-Ni3	136.8(5)
O3-Ni1-O4	91.7(4)	O5-Ni3-O6	99.8(4)	Ni1-O3-Ni2	141.7(5)
O1-Ni2-O3	98.3(4)	O1-Ni4-O5	98.9(4)	Ni1-O4-Ni2	132.5(5)
O1-Ni2-O4	92.7(4)	O1-Ni4-O6	93.6(4)	Ni3-O5-Ni4	139.2(5)
O3-Ni2-O4	93.0(4)	O5-Ni4-O6	100.5(4)	Ni3-O6-Ni4	140.7(5)

The change of the structural parameters under pressure, going across the phase transition from triclinic to orthorhombic symmetry, is shown in Figure 3.6. The lattice parameters (*a, b* and *c*) and the unit-cell volume (*V*) decrease steeply across the transition and the change in volume from 2.1 to 4.7 GPa is 4.5%, in agreement with a previous high pressure synchrotron X-ray diffraction study[35]. This is reflected in the mean Bi-O and Ni-O distances which are both shorter in the high pressure phase than in the ambient pressure phase (Tables 3.3 and 3.4). There was no indication of phase coexistence in the 2.1 or 4.7 GPa data, although this would be expected at pressures close to the first-order metal-insulator transition.

The charge distribution in both the ambient and high pressure phase was examined using Bond Valence Sums (BVSs) which were calculated from the experimentally determined Bi-O and Ni-O distances using standard parameters [15, 28] for M = Bi^{3+}, Bi^{5+}, Ni^{2+} and Ni^{3+}. The results are listed in Table 3.5 and confirm that at ambient pressure the charge distribution is $Bi^{3+}_{0.5}Bi^{5+}_{0.5}Ni^{2+}O_3$. Above 4 GPa, a drastic change takes place and in the high pressure phase the BVSs for the single Bi and Ni sites are both close to 3 (3.32 and 2.93, respectively, at 7.6 GPa). There is a slight increase in the BVSs with pressure as the structure is compressed and the Bi-O and Ni-O bond lengths shorten but this is small in comparison to the major shift that occurs at the phase transition, illustrated in Figure 3.7. This shows that the high pressure phase has the charge distribution $Bi^{3+}Ni^{3+}O_3$ and that a complete one electron Ni→Bi transfer has occurred at the metal-to-insulator transition.

Table 3.4

Calculated bond distances and angles for $BiNiO_3$ at 7.6 GPa and 300 K

Distances (Å)					
Bond	Length	Bond	Length	Bond	Length
Bi1-O3 (×2)	2.616(4)	Bi1-O4	3.128(5)	Ni1-O1 (×2)	1.958(3)
Bi1-O3 (×2)	2.338(3)	Bi1-O4	2.393(4)	Ni1-O1 (×2)	1.946(3)
Bi1-O3 (×2)	2.563(4)	Bi1-O4	3.072(6)	Ni1-O2 (×2)	1.943(1)
Bi1-O3 (×2)	3.305(3)	Bi1-O4	2.265(6)		
		Average	*2.71(2)*	*Average*	*1.95(2)*
Angles (°)					
Bond		Angle		Bond	Angle
Ni1-O1-Ni1		152.7(2)		Ni1-O2-Ni1	152.1(1)

Table 3.5

Bond Valence Sums for $BiNiO_3$ at various pressures. Values were calculated with equations 2.20 and 2.21 using R_{ij} = 2.094 for Bi^{3+}, 2.06 for Bi^{5+}, 1.67 for Ni^{2+} and 1.686 for Ni^{3+}.

Pressure	Bi1	Bi2	Ni1	Ni2	Ni3	Ni4
0.1 MPa	3.17	5.07	1.69	1.93	1.92	1.91
2.1 GPa	3.30	4.95	1.89	1.99	1.85	2.15
4.7 GPa	3.26		2.79			
6.1 GPa	3.29		2.86			
7.7 GPa	3.32		2.93			

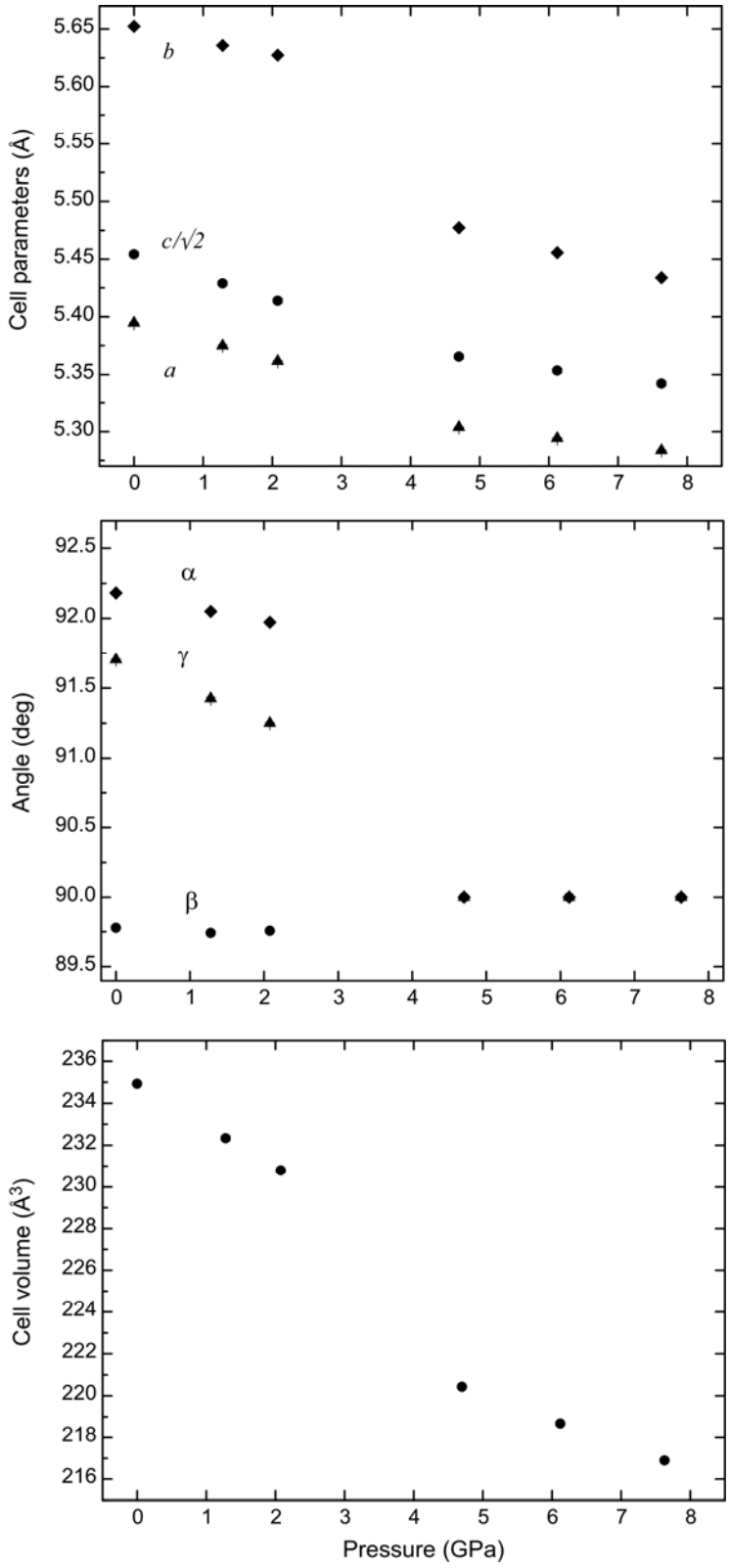

Figure 3.6 Pressure dependence of the $BiNiO_3$ cell parameters. The error bars are smaller than the size of the data points.

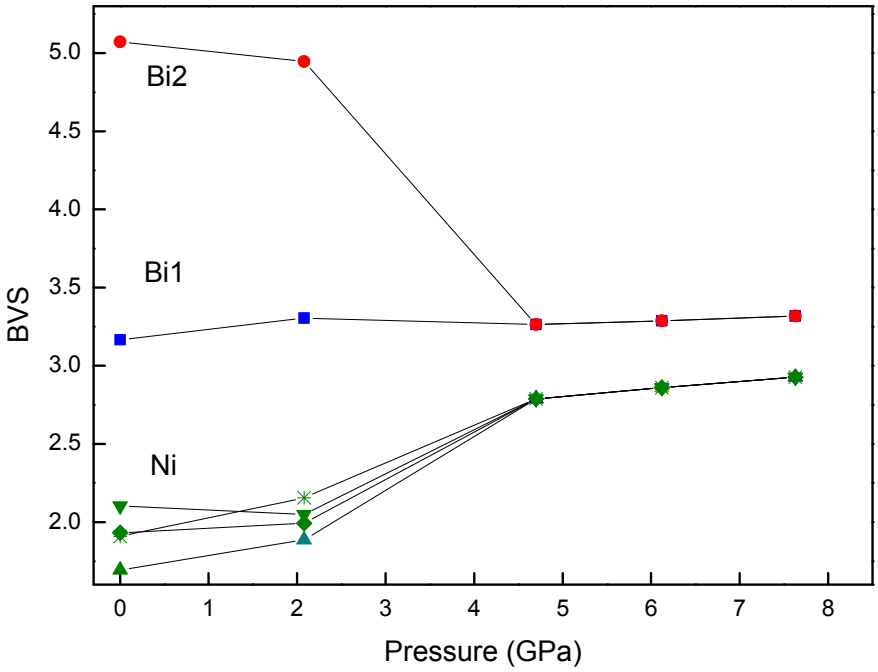

Figure 3.7 Bond-Valence sums for Bi and Ni at increasing pressures calculated from the Bi-O and Ni-O bond lengths.

3.3.2 Variable temperature neutron diffraction at ambient pressure

No structural transitions were observed on cooling $BiNiO_3$ to 5 K at ambient pressure and all of the diffraction patterns were therefore indexed on the triclinic $P\bar{1}$ structural symmetry model taken from a previously published room temperature synchrotron X-ray diffraction study of $BiNiO_3$[27]. The cell parameters, atomic co-ordinates and isotropic thermal factors were all refined. A pseudo-Voigt function was used to model the peak shape and the background was fitted using linear interpolation. The diffraction patterns showed the presence of a NiO impurity, including the (½ ½ ½) magnetic superstructure peak at $2\theta \approx 29°$, and some weak reflections from unidentified impurities in addition to the main phase $BiNiO_3$. The NiO impurity was refined in the cubic symmetry with an additional model needed for the magnetic structure.

This was fitted as a separate phase in the hexagonal settings taken from D. Rodic *et al*[42] with a doubling of the *c*-axis taking into account the magnetic superstructure. From the refined scale factors, the mass percentage of NiO was 5.04(7) %. The results of the refinements are given in Tables 3.6-3.7, and the calculated, observed and difference plots can be seen in Figures 3.8-3.9. This gave a good fit to the patterns but the intensities of the $0\bar{1}1$, 011, $10\bar{1}$ and 101 reflections were considerably under estimated by the nuclear model, the difference increasing with decreasing temperature, showing that these are magnetic Bragg contributions. No additional magnetic peaks were observed in any of the diffraction profiles indicating that the magnetic unit cell is the same as the structural supercell. For that reason, the magnetic structure was refined in the nuclear phase with both nuclear and magnetic scattering calculated for the nickel sites. Figure 3.10 shows the low angle region of the Rietveld fits at 5 and 300 K. The above reflections are derived from splitting the cubic perovskite (½ ½ ½) reflection and a magnetic model was therefore chosen where the moments form a G-type antiferromagnetic structure, in which all neighbouring magnetic moments of the Ni^{2+} ions are antiferromagnetically aligned (Figure 3.11). Hence, the spins on Ni1 and Ni4 are anti parallel to those on Ni2 and Ni3. The moments were also refined with the constraint that they are equal and opposite. This model provided a good fit to the magnetic intensities at all temperatures measured. The refined components of the magnetic moments are listed in Table 3.8. The G-type magnetic structure observed for $BiNiO_3$ is in agreement with $3d^8$ Ni^{2+} cations at the perovskites B-sites, as antiferromagnetic superexchange is expected for all of the Ni-O-Ni interaction according to the Goodenough-Kanamori rules[43, 44]. Atomic parameters from the Rietveld fits to the 100 and 200 K powder diffraction data can be found in Appendix A.

Table 3.6

Atomic parameters for $BiNiO_3$ from the Rietveld fit to 300 K (upper values) and 5 K (lower values) powder neutron diffraction data.

Atom	Site	*x*	*y*	*z*	$U_{iso} \times 100$ (Å^2)
Bi1	2i	0.0063(6)	0.0486(5)	0.2315(4)	0.51(8)
		0.0067(8)	0.0507(6)	0.2306(5)	0.07(10)
Bi2	2i	0.5105(6)	0.4426(6)	0.7242(4)	0.51(8)
		0.5097(8)	0.4430(7)	0.7230(5)	0.07(10)
Ni1	1d	0.5	0	0	0.96(6)
					0.56(8)
Ni2	1c	0	0.5	0	0.96(6)
					0.56(8)
Ni3	1f	0.5	0	0.5	0.96(6)
					0.56(8)
Ni4	1g	0	0.5	0.5	0.96(6)
					0.56(8)
O1	2i	-0.1410(9)	0.4708(8)	0.2521(6)	0.66(6)
		-0.1399(11)	0.0762(10)	0.2532(8)	0.51(8)
O2	2i	0.3949(9)	0.0780(7)	0.757496)	0.66(6)
		0.3952(11)	0.0762(9)	0.7573(7)	0.51(8)
O3	2i	0.8332(8)	0.1748(7)	-0.0327(6)	0.66(6)
		0.8353(10)	0.1745(9)	-0.0313(8)	0.51(8)
O4	2i	0.3166(8)	0.3359(7)	0.0836(6)	0.66(6)
		0.3165(11)	0.3331(9)	0.0829(8)	0.51(8)
O5	2i	0.2129(8)	0.7709(7)	0.4114(6)	0.66(6)
		0.2131(11)	0.7692(10)	0.4107(8)	0.51(8)
O6	2i	0.6737(8)	0.6868(7)	0.5465(6)	0.66(6)
		0.6734(11)	0.6859(9)	0.5459(8)	0.51(8)

Table 3.7

Structural parameters together with reliability factors for $BiNiO_3$, space group $P\bar{1}$, at 5, 100, 200 and 300 K.

Temperature (K)	5	100	200	300
a (Å)	5.38815(7)	5.38970(7)	5.39234(7)	5.39747(7)
b (Å)	5.64727(8)	5.64856(8)	5.65007(8)	5.65737(8)
c (Å)	7.69618(12)	7.69895(11)	7.70527(11)	7.71662(11)
α (°)	92.249(1)	92.237(1)	92.207(1)	92.179(1)
β (°)	89.781(1)	89.780(1)	89.780(1)	89.781(1)
γ (°)	91.718(1)	91.709(1)	91.698(1)	91.714
V ($Å^3$)	233.89(1)	234.10(1)	234.47(1)	235.20(1)
χ^2	1.19	1.92	1.87	1.67
R_{wp} (%)	6.54	4.66	4.56	4.26
R_p (%)	4.84	3.35	3.30	3.06
R_{F2} (%)	4.27	3.54	4.10	3.69

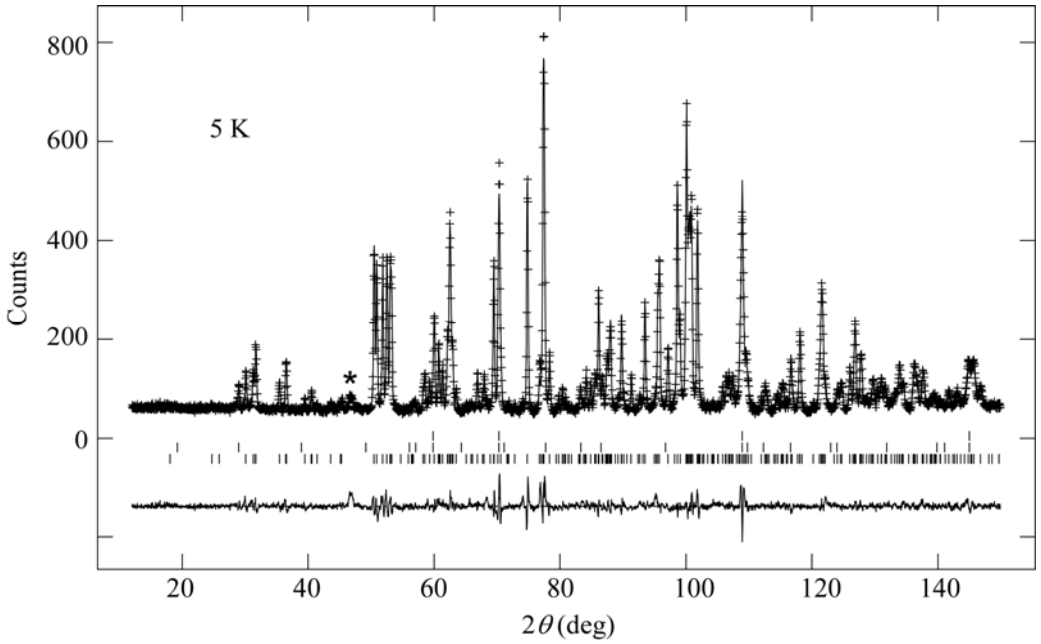

Figure 3.8 Observed, calculated and difference neutron diffraction profiles from the Rietveld refinement of $BiNiO_3$ at 5 K with the reflection markers representing $BiNiO_3$, NiO nuclear and NiO magnetic phase from bottom to top, and the contribution from an unknown impurity marked *.

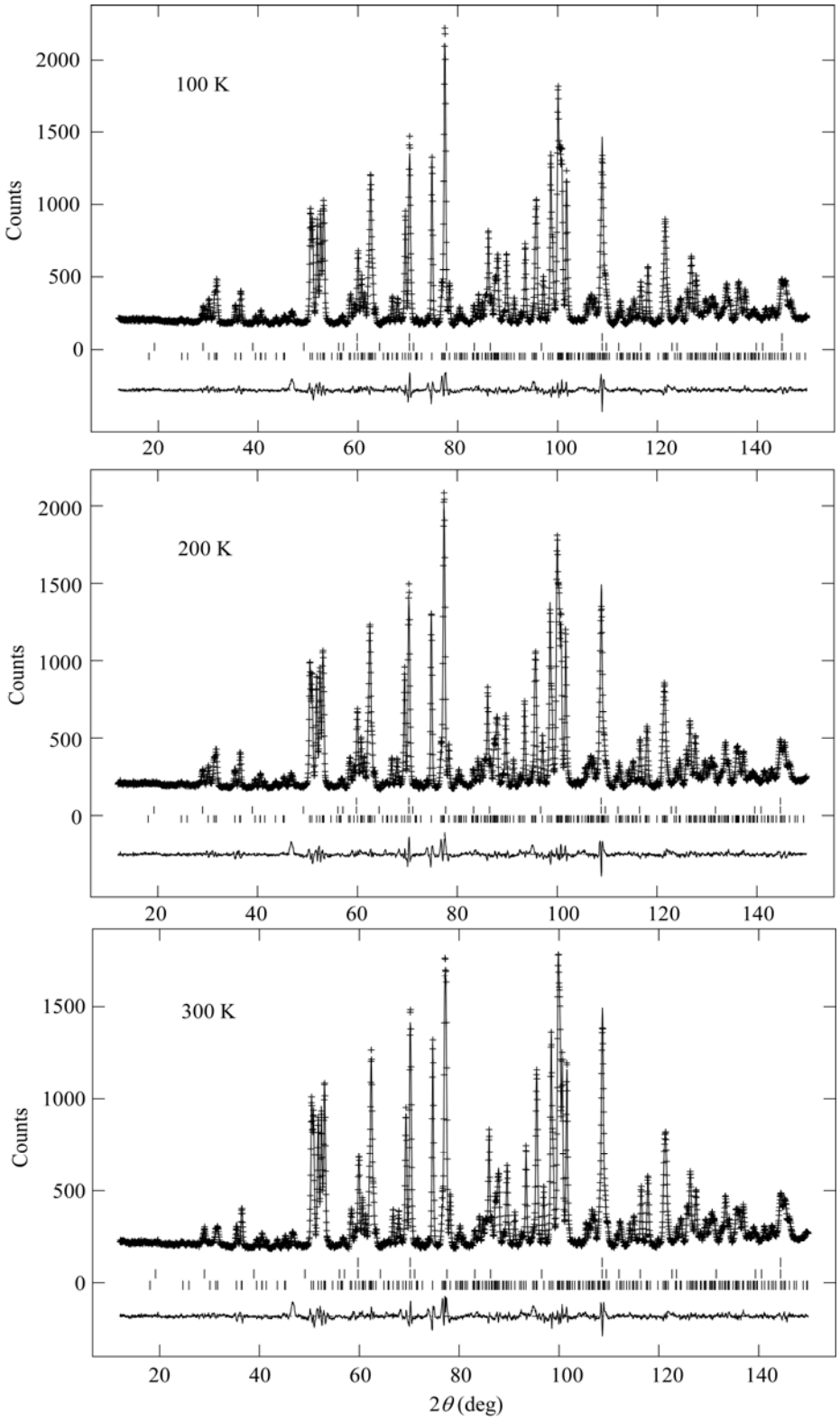

Figure 3.9 Observed, calculated and difference neutron diffraction profiles from the Rietveld refinement of $BiNiO_3$ at 100, 200 and 300 K with the reflection markers representing $BiNiO_3$, NiO nuclear and NiO magnetic phase from bottom to top.

Although the magnetic interactions are predominantly antiferromagnetic, the four Ni sites are unrelated by symmetry and so the orientation and magnitude of their magnetic moments will not be the same. Hence, the cancellation of the opposed Ni moments is not exact and a magnetic state occurs that can be described as ferrimagnetic. The existence of which is confirmed by the magnetic hysteresis curves previously reported for $BiNiO_3$[27]. Due to the small number of observed magnetic intensities it is not possible to refine the individual site moments against the present powder diffraction data. However, the good fit that was achieved with the above model demonstrates that the variations of the individual moments from the average are quite small and therefore, the suggested G-type antiferromagnetic model is a very good approximation of the ferrimagnetic order in $BiNiO_3$. The resultant magnetic moment of 1.74(3) μ_B at 5 K, which lies close to [001], is typical for $S = 1$ Ni^{2+}, with a small decrease from the expected value of 2 μ_B as a result of covalency. The variation of the overall magnetic moment with temperature is plotted in Figure 3.12 and confirms that the magnetic ordering transition temperature is close to 300 K[27].

The magnetic structure of $BiNiO_3$ is rather different to those reported for the insulating phases of the rare earth nickelate perovskites $RNiO_3$[19, 20]. In these compounds, charge disproportionation of the Ni leads to a $\sqrt{2}a_p \times \sqrt{2}a_p \times \sqrt{2}a_p$ superstructure of the perovskites a_p cell and a charge ordered arrangement of ideally $R_2Ni^{2+}Ni^{4+}O_6$. However, the observed charge separation is only 30-40 % of the ideal value. The spin order of theses phases is antiferromagnetic with a propagation vector of (½0½). This is typical for $A_2BB'O_6$ double perovskites with magnetic transition metals at B (and in some cases B') sites[45]. Complex spin order arrangements with (½0½) and (0½½) propagation vectors arise due to competition between 90° and 180° B-O-B'-O-B superexchange pathways as well as B-O-B' interactions when both cations are magnetic. The G-type spin order observed in $BiNiO_3$ is by contrast typical for ABO_3 perovskites with non-degenerate magnetic ions at B sites, for example $RCrO_3$ and $RFeO_3$. In these materials strong B-O-B antiferromagnetic superexchange dominates.

Examination of the structural results show that no phase transition takes place in the temperature range 5-300 K and the triclinic phase hardly changes throughout. The unit cell lengths *a, b* and *c* and the cell volume all decrease slightly with temperature and there is no discontinuity in the variation (Figure 3.13). The bond valence sums, BVS, listed in Table 3.8 verifies a very high degree (78 %) of Bi charge disproportionation[46]. Comparison of the values for the Bi and Ni atoms at 5 and 300 K shows that they are very similar, confirming that the charge distribution remains $Bi^{3+}_{0.5}Bi^{5+}_{0.5}Ni^{2+}O_3$ down to 5 K.

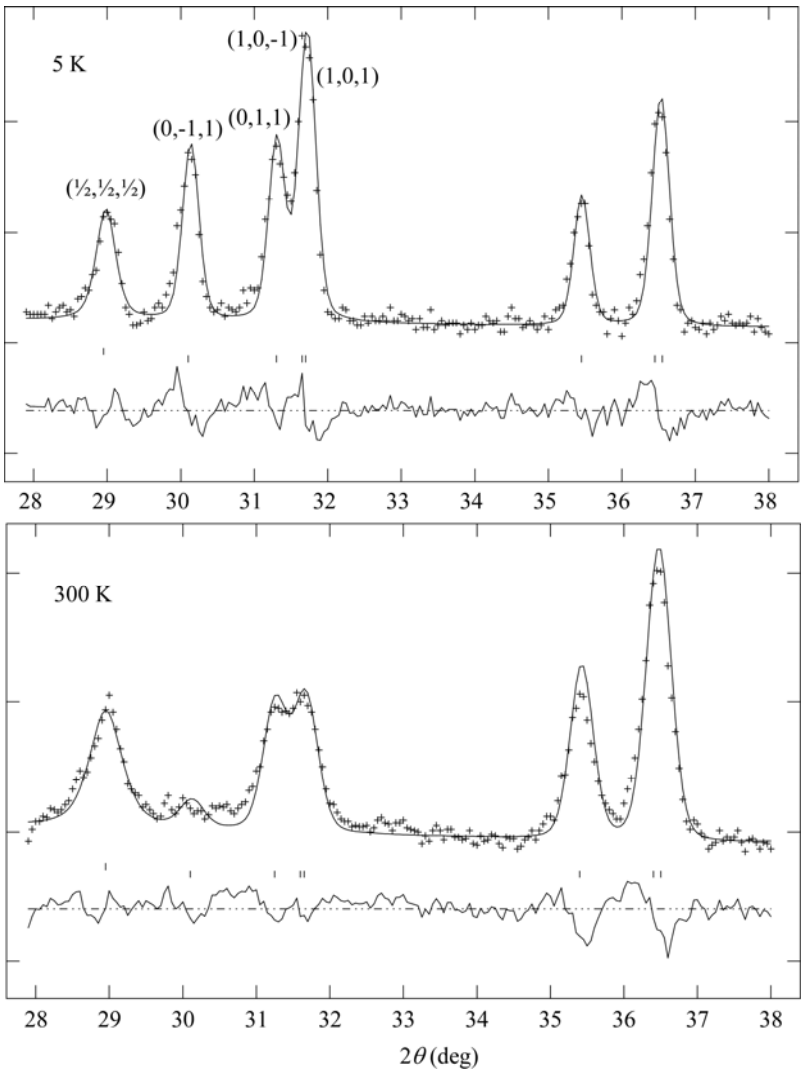

Figure 3.10 Rietveld fit of the low angle region of the crystal and magnetic structure at 5 and 300 K showing the NiO (½½½) magnetic superstructure peak and the $BiNiO_3$ $(0\bar{1}1)$, (011), $(10\bar{1})$ and (101) magnetic reflections.

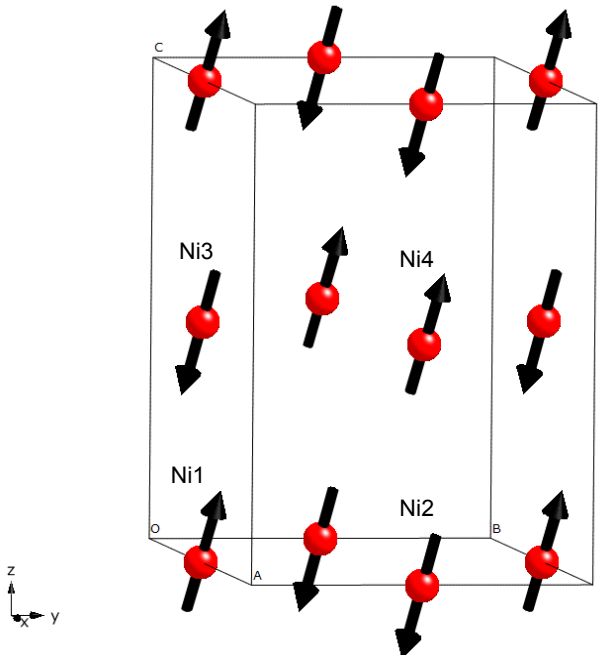

Figure 3.11 The G-type Arrangement of the magnetic spins in $BiNiO_3$.

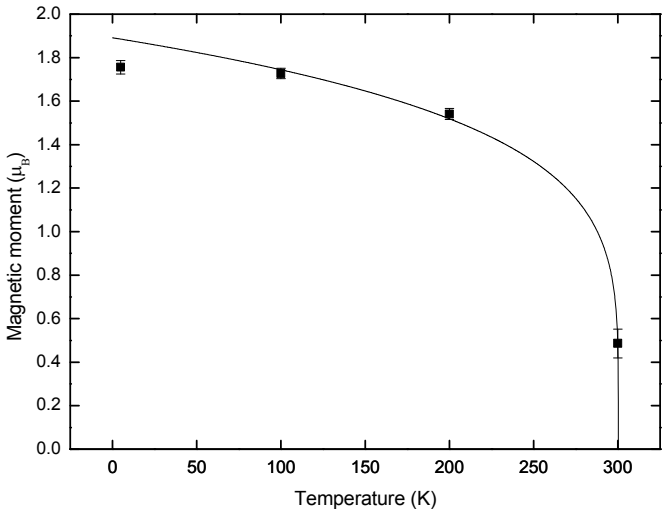

Figure 3.12 Variation of magnetic moment with temperature. A critical law curve is shown as a guide to the eye. The points have been fitted with the expression $M = M_0\left(1-\frac{T}{T_C}\right)^{\beta}$ where M_0 and T_C were set to vary and β was fixed at a value of 0.2.

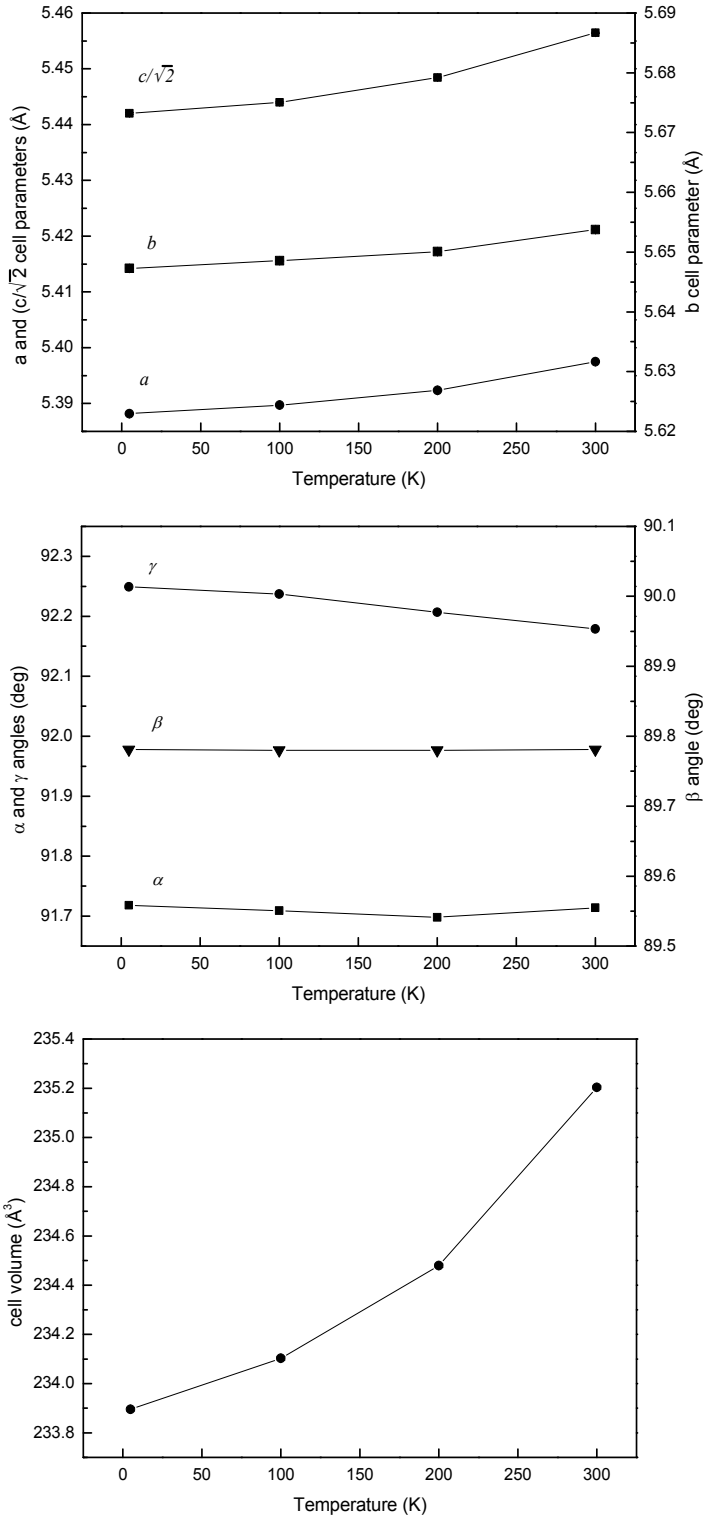

Figure 3.13 Temperature dependence of the $BiNiO_3$ cell parameters. The c-axis length is divided by √2 for compatability.

Table 3.8

The refined magnetic moment components for $BiNiO_3$, and Bond Valence Sums (BVS) for Bi and Ni calculated from the Bi-O and Ni-O bond lengths, at 5, 100, 200 and 300 K.

Temperature		5 K	100 K	200 K	300 K
Magnetic moments	μ_x (μ_B)	0.68(12)	0.95(8)	0.90(8)	0.32(20)
	μ_y (μ_B)	0.40(7)	0.25(6)	0.22(7)	0.08(22)
	μ_z (μ_B)	1.57(6)	1.42(6)	1.23(7)	0.32(21)
	μ_{Tot} (μ_B)	1.76(3)	1.73(2)	1.54(3)	0.49(7)
BVSs	Bi1	3.25	3.23	3.22	3.20
	Bi2	4.78	4.79	4.74	4.75
	Ni1	1.83	1.83	1.83	1.81
	Ni2	1.96	1.96	1.97	1.95
	Ni3	1.84	1.86	1.85	1.83
	Ni4	2.06	2.02	2.03	1.99

3.4 Conclusions

In conclusion, from the BVS calculations it was confirmed that the charge distribution in $BiNiO_3$ is $Bi^{3+}_{0.5}Bi^{5+}_{0.5}Ni^{2+}O_3$ at ambient pressure and $Bi^{3+}Ni^{3+}O_3$ in the high pressure phase[46]. This shows that the pressure–induced insulator to metal transition occurs via an exceptional simultaneous melting of the Bi-charge disproportionation and a Ni→Bi charge transfer[47]. The various electronic instabilities in $BiNiO_3$ may offer new possibilities for tuning the electronic phenomena in oxides and creating devices based on switching between the different phases as have been demonstrated for perovskites manganites.

The analysis of the diffraction data shows that the crystal structure is triclinic, spacegroup $P\bar{1}$, for all temperatures measured and BVS calculations indicate that the charge distribution remains $Bi^{3+}_{0.5}Bi^{5+}_{0.5}Ni^{2+}O_3$ down to 5 K. This confirms that phase IV does not occur in the temperature range 5-300 K at ambient pressure. The magnetic order was found to be G-type antiferromagnetic with the magnetic unit cell being equal to that of the nuclear unit cell[47]. From the Rietveld refinement of the

5 K data a magnetic moment of 1.74(3) μ_B was obtained, with the moment decreasing with increased temperature below the Néel temperature. Fitting of a critical law curve to the data confirms that the transition temperature is close to 300 K as indicated by previous magnetic susceptibility measurements[27].

These results demonstrate that $BiNiO_3$ is a unique perovskite in having electronically variable A- and B-site cations, with an active intermetallic charge-transfer degree of freedom as well as charge disproportionation instabilities at both the A and B sites. Four distinct electronic ground states should be observable in $BiNiO_3$ as shown in Figure 3.14. Phases I and III are observed at low and high pressures at ambient temperature as illustrated in this work. Phase II is also expected to take place in pure $BiNiO_3$ at an elevated temperature but this has not yet been observed as it decomposes at a temperature lower than the transition temperature at ambient pressure. However, stabilised forms of phase II can be achieved by Pb-doping which disrupts the long range Bi^{3+}/Bi^{5+} charge order resulting in $Bi^{4+}_{0.8}Pb^{4+}_{0.2}Ni^{2+}O_3$[38]. It has also been confirmed that the Bi^{4+} state is found in the La-doped compound, $Bi^{4+}_{1-x}La^{3+}_{x}Ni^{(2+x)+}O_3$[35]. Ground state IV, $Bi^{3+}Ni^{2+}_{0.5}Ni^{4+}_{0.5}O_3$, has not yet been observed and the present study shows that it does not occur at ambient pressures down to 5 K[46]. However, disproportionation of Ni^{3+} is seen in $RNiO_3$ for R^{3+} smaller than La^{3+} or Bi^{3+} and so it is expected that this ground state may be formed in $BiNiO_3$ at high pressures and low temperatures or in substituted $Bi^{3+}_{0.5}R^{3+}_{0.5}Ni2^{+}_{0.5}Ni^{4+}_{0.5}O_3$ for small R^{3+}.

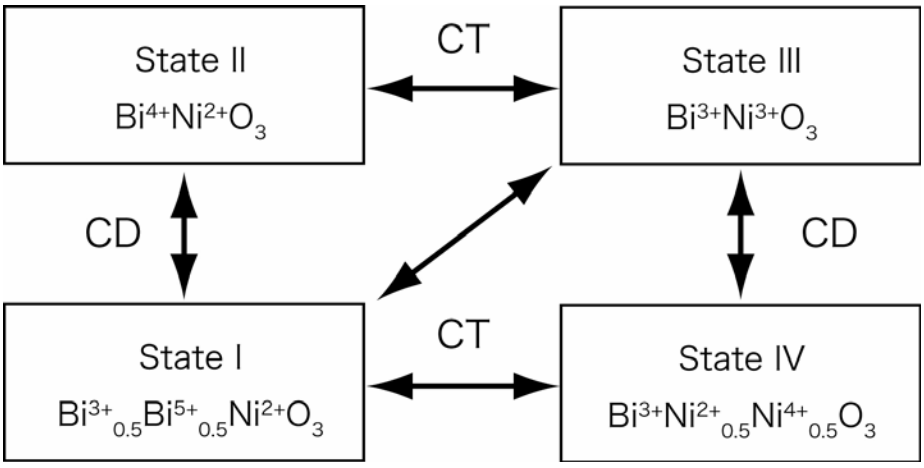

Figure 3.14 Electronic ground states for $BiNiO_3$ showing intermetallic charge transfer (CT) and charge disproportionation (CD) transitions. The pressure-induced insulator to metal transition between states I and III is also indicated.

3.5 References

1. J.G. Bednorz and K.A. Muller, *Zeits. F. Phys. B*, **64**, 189-193 (1986).
2. K. Chahara, T. Ohno, M. Kasai and Y. Kozono, *Appl. Phys. Lett.*, **63**, 1990-1992 (1993).
3. P. Schiffer, A.P. Ramirez, W. Bao and S.W. Cheong, *Phys. Rev. Lett.*, **75**, 3336-3339 (1995).
4. K. Iijima, R. Takayama, Y. Tomita and I. Ueda, *J. Appl. Phys.*, **60**, 2914-2919 (1986).
5. J. Wang, J.B. Neaton, H. Zheng, V. Nagarajan, S.B. Ogale, B. Liu, D. Viehland, V. Vaithyanathan, D.G. Schlom, U.V. Waghmare, N.A. Spaldin, K.M. Rabe, M. Wuttig and R. Ramesh, *Science*, **299**, 1719-1722 (2003).
6. V.M. Goldschmidt, *Skr. Nor. Videnk.-Akad, KI. 1: Mat-Naturvidensk.*, **8**, (1926).
7. R.J. Cava, B. Batlogg, J.J. Krajewski, R. Farrow, L.W. Rupp, A.E. White, K. Short, W.F. Peck and T. Kometani, *Nature*, **332**, 814-816 (1988).
8. A.W. Sleight, J.L. Gillson and P.E. Bierstedt, *Solid State Comm.*, **17**, 27-28 (1975).
9. P.G. Radaelli, D.E. Cox, M. Marezio and S.W. Cheong, *Phys. Rev. B*, **55**, 3015 (1997).

10. M. Takano, N. Nakanishi, Y. Takeda, S. Naka and T. Takada, *Mater. Res. Bull.*, **12**, 923-928 (1977).
11. P.M. Woodward, D.E. Cox, E. Moshopoulou, A.W. Sleight and S. Morimoto, *Phys. Rev. B*, **62**, 844-855 (2000).
12. J.L. Garcia-Munoz, M. Amboage, M. Hanfland, J.A. Alonso, M.J. Martinez-Lope and R. Mortimer, *Phys. Rev. B*, **69**, 094106-6 (2004).
13. J.A. Alonso, M.J. Martínez-Lope, M.T. Casais, J.L. García-Muñoz, M.T. Fernández-Díaz and M.A.G. Aranda, *Phys. Rev. B*, **64**, 094102 (2001).
14. T. Saito, M. Azuma, E. Nishibori, M. Takata, M. Sakata, N. Nakayama, T. Arima, T. Kimura, C. Urano and M. Takano, *Physica B*, **329-333**, 866-867 (2003).
15. J.A. Alonso, J.L. Garcia-Munoz, M.T. Fernandez-Diaz, M.A.G. Aranda, M.J. Martinez-Lope and M.T. Casais, *Phys. Rev. Lett.*, **82**, 3871-3874 (1999).
16. J.L. García-Muñoz, J. Rodríguez-Carvajal, P. Lacorre and J.B. Torrance, *Phys. Rev. B*, **46**, 4414 (1992).
17. M. Medarde and L. a, *J. Phys.: Cond. Matt.*, **9**, 1679-1707 (1997).
18. J.S. Zhou, J.B. Goodenough, B. Dabrowski, P.W. Klamut and Z. Bukowski, *Phys. Rev. Lett.*, **84**, 526 (2000).
19. J.L. García-Muñoz, J. Rodríguez-Carvajal and P. Lacorre, *Phys. Rev. B*, **50**, 978 (1994).
20. J. Rodríguez-Carvajal, S. Rosenkranz, M. Medarde, P. Lacorre, M.T. Fernandez-Díaz, F. Fauth and V. Trounov, *Phys. Rev. B*, **57**, 456 (1998).
21. G. Demazeau, A. Marbeuf, M. Pouchard and P. Hagenmuller, *J. Solid State Chem.*, **3**, 582 (1971).
22. J.K. Vassiliou, M. Hornbostel, R. Ziebarth and F.J. Disalvo, *J. Solid State Chem.*, **81**, 208 (1989).
23. J.A. Alonso, M.J. Martinez-Lope, M.T. Casais, M.A.G. Aranda and M.T. Fernandez-Diaz, *J. Am. Chem. Soc.*, **121**, 4754-4762 (1999).
24. Y.Y. Tomashpolskii, E.V. Subova, K.P. Burdina and Y.N. Venevtsev, *Izv. Akad. Nauk SSSR, Ser. Neorg. Mater.*, **3**, 2123 (1967).
25. Y.Y. Tomashpolskii and Y.N. Venevtsev, *Izv. Akad. Nauk SSSR, Ser. Neorg. Mater.*, **5**, 1279 (1969).

26. Y.Y. Tomashpolskii, Y.N. Venevtsev, K.P. Burdina and Y.N. Venevtsev, *Kristallografiya*, **13**, 987 (1968).
27. S. Ishiwata, M. Azuma, M. Takano, E. Nishibori, M. Takata, M. Sakata and K. Kato, *J. Mater. Chem.*, **12**, 3733-3737 (2002).
28. N.E. Brese and M. Okeeffe, *Acta Cryst. B*, **47**, 192-197 (1991).
29. I.D. Brown and D. Altermatt, *Acta Cryst. B*, **41**, 244-247 (1985).
30. H. Wadati, M. Takizawa, T.T. Tran, K. Tanaka, T. Mizokawa, A. Fujimori, A. Chikamatsu, H. Kumigashira, M. Oshima, S. Ishiwata, M. Azuma and M. Takano, *Phys. Rev. B*, **72**, 155103-5 (2005).
31. S. Niitaka, M. Azuma, M. Takano, E. Nishibori, M. Takata and M. Sakata, *Solid State Ionics*, **172**, 557-559 (2004).
32. A.A. Belik, S. Iikubo, K. Kodama, N. Igawa, S. Shamoto, S. Niitaka, M. Azuma, Y. Shimakawa, M. Takano, F. Izumi and E. Takayama-Muromachi, *Chem. Mater.*, **18**, 798-803 (2006).
33. T. Kimura, S. Kawamoto, I. Yamada, M. Azuma, M. Takano and Y. Tokura, *Phys. Rev. B*, **67**, 180401 (2003).
34. M. Azuma, K. Takata, T. Saito, S. Ishiwata, Y. Shimakawa and M. Takano, *J. Am. Chem. Soc.*, **127**, 8889-8892 (2005).
35. S. Ishiwata, M. Azuma, M. Hanawa, Y. Moritomo, Y. Ohishi, K. Kato, M. Takata, E. Nishibori, M. Sakata, I. Terasaki and M. Takano, *Phys. Rev. B*, **72**, 045104-7 (2005).
36. A. Shukla, J.-P. Rueff, J. Badro, G. Vanko, A. Mattila, F.M.F. de Groot and F. Sette, *Phys. Rev. B*, **67**, 081101 (2003).
37. S. Ishiwata, M. Azuma and M. Takano, *Solid State Ionics*, **172**, 569-571 (2004).
38. S. Ishiwata, M. Azuma and M. Takano, *Chem. Mater.*, **19**, 1964-1967 (2007).
39. J.M. Besson, R.J. Nelmes, G. Hamel, J.S. Loveday, G. Weill and S. Hull, *Physica B*, **180-181**, 907-910 (1992).
40. H.M. Rietveld, *Acta Cryst.*, **22**, 151 (1967).
41. A.C. Larson and R.B.V. Dreele, *General Structural Analysis System (GSAS)*; Los Alamos National Laboratory: Los Alamos, 2000.

42. D. Rodic, V. Spasojevic, V. Kusigerski, R. Tellgren and H. Rundlof, *Physica Stat. Sol. B*, **218**, 527 (2000).
43. J.B. Goodenough, *Magnetism and the Chemical Bond*; Interscience: New York, 1963.
44. J. Kanamori, *J. Phys. Chem. Solids*, **10**, 87-98 (1959).
45. J.W.G. Bos and J.P. Attfield, *Phys. Rev. B*, **70**, (2004).
46. S.J.E. Carlsson, M. Azuma, Y. Shimakawa, M. Takano, A. Hewat and J.P. Attfield, *J. Solid State Chem.*, **181**, 611 (2008).
47. M. Azuma, S. Carlsson, J. Rodgers, M.G. Tucker, M. Tsujimoto, S. Ishiwata, S. Isoda, Y. Shimakawa, M. Takano and J.P. Attfield, *J. Am. Chem. Soc.*, **129**, 14433-14436 (2007).

Chapter 4

Structural stability of $(EDT\text{-}TTF\text{-}CONH_2)_6[Re_6Se_8(CN)_6]$ under high pressure

4.1 Introduction

In the early 1970's the search for organic conductors led to the discovery of metal-like electrical conduction in well-ordered molecular crystals as well as a variety of other electronic properties from magnetic insulators to superconductors[1]. These properties are associated with the low dimensionality (one or two dimensions) of the electron gas in the charge-transfer compounds in which they were observed.

Charge-transfer materials contain an anionic and a cationic component, originating from a charge transfer between a donor and acceptor species that could be two organic molecules or an organic molecule with an inorganic ion. For the last three decades, the most investigated organic conductors are molecular compounds based on the tetrathiafulvalene (TTF) molecule[2] with the classical example being TTF-TCNQ (TCNQ = tetracyano-*p*-quinodimethane). Discovered in 1973[3], it is a typical charge-transfer material where the structure is made up of separate stacks of donor TTF and acceptor TCNQ molecules with electronic interaction occurring only in one direction (within the stacks) through their delocalised π system. A metal-insulator transition associated with a lattice distortion is observed on cooling.

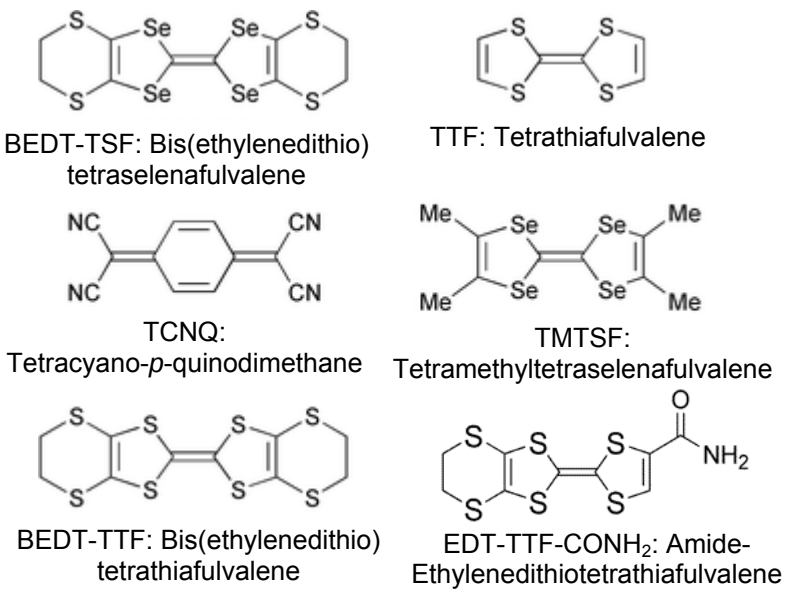

Figure 4.1 Illustration and abbreviations of some precursor molecules to conducting and superconducting molecule-based compounds.

Another class of organic conductors are the radical cation salts such as $TMTSF_2X$ where X is an organic anion and TMTSF is the organic molecule tetramethyltetraselenafulvalene. Depending on temperature and applied pressure, an insulating state can be replaced by a metallic or even a superconducting state as seen in the first organic superconductor $(TMTSF)_2PF_6$, reported in 1980[4]. In this group of materials, also referred to as the Beachgaard salts, the molecules form a zigzag pattern along the stacking axis and one positive charge or hole is shared between two molecules. Stronger interactions between the stacks caused by short selenium-selenium interatomic distances mean that the structure can be considered as almost two dimensional. Also important are the salts of the electron donor bis(ethylenedithio)tetrathiofulvalene (BEDT-TTF), which tends to form polymorphic phases with significant differences in structure and properties[5]. Figure 4.1 shows the structures and full names of the organic molecules discussed in the text above. Introducing amides in TTF-based materials produces a templating effect of the inorganic counter ion and salts with different stoichiometry can be obtained from

isosteric ions. For example, crystallisation of EDT-TTF-$CONH_2$ with ReO_4^- yields a 2:1 metallic salt whereas AsF_6^- gives the 6:1 salt.

Recently, a new conducting, molecular mixed-valence π-conjugated radical cation salt, (EDT-TTF-$CONH_2$)$_6$[$Re_6Se_8(CN)_6$] has been synthesised[6]. It is unique amongst the TTF-based materials because it exhibits the Kagome topology. Figure 4.2(a) depicts the Kagome lattice, a planar hexagonal net composed of interlaced triangles, which is of particular interest due to its large degree of frustration and lack of a well defined ground state structure. When unpaired spins are situated at the corners or sides of the lattice triangles, antiferromagnetic couplings can not be completely satisfied and with the freedom of twist of the spin planes, this gives rise to a number of degenerate ground states, especially for S = ½ spins[7, 8]. Two of these states are known to exhibit long range order, Figure 4.2(b) and (c). Whilst Kagome layers can be found in inorganic compounds such as the minerals Jarosite and Volborthite[8], there are very few molecular systems with this topology. One example is the molecular salt (m-MPYNN)X (m-N-methylpyridinium α-nitronyl nitroxide, X = I^-, BF_4^-, ClO_4^- etc.), where unpaired S = ½ spins are ferromagnetically coupled within m-MPYNN molecular dimers (S = 1) that in turn order antiferromagnetically[9, 10]. However, (EDT-TTF-$CONH_2$)$_6$[$Re_6Se_8(CN)_6$] is the only known TTF-based material to exhibit a Kagome lattice symmetry.

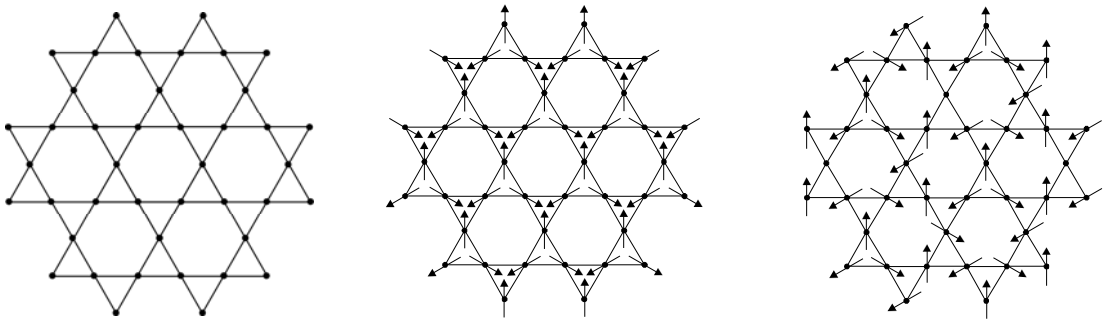

(a) **(b)** **(c)**

Figure 4.2 A planar representation of the Kagome lattice (a) with examples of two different degenerate ground states for the spin structure (b) and (c).

The crystal structure of (EDT-TTF-CONH$_2$)$_6$[Re$_6$Se$_8$(CN)$_6$] has previously been determined by single-crystal X-ray diffraction as belonging to the rhombohedral system, spacegroup $R\bar{3}$, with one EDT-TTF-CONH$_2$ in general position and the octahedral cluster anion occupying a $\bar{3}$ symmetry site[6]. Each cluster anion is connected to six EDT-TTF-CONH$_2$ molecules by strong hydrogen bonds formed between the cyanide groups of the anion and one of the amino group hydrogen atoms from the organic molecules as shown in Figure 4.3(a). The [EDT-TTF-CONH$_2$]$_6${Re$_6$Se$_8$(CN)$_6$] units are interlocked with six others forming a two-dimensional pattern where any cluster core is surrounded by six centrosymmetrical dimers. Connecting the centres of the [EDT-TTF-CONH$_2$]$_2$ dimers yields a Kagome type lattice in the (111) plane, drawn in Figure 4.3(b), where the dimers are located at the corner of the triangles and cluster anions fill the hexagonal voids.

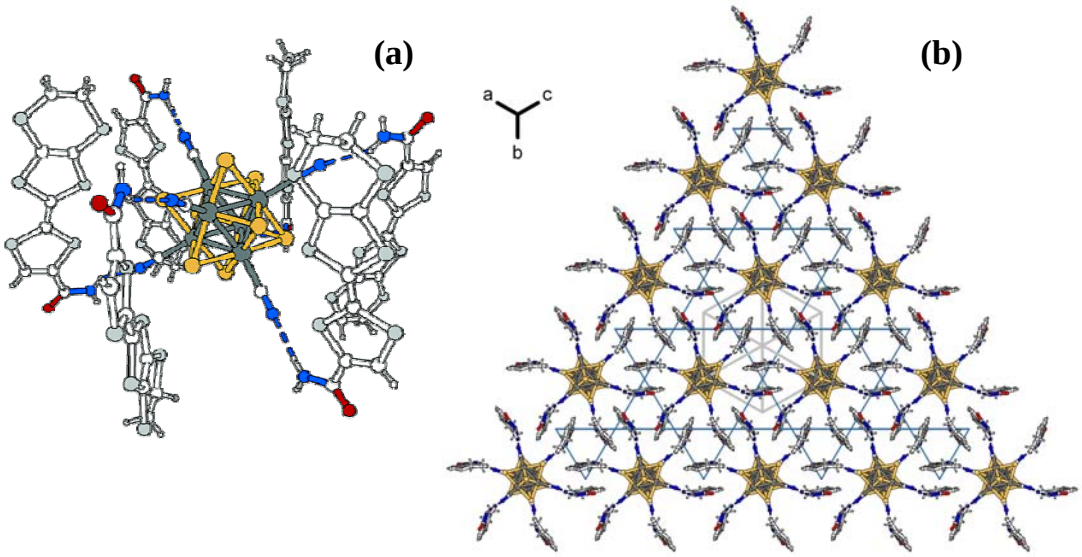

Figure 4.3 A projection of the [EDT-TTF-CONH$_2$]$_6$[Re$_6$Se$_8$(CN)$_6$] unit (a), assembled via N-H···N≡C hydrogen bonds, which connects with six of its congeners to form a Kagome pattern of dimers (b). From [6].

The only connection between the (111) blocks are self-complementary hydrogen bonds between the remaining amino group hydrogen and the carbonyl

oxygen of another molecule leading to the formation of what looks like organic tubes along the $\bar{3}$ axis. Hence, there is no direct overlap between the molecular cation π systems of different (111) layers and the electronic structure is based only on the HOMO interactions between molecules within any two-dimensional Kagome lattice[6].

There are only two different interactions present, one intradimer and one interdimer with the former calculated as being 4 times stronger (+ 413 compared to -115 meV at room temperature) as a result of a favourable overlap mode that shortens the contacts between the sulphur atoms[6]. Infrared spectroscopy measurements and single-crystal electron spin resonance measurements indicate that the charge balance between the two components is [(EDT-TTF-$CONH_2$)$_6^{4(+)}$][$Re_6Se_8(CN)_6^{4-}$] at room temperature i.e. the clusters are fully reduced (and diamagnetic) and four holes are shared between the three dimers in each unit cell, with small amounts of [$Re_6Se_8(CN)_6$]$^{-3}$[6]. This is in accordance with the conductivity measurements which have shown that (EDT-TTF-$CONH_2$)$_6$[$Re_6Se_8(CN)_6$] is metallic at room temperature[6]. However, a metal to insulator transitions occurs between 150-200 K, Figure 4.4(a), accompanied by a change in the magnetic behaviour, Figure 4.4(b). In accordance, single-crystal X-ray diffraction studies has revealed that a phase transition occurs and at 100 K the structure was found to be triclinic, spacegroup $P\bar{1}$. This leads to a change in the conformation and orientation of one of the dimers and it becomes fully oxidised, (EDT-TTF-$CONH_2$)$^{2+}$, whilst the other two mixed-valence dimers, remain in effect unchanged across the phase transition (Figure 4.5(c)). Because the three-fold symmetry has been lost, three different intradimer and interdimer interactions are now present, with the former calculated as being +413, +587 and +414 meV, confirming that the interactions within one of the dimers have clearly become stronger. This increase is thought to originate from a movement of the molecules making the dimer half-eclipsed allowing more favourable sulphur-sulphur orbital interactions as shown in Figure 4.5(d). In effect, a charge ordering has occurred which brakes the two dimensional symmetry within the Kagome layers leaving only one single direction of one dimensional uniform chains of spins ½, illustrated in

Figure 4.5(a) and (b). However, the transition is fully reversible as sharp Bragg peaks can be recovered upon bringing the crystal back to room temperature.

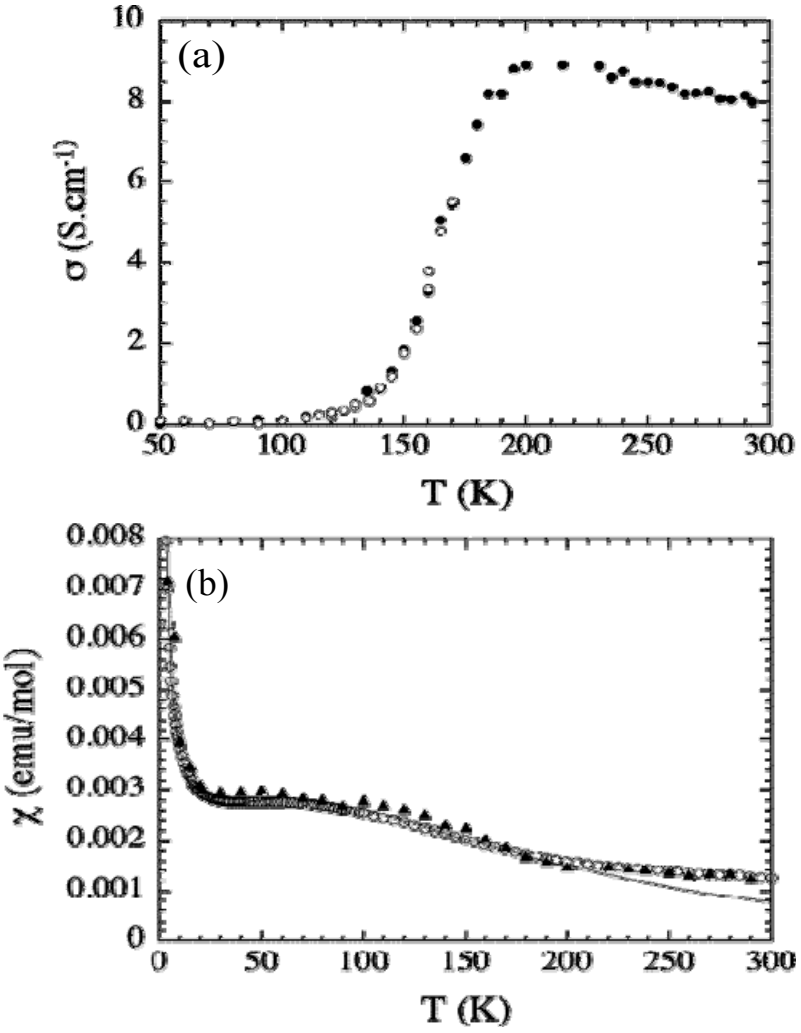

Figure 4.4 Temperature dependence of the electrical conductivity (top) and spin susceptibility (bottom) of (EDT-TTF-CONH$_2$)$_6$[Re$_6$Se$_8$(CN)$_6$] from [6]. In the top diagram, open and full circles correspond to two different crystals. In the bottom diagram the open dots are data from SQUID measurements and the open triangles Electron Spin Resonance (ESR) data.

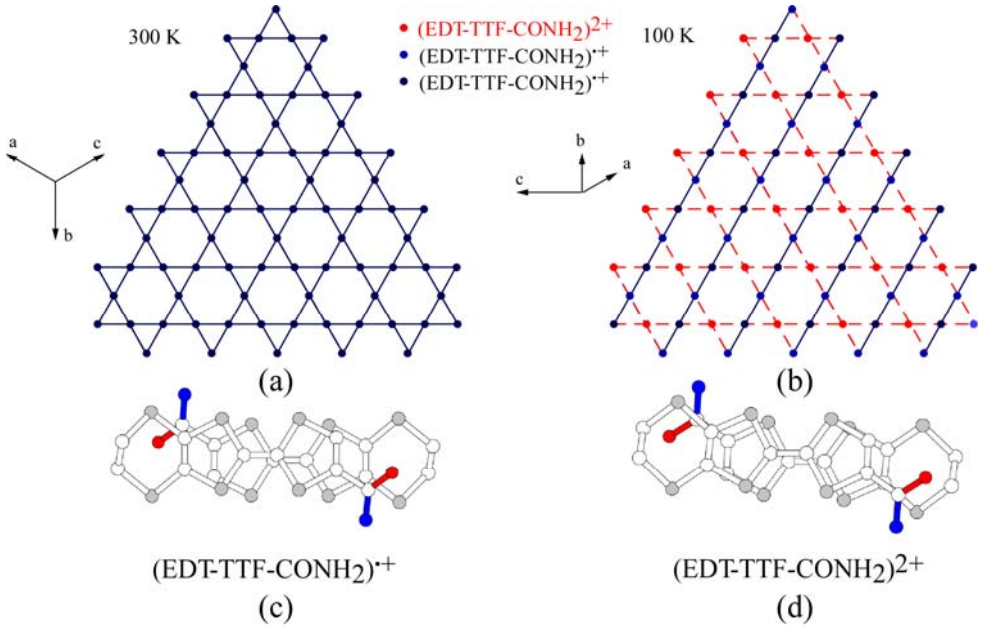

Figure 4.5 Illustration of the Kagome net in the rhombohedral room-temperature structure (a) and the broken symmetry in the triclinic 100 K structure (b) that occurs due to the localisation of one extra hole on one of the 3 dimers. The transition leaves two dimers essentially unchanged (c) but the third becomes half-eclipsed (d) resulting in charge ordering along the red broken lines (b).

The low temperature triclinic structure is associated with a localised, electrically insulating ground state, where only the 24-electron, diamagnetic cluster tetraanions, $[Re_6Se_8(CN)_6]^{4-}$, occupy the cluster sites. Its magnetic susceptibility is explained by a model of uniform chains of localised $S = ½$ spins in accordance with the averaged 100 K crystal structure and band structure calculations. The stability of this special Kagome topology can be understood by examining the relationship between the temperature dependant degree of charge transferred between the organic and inorganic component, i.e. the $[Re_6Se_8(CN)_6]^{3-}/[Re_6Se_8(CN)_6]^{4-}$ ratio at any temperature, and the electronic ground state and net molecular motion reached in the material. Similar cases of subtle symmetry breaking disorder are observed in mixed-valent inorganic oxides such as magnetite (Fe_3O_4) but are very unusual in molecular systems. The intention of this work is to study the structure under high pressure and gain more insight into the properties of this material. Pressure provides an additional method to transform the two structures and could change the charge localised

structure or favour another ground state by changing the balance of intermolecular interactions at higher densities.

4.2 Experimental

4.2.1 Synthesis

Crystals of (EDT-TTF-CONH$_2$)$_6$ (Re$_6$Se$_8$(CN)$_6$) were prepared by Dr. P. Batail and co-workers at the University of Angers using an electrocrystallisation method[11]. Firstly, 5 mg of EDT-TTF-CONH$_2$ was oxidised in the presence of 25 mg of (PPh$_4$)$_4$(Re$_6$Se$_8$(CN)$_6$) in a 1/1 mixture of 12 ml freshly distilled acetonitrile and tetrahydrofuran. The crystallisation experiments were then carried out in two-compartment cells with platinum wires (l = 2cm, Ø = 1mm), Figure 4.6, at a constant current of 0.5 mA at 25˚C, yielding octahedral black crystals. These crystals were then gently ground into a fine powder for the synchrotron X-ray powder diffraction experiments.

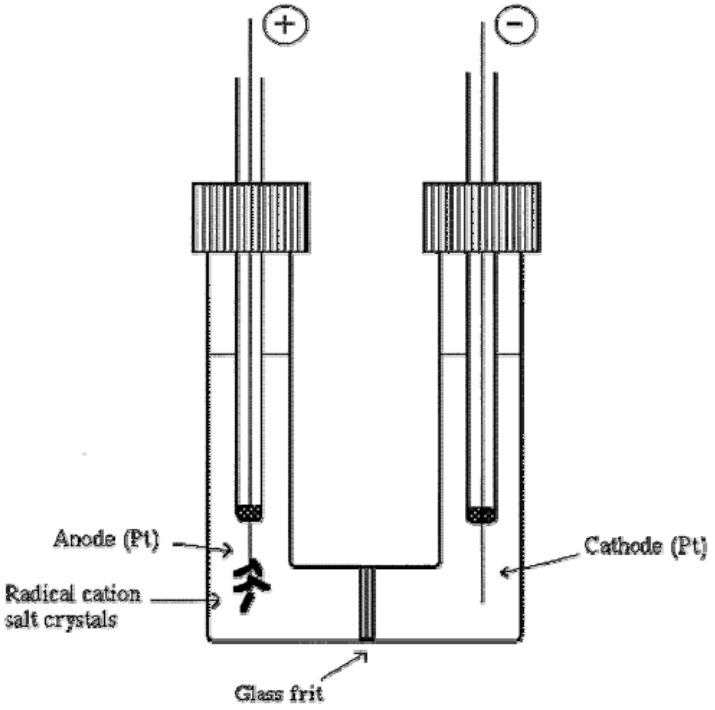

Figure 4.6 Drawing of a typical two-compartment electrocrystallisation cell from [11].

4.2.2 Synchrotron X-ray Diffraction Measurements

4.2.2.1 Powder study

High pressure synchrotron X-ray powderdiffraction patterns were collected at room temperature on station 9.5 of the Daresbury Synchrotron Radiation Source (Warrington, UK), with λ = 0.44374 Å, using a diamond-anvil cell set-up. Data were collected on an image plate and each scan was run for 10 minutes which was enough time to give clear data. Silicon oil was used as pressure medium. The pressure was increased in steps of 0.3 to 0.5 GPa and measured both before and after each scan. An average was then taken of the before and after values and this number was used for the plots. Peak broadening and freezing of the pressure medium, which leads to uneven pressure inside the cell, meant that the highest pressure reached was 4.82 GPa.

4.2.2.2 Single crystal study

Synchrotron X-ray single-crystal diffraction experiments were performed at Beamline 9.8 of the SRS using a wavelength of 0.6751 Å, a 200 μm collimator and a sample to detector distance of 70 mm. The sample was loaded in a Merrill-Bassett diamond-anvil cell[12] equipped with 600 μm culet diamonds and a tungsten gasket. A small chip of ruby was placed beside the sample for subsequent pressure measurement utilizing the ruby fluorescence technique[13]. The gasket hole was filled with mineral oil to act as a pressure-transmitting medium before the cell was finally assembled. Diffraction data were collected on a BRUKER APEXCCD-type detector at 295 K in a manner described by Dawson *et al*[14]. Integrations were performed using the program SAINT[15] and absorption corrections were made with the programs SADABS[16] and SHADE[17]. Figure 4.7 shows a copy of a data frame taken at 0.4 GPa illustrating the contamination by the intense diamond reflection and the beryllium powder rings. This reduces the number of useful reflections as only spots with intensities above those of the beryllium rings are used when harvesting reflections. The completeness of the data sets are also limited by the restricted volume of reciprocal space that can be accessed on account of the 40°

opening angle of the Merrill-Bassett diamond anvil cell[12]. Data were collected at pressures of 0, 0.4, 0.8, 1.2 and 1.8 GPa, and refinements were carried out against $|F^2|$ on all data using the *CRYSTALS* code[18] .

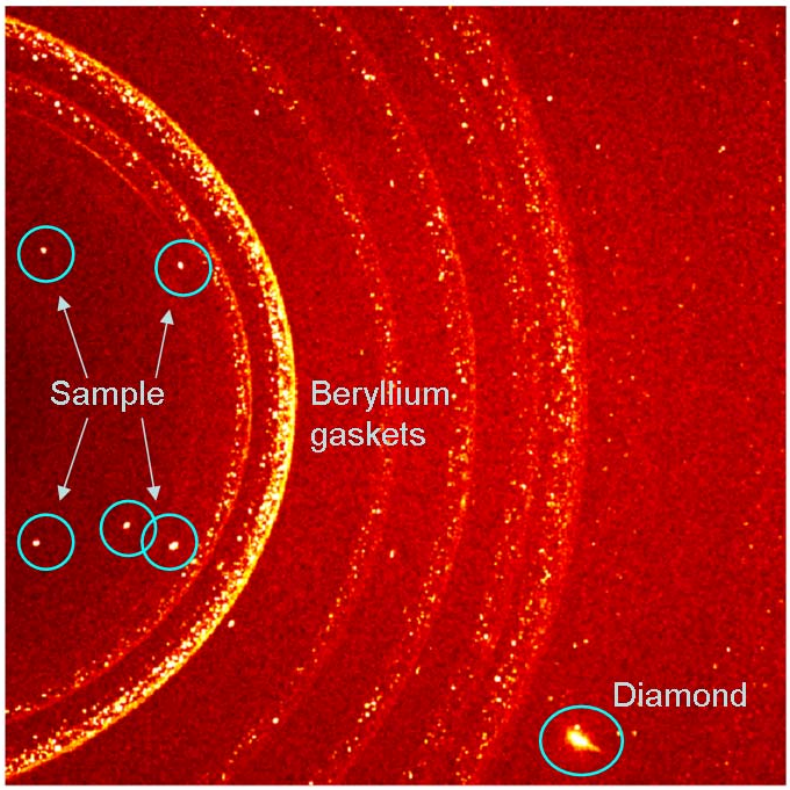

Figure 4.7 Data frame taken of the sample at 0.4 GPa showing some sample reflections and the contamination by the intense diamond reflection and the beryllium powder rings.

4.3 Results

4.3.1 Powder diffraction study

The synchrotron X-ray powder data were indexed in the rhombohedral space group $R\bar{3}$, with starting values of a = 15.0192 Å and α = 61.47˚ according to results obtained by Baudron *et al*[6], and analysed with the GSAS software using a Le Bail profile fitting[19]. This method does not allow for a total refinement of such a complex structure but it makes it possible to follow the variation of the lattice parameters with pressure. The lattice parameters and profile coefficients *GU, GV, GW* and *LY* were all refined for the ambient pressure data until a good fit was achieved. The values obtained for Gaussian coefficients *GU, GV* and *GW* were then fixed for the high pressure data refinements and only the lattice parameters and Lorentzian coefficient LY were varied. Typical refinement plots are shown in Figures 4.8 and 4.9. At ambient pressure, the lattice parameters a and α had a value of 14.98(6) Å and 61.403(8)˚ respectively which is slightly lower than those previously reported[6]. The cell parameters and the unit cell volume, V, gradually decreased as pressure was applied (Figure 4.10) corresponding to the intermolecular distances being reduced. Near the top of the pressure range, there appears to be an increase in the cell parameters, with a minimum of a and V appearing around 4.4 GPa. The angle, α has a minimum of 60.36 degrees at the lower pressure of 3.5 GPa. This, as expected, corresponds to the maximum value of profile coefficient *LY*, which slowly increases with pressure up until this point (Figure 4.10). The increase in the lattice parameters could be an indication of a phase transition taking place but it may also be caused by peak broadening or problems with solidifying of the pressure medium. A phase transition can not be detected by looking at changes in the diffraction patterns due to the low resolution. However, a change in compressibility of a and V at between 0.5 and 1.2 GPa indicates that a structural transition may occur in this region.

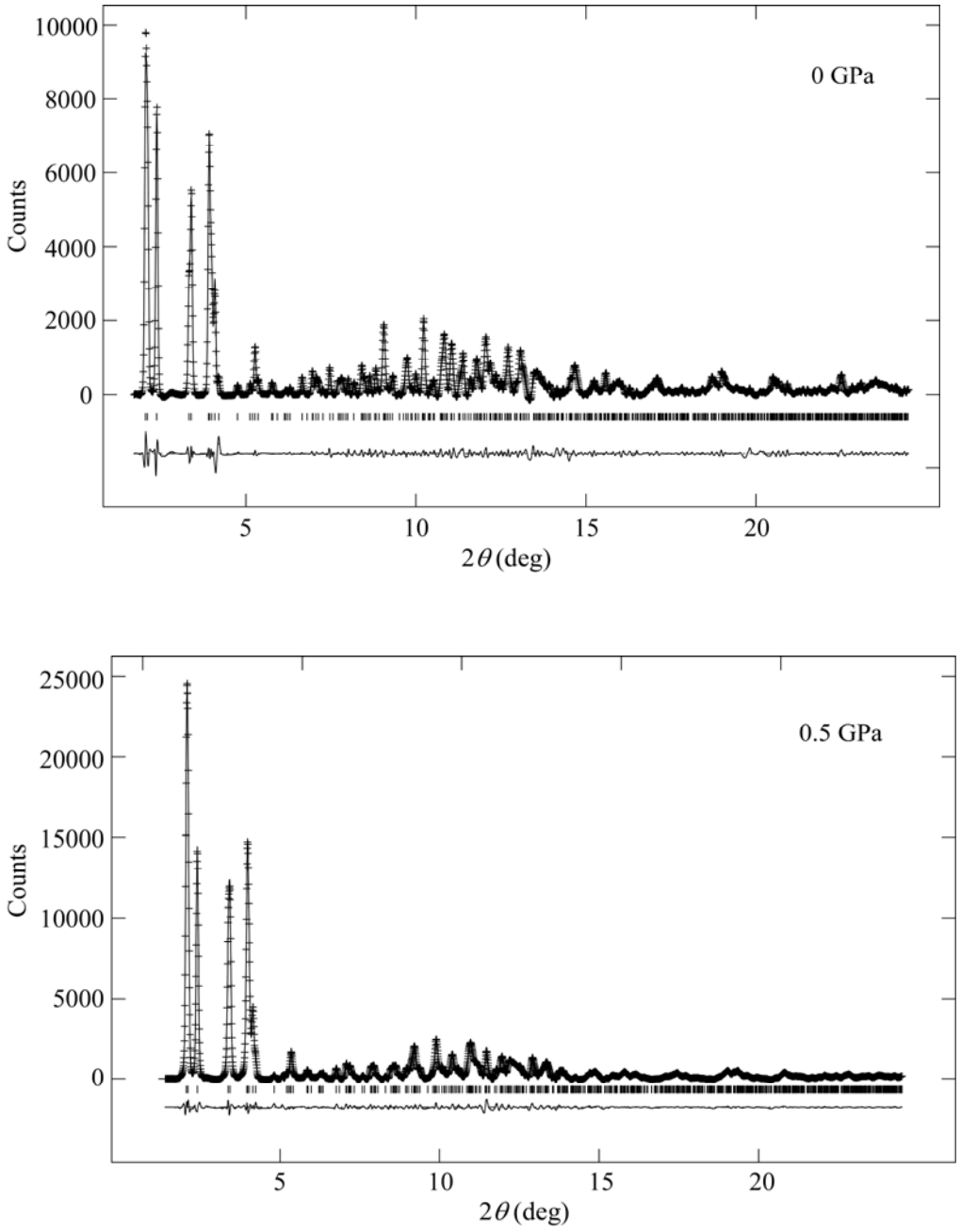

Figure 4.8 Le Bail plots for (EDT-TTF-CONH$_2$)$_6$ (Re$_6$Se$_8$(CN)$_6$) at 0 and 0.5 GPa showing the observed, calculated and difference curves.

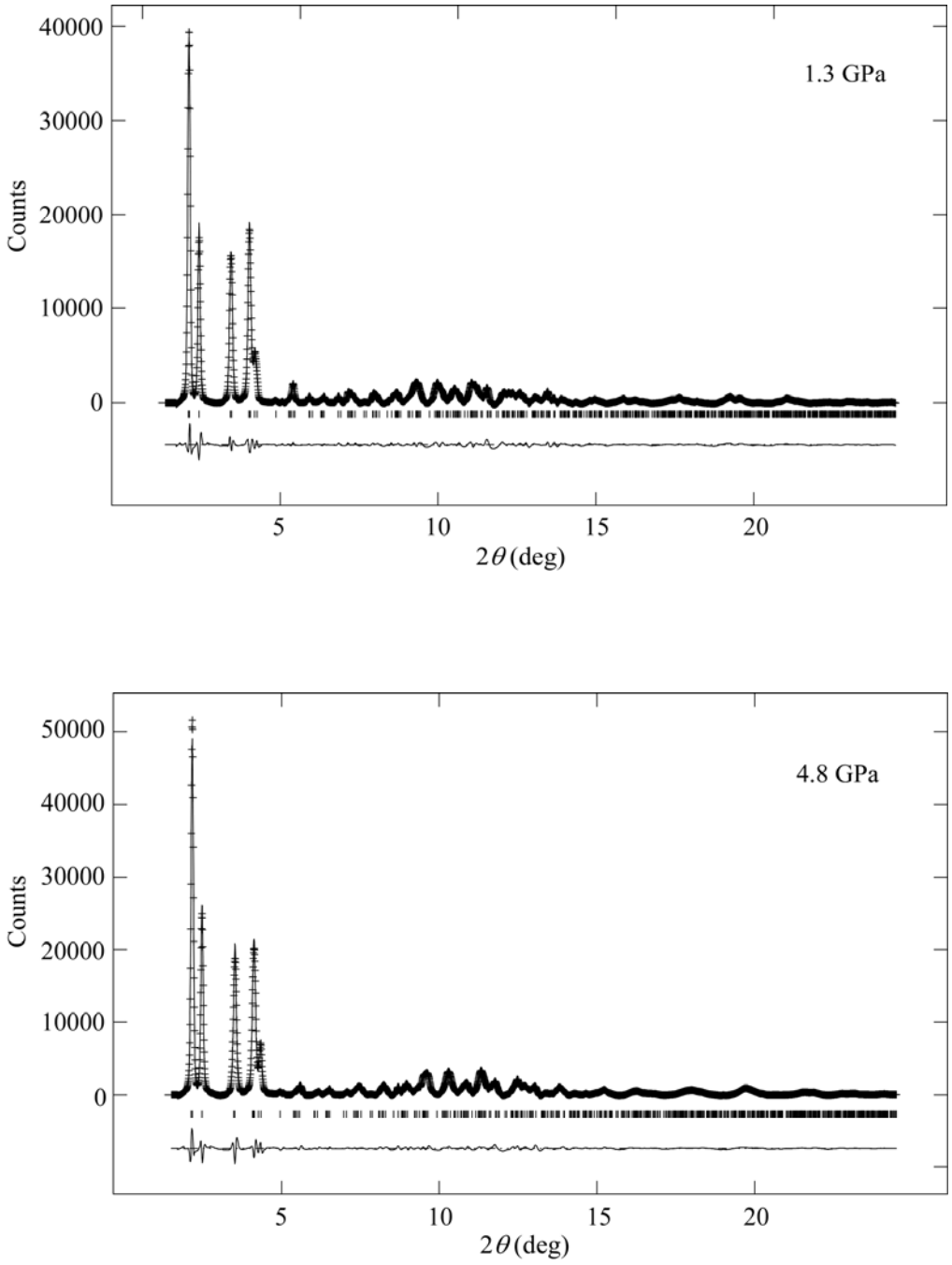

Figure 4.9 Le Bail plots for (EDT-TTF-CONH$_2$)$_6$ (Re$_6$Se$_8$(CN)$_6$) at 1.4 and 4.8 GPa showing the observed, calculated and difference curves.

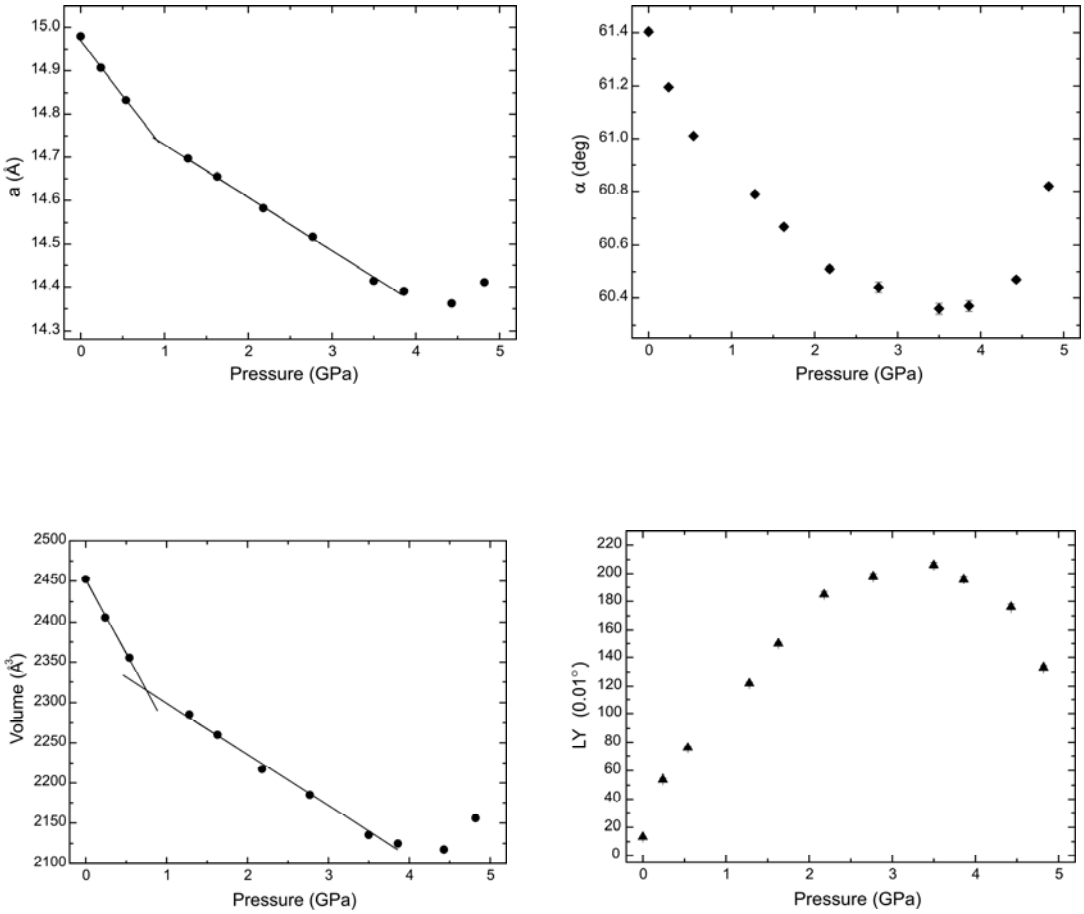

Figure 4.10 Plots of the changes in lattice parameters and Lorenzian profile coefficient with pressure.

4.3.2 Single crystal study

Indexing of the reflections obtained from the single-crystal synchrotron X-ray diffraction experiments at the five pressure points gave the unit cell dimensions listed in Table 4.1. The crystal was rhombohedral at 0 and 0.4 GPa and triclinic above this pressure showing that a single-crystal to single-crystal phase transition has occurred between 0.4 and 0.8 GPa. Refinements of the 0 and 0.4 GPa data were carried out using the rhombohedral space group $R\bar{3}$ and starting from the published coordinates determined at ambient pressure[6]. The vibrational and thermal displacement parameters of all the non-hydrogen atoms were restrained to be similar to the nearest neighbour atoms but were allowed to refine anisotropically. One carbon atom of the ethylenedithio bridge was disordered but the position was determined from the Fourier difference map and the distances around it were restrained. Hydrogen atoms were seen in a difference density synthesis but those attached to carbon atoms were repositioned geometrically. All H atoms were initially refined with soft restraints on the bonds to regularize their geometry after which they were refined with riding constraints only.

Table 4.1

Summary of lattice parameters and R-factors for (EDT-TTF-CONH$_2$)$_6$[Re$_6$Se$_8$(CN)$_6$] at increasing pressure.

Pressure	0 GPa	0.4 GPa	0.8 GPa	1.2 GPa	1.8 GPa
a (Å)	15.0012(1)	14.8819(1)	14.6062(10)	14.585(12)	14.3991(9)
b (Å)	-	-	14.6228(11)	14.6018(14)	14.5069(9)
c (Å)	-	-	14.7892(19)	14.805(20)	14.6179(15)
α (°)	61.409(10)	61.078(10)	90.811(11)	90.869(13)	91.603(12)
β (°)	-	-	119.154(10)	119.081(12)	118.532(12)
V (Å^3)	2462.6(4)	2387.12(4)	2280.4(6)	2278.4(7)	2214.0(5)
γ (°)	-	-	118.971(6)	118.944(7)	118.826(7)
R	0.077	0.063	0.128	0.122	0.125

Owing to the low completeness of the 0.8, 1.2 and 1.8 GPa data sets, all intramolecular distances were restrained to the values observed in the ambient pressure structure, and all non-hydrogen atoms were refined with isotropic displacement parameters. In addition, all atoms within the EDT-TTF-CONH$_2$ molecules were restrained to be planar and the three N≡C and Re-C bonds in the cluster were restrained to the same value. H atoms attached to carbon were placed geometrically and initially refined with soft restraints on the bond lengths and angles to regularize their geometry after which the positions were refined with riding constraints.

Table 4.1 shows the resulting *R*-factors which lies between 7 and 13%. These values are high but typical for refinements of high pressure data sets and are sufficient to identify the main changes in the structural features of the compound with pressure. The $\bar{3}$ symmetry which results in a Kagome pattern of equivalent mixed valence dimers in the (111) layers is retained up to 0.4 GPa (Figure 4.11). Above this pressure the triclinic asymmetric unit contains three independent EDT-TTF-CONH$_2$ molecules giving rise to three symmetry inequivalent dimers as illustrated in Figure 4.12.

Listings of crystal and refinement details are given in Table 4.2 for the 0 and 1.8 GPa data sets. The corresponding information for the 0.4, 0.8 and 1.2 GPa refinements are shown in Appendix B. Refined positions of atoms, thermal parameters and distances and angles for all of the five data sets are listed in appendix B. The settings of the structures here are the same as used in the previously published X-ray diffraction study of (EDT-TTF-CONH$_2$)$_6$[Re$_6$Se$_8$(CN)$_6$] at 295 and 100 K to facilitate a comparison with those results.

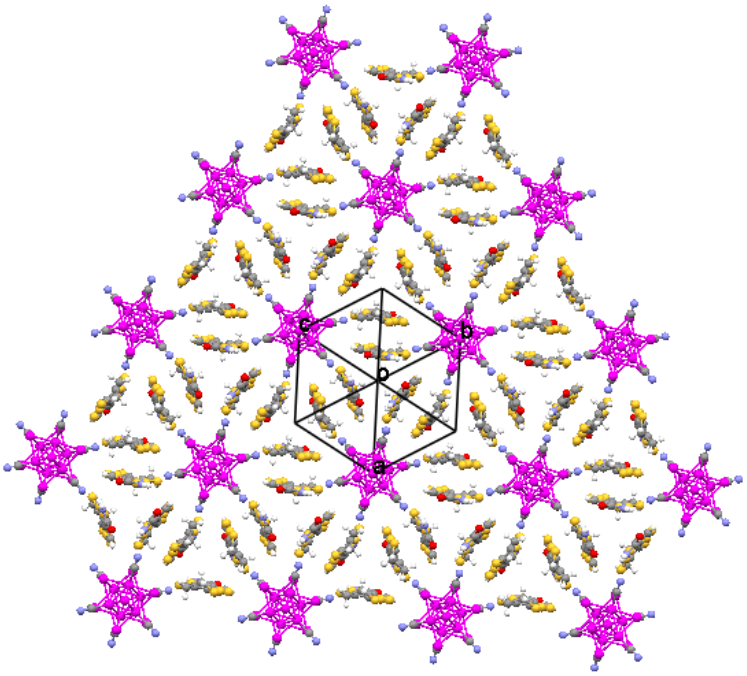

Figure 4.11 Schematic view of the extended network of dimers in the (111) plane at 0.4 GPa illustrating the $R\bar{3}$ Kagome symmetry that remains up to this pressure.

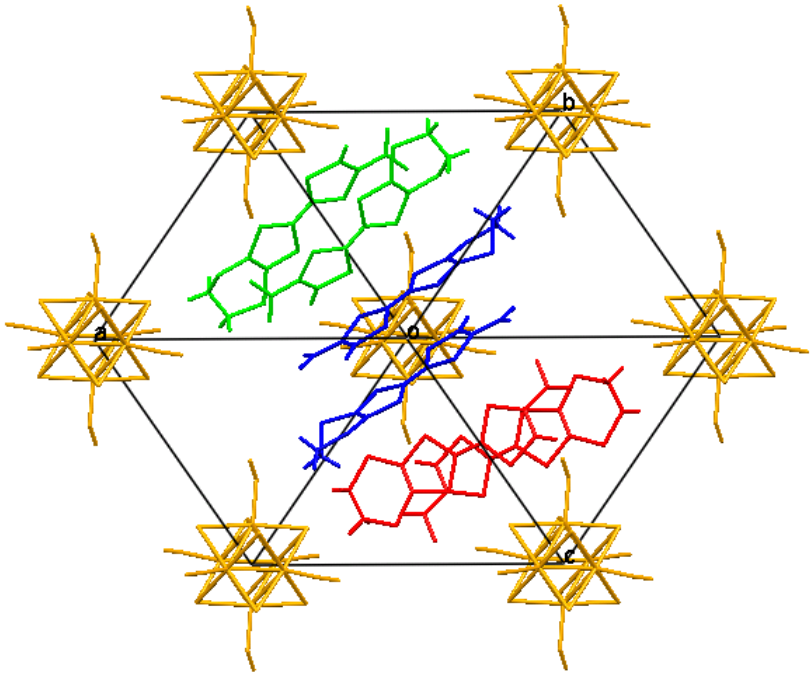

Figure 4.12 View of the 1.8 GPa crystal structure showing the three types of dimers A (blue), B (red) and C (green) which are all different in the triclinic distortion.

Table 4.2

Crystal, collection and refinement details for (EDT-TTF-CONH$_2$)$_6$[Re$_6$Se$_8$(CN)$_6$] at 0 and 1.8 GPa.

Crystal data	**0 GPa**	**1.8 GPa**
Chemical formula	$C_{60}H_{42}N_{12}O_6Re_6S_{36}Se_8$	$C_{60}H_{30}N_{12}O_6Re_6S36Se_8$
M_r	3930.33	3918.24
Cell setting, Space group	Rhombohedral, $R\bar{3}$	Triclinic, $P\bar{1}$
a (Å)	15.00120 (10)	14.2991(9)
b (Å)	-	14.5069(9)
c (Å)	-	14.6179(15)
α (°)	61.4090 (10)	91.603(9)
β (°)	-	118.532(8)
γ (°)	-	118.826(5)
V (Å^3)	2462.60 (4)	2214.0
Z	1	1
D_x (mg m^{-3})	2.650	2.939
Radiation type	Mo $K\alpha$	Mo $K\alpha$
No. of reflections for cell parameters	4451	3207
θ range (°)	4–25	3-26
μ (mm^{-1})	11.12	12.37
Temperature (K)	295	
Crystal form, colour	Prism, black	
Crystal size (mm)	0.1 × 0.1 × 0.1	
Data collection		
Diffractometer	Bruker SMART	
Data collection method	ω scans	
Absorption correction	multi-scan SADABS (Siemens, 1996)	
No. of measured, independent and observed reflections	8627, 1925, 1572	8699, 2737, 1618

Criterion for observed reflections	$I > 2.00\sigma(I)$	
R_{int}	0	0.082
θ_{max} (°)	25	26
Range of *h, k, l*	$h = -6 \rightarrow 14$ $k = -6 \rightarrow 15$ $l = 2 \rightarrow 18$	$h = -18 \rightarrow 18$ $k = -18 \rightarrow 18$ $l = -9 \rightarrow 9$
Refinement		
Refinement on	F^2	
$R[F^2 > 2\sigma(F^2)]$, $wR(F^2)$, S	0.077, 0.229, 0.96	0.125,0.37, 1.23
No. of reflections	1898	2737
No. of parameters	193	257
H-atom treatment	Riding independent and constrained refinement	
Weighting scheme	$w = 1/[\sigma^2(F^2) + (0.09P)^2 + P]$ $P = (\max(F_o^2,0) + 2F_c^2)/3$	$w = 1/[\sigma^2(F^2) + (0.2P)^2 + P]$ $P = (\max(F_o^2,0) + 2F_c^2)/3$
$(\Delta/\sigma)_{max}$	0.0003	0.05
$\Delta\rho_{max}$, $\Delta\rho_{min}$ (e Å^{-3})	2.07, -2.43	5.99, -4.73

4.4 Discussion

The lattice constants obtained from the single crystal refinements at ambient pressure agrees well with those previously published and those of the powder diffraction study. Figure 4.13 shows the variation of the lattice parameters *a, b* and *c*, and the unit cell volume, *V*, with pressure. As expected with an increase in pressure, a decrease of all parameters is observed. There is a noticeable change of the *a* and *b* axis lengths as well as the volume during the transition to the triclinic structure followed by a change incompressibility. The reduction of the *c*-axis with pressure is more regular and there is no sudden change across at the phase transition.

The effect of pressure on the intermolecular hydrogen bonds, defined in Figure 4.14, is plotted in Figure 4.15. Below the phase transition, there is a decrease in all these distances with increased pressure (0.4 GPa) with the biggest difference

seen in the longer and weaker **C**H···**N**≡C and **C**H···**Se** bonds, 2.4 % and 3.3 % respectively. There is a smaller reduction of 1.6 % in the shorter **O**···**N**≡C bond length and 1.9 % in the strong **N**H···**N**≡C bond (the hydrogen bond within the (111) layers). Hence, overall the bond distances are mainly reduced along the [111] direction and it appears the compression of the structure occurs mainly between the Kagome layers rather than within them. In Figure 4.15, there are three different values for each intermolecular hydrogen bond above 0.4 GPa, confirming the loss of the $\bar{3}$ symmetry and the formation of three symmetry inequivalent EDT-TTF-$CONH_2$ molecules, A, B and C, caused by the phase transition. For the strong **N**H···**N**≡C bond, the behaviour of all the molecules is similar, with a steady decrease of the three distances in the pressure range 0-1.8 GPa. The data point at 1.8 GPa for molecule C does not follow the trend but an explanation may be the instability of the C≡N bonds in this refinement creating a larger bond angle and hence an increase in bond distance. A similar situation is observed for the short **O**···H**N** bond with the difference being that whilst a drastic reduction of two of the distances, BC and CA, occurs across the phase transition, the bond lengths are not much reduced on increasing the pressure further. The increase with pressure for molecules A and C in the plots of the **C**H···**N**≡C and **C**H···**Se** bond lengths could be a result of twisting or sliding motions. Considering the quality of the data and the heavy restraints applied during the refinements, it is difficult to determine the exact movements of the individual molecules and the subtle changes of the structure. However, the variation of the trends observed in the plots in Figure 4.15 clearly shows that the molecules are different to each other and move in a different way when pressure is applied.

A clearer picture of what is happening in the structure when pressure is applied can be obtained by looking at the intradimer distances defined in Figure 4.16 and plotted in Figure 4.17. These distances can be used as an indication of a dimer becoming more or less eclipsed. A sliding of the molecules across each other towards a more eclipsed state will result in a reduction of the C(1)-C(2)-C(1) angle as well as the C(1)-C(2) and C(1)-C(1) distances whereas the C(2)-C(2) distance should increase. However, when the system is subjected to high pressure there could also be a reduction in these distances due to the molecules moving closer together. The bond

angle however should become larger if the distance between the two molecules in the dimer becomes smaller.

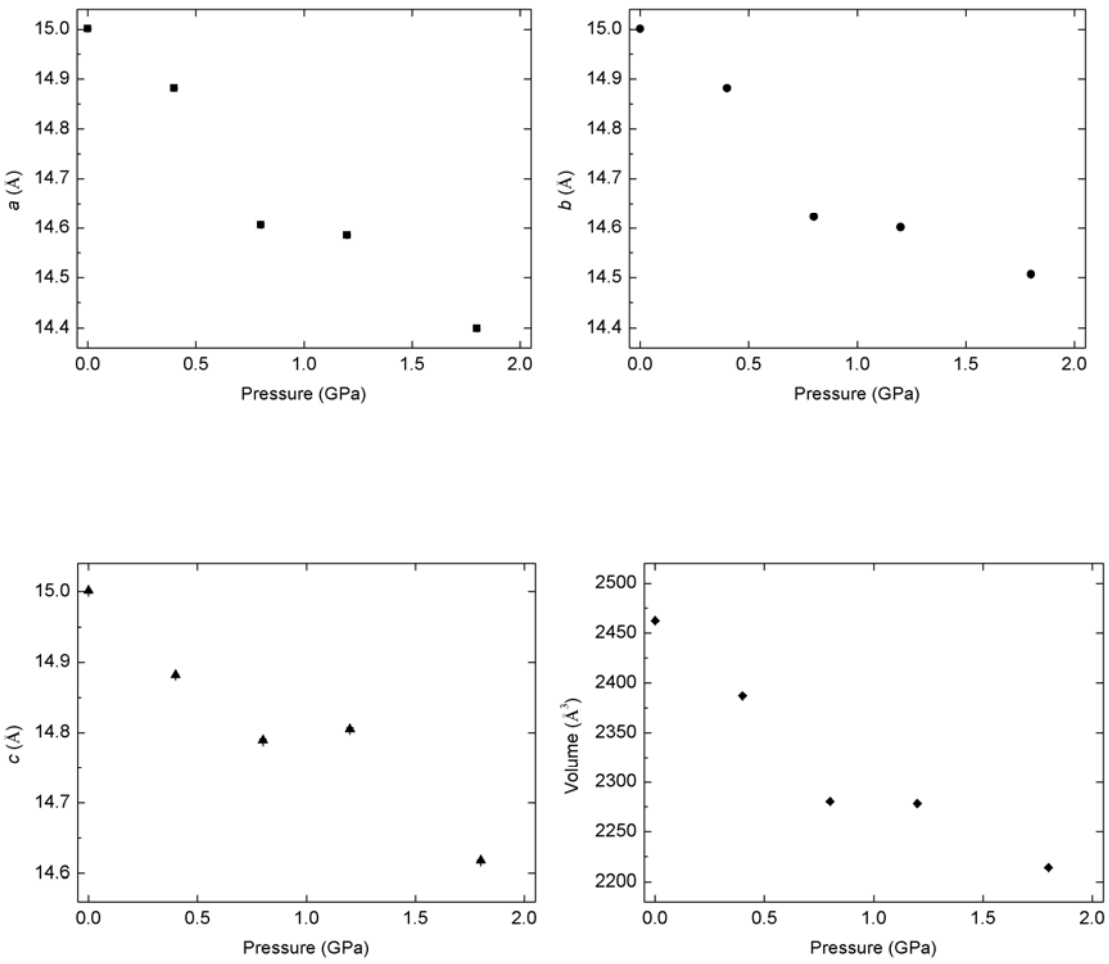

Figure 4.13 Plots showing the variation of the lattice parameters and unit cell volume of (EDT-TTF-CONH$_2$)$_6$[Re$_6$Se$_8$(CN)$_6$] with pressure.

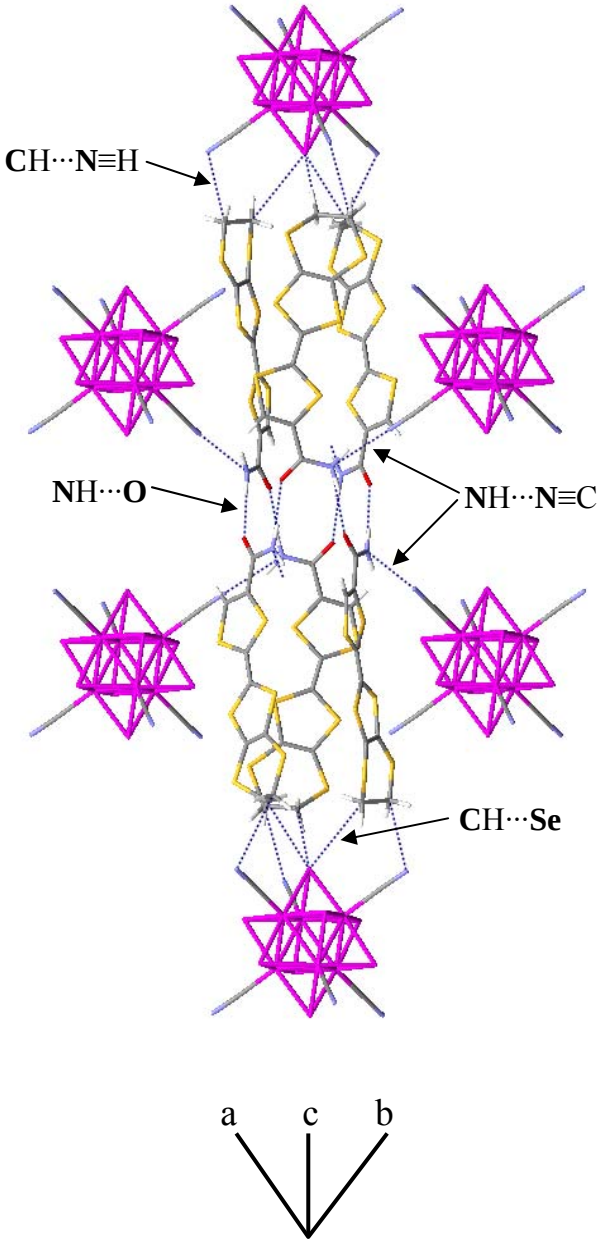

Figure 4.14 Projection of the structure along the [111] direction showing the assembly of molecules and clusters via 4 different hydrogen bonds.

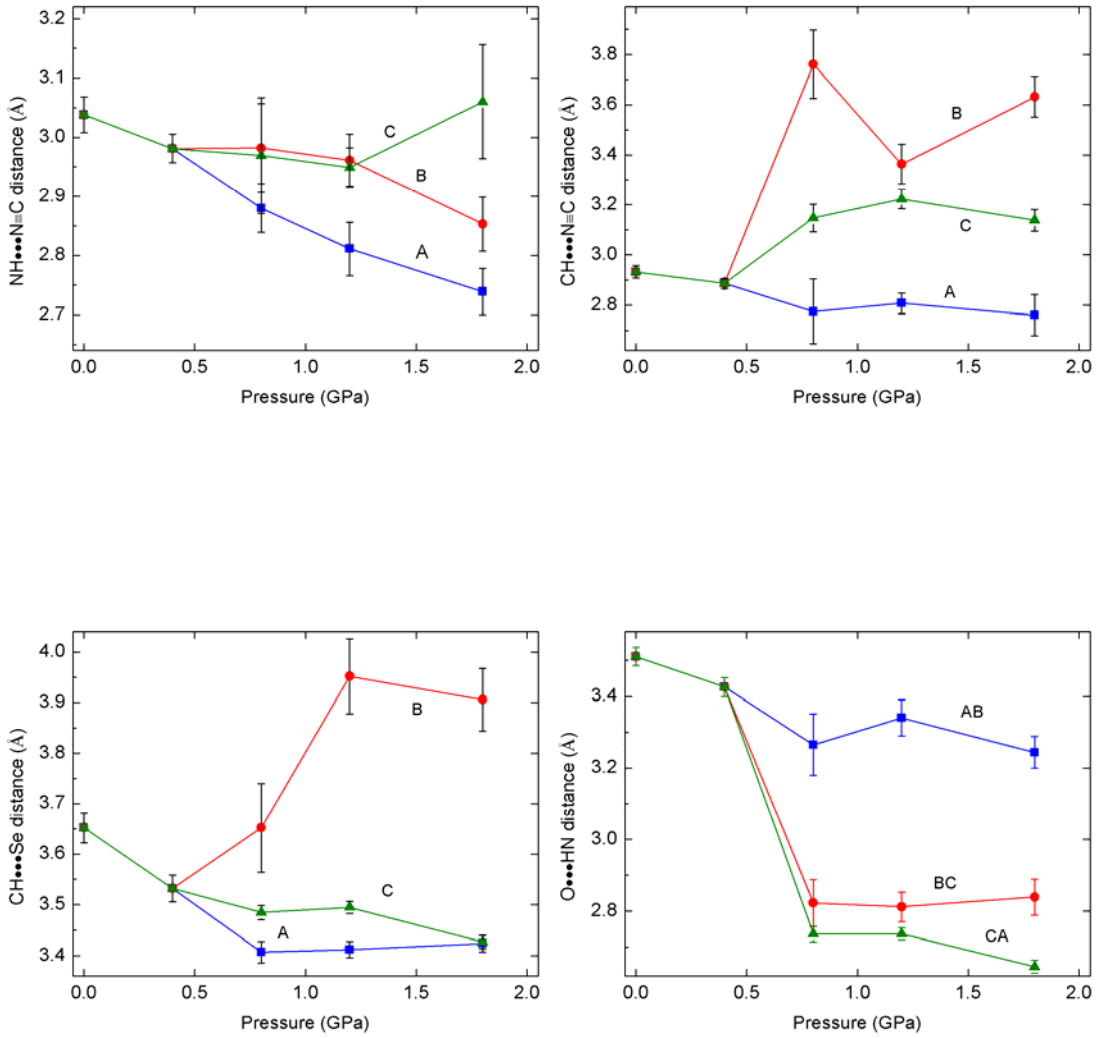

Figure 4.15 Plots showing the variation of the intermolecular hydrogen bond lengths with pressure. The various distances are defined in Figure 4.14 and are measured from the atom bonded to the hydrogen rather than the hydrogen itself as the position of some of the hydrogen atoms could not be refined. The three symmetry inequivalent (EDT-TTF-CONH$_2$)$_6$[Re$_6$Se$_8$(CN)$_6$] molecules are represented by A, B and C.

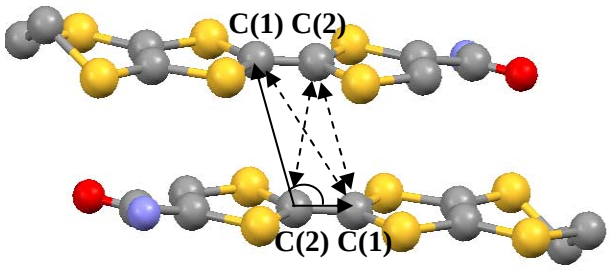

Figure 4.16 Illustration of an EDT-TTF-CONH$_2$ dimer showing the definition of the intradimer angle and various carbon-carbon distances discussed in the text.

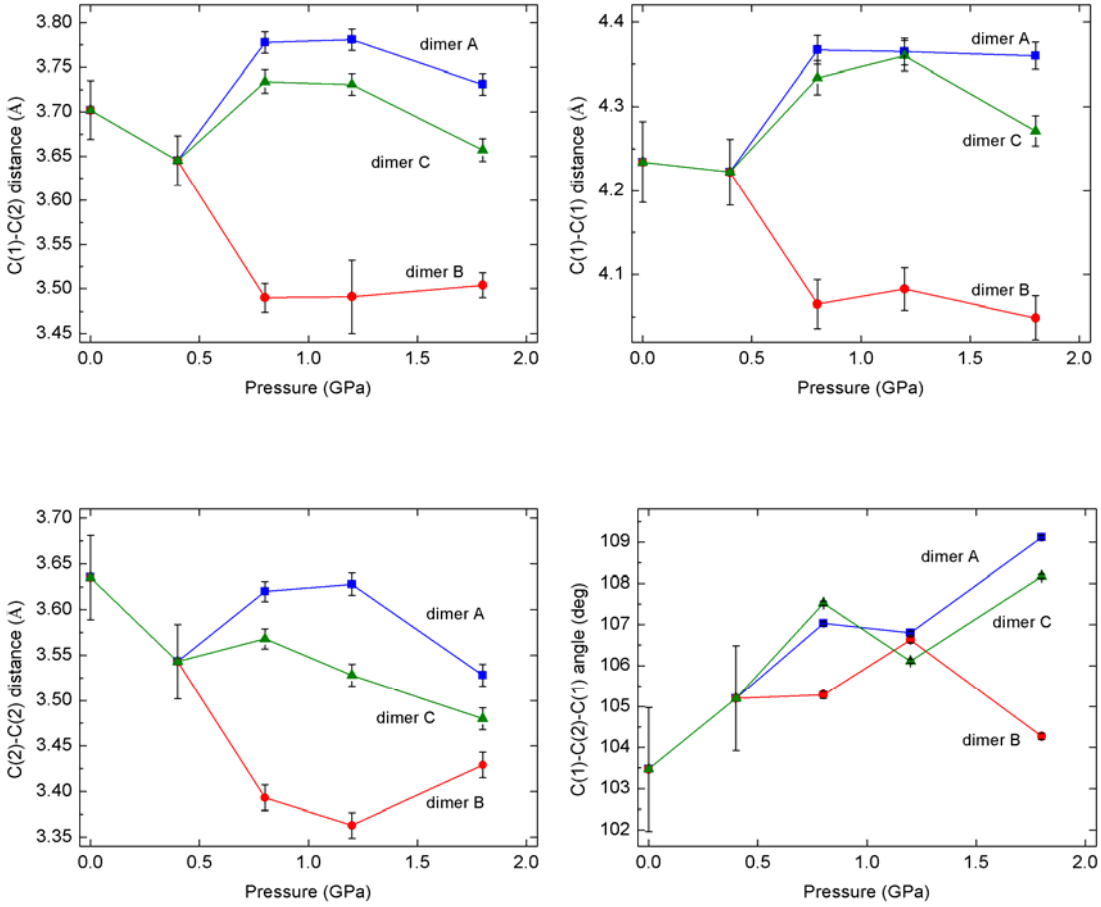

Figure 4.17 Plots showing the variation of chosen intradimer C-C distances and angle with pressure. The distances and angle are defined in figure 4.3 and the three symmetry inequivalent dimers A, B and C are represented by blue, red and green markers respectively.

As predicted, when increasing the pressure below the phase transition there is a decrease in all intradimer carbon-carbon distances and an increase in the C(1)-C(2)-C(1) angle. Above the phase transition there is a clear difference in the behaviour of dimer B compared to dimer A and C. In the latter two, there is sharp rise in the intradimer distances across the phase transition, followed by a gradual decrease with increased pressure along with a gradual increase in the intradimer angle throughout the pressure range. Hence, the phase transition forces the two molecules within these dimers further apart and also causes them to slide away from each other. Applying pressure to the new phase leads to the molecules again moving closer together. In contrast, for dimer B there is at first a sharp drop in the C-C distances after which the curve flattens out for C(1)-C(2) and C(1)-C(1) whereas the C(2)-C(2) value increases. There is no sudden change in the intradimer angle and only a small reduction is seen on further increasing the pressure. This illustrates that the molecules within this dimer slide towards each other as well as move closer together over the phase transition. Above the transition there is further sliding within the dimer with pressure towards a more eclipsed state.

The end result is that at 1.8 GPa the value of the C(1)-C(2)-C(1) angle is similar for dimer A and C, 109.11(44)° and 108.17(47)° respectively, whereas it is considerably smaller for dimer B, 104.27(75)° clearly showing that, in analogy with the low temperature structure, one dimer has become more eclipsed than the other two. The lattice parameters, intradimer angle and distances of the low temperature structure and the 1.8 GPa refinement are listed in Table 4.3. This shows that the more eclipsed dimer B is the same (by symmetry) as in the low temperature (100 K) structure. The difference in lattice parameters shows that the structure is, as expected, much more compressed at high pressure but interestingly, the intradimer distances are larger. Again, indicating that the compression under pressure occurs mainly along [111] as opposed to within the cluster/dimer layers. It is also clear that the intradimer angle in dimer B is lower in the 100 K structure most likely because the dimer is simply less eclipsed at high pressure.

4.5 Conclusions

In conclusion, the structural properties of (EDT-TTF-$CONH_2$)$_6$[$Re_6Se_8(CN)_6$] are strongly affected by the application of pressure with the effects of increased pressure being analogous to those of a lowering of the temperature. A phase transition occurs between 0.4 and 0.8 GPa to a triclinic $P\bar{1}$ structure. Changes in the intermolecular and intradimer distances revealed that a sliding motion within one of the dimers results in it being more eclipsed due to charge localisation of an extra hole of one of the dimers. Hence, it has been shown that high pressure as well as low temperature can drive the charge ordering transition in (EDT-TTF-$CONH_2$)$_6$ [$Re_6Se_8(CN)_6$]. Measuring the physical properties at high pressure would be required to confirm if the transition is sufficient to cause the insulating behaviour seen at low temperature.

Table 4.3

Lattice parameters, intradimer angle and distances for the low temperature (100 K) and high pressure (1.8 GPa) structures of (EDT-TTF-$CONH_2$)$_6$[$Re_6Se_8(CN)_6$].

Lattice parameters		100 K (0 GPa) [6]	1.8 GPa (300 K)
a (Å)		14.7776(16)	14.3991(9)
b (Å)		14.7849(15)	14.5069(9)
c (Å)		15.1131(17)	14.6179(15)
α (°)		91.286(13)	91.603(9)
β (°)		118.886(11)	118.532(8)
γ (°)		118.210(11)	118.826(5)
Intradimer distances (Å)/angles (°)			
Dimer A	C(1)-C(2)	3.549	3.731
	C(1)-C(1)	4.219	4.360
	C(2)-(2)	3.340	3.528
	C(1)-C(2)-C(1)	109.95	109.11
Dimer B	C(1)-C(2)	3.445	3.504
	C(1)-C(1)	3.976	4.049
	C(2)-(2)	3.477	3.429
	C(1)-C(2)-C(1)	100.78	104.27
Dimer C	C(1)-C(2)	3.588	3.657
	C(1)-C(1)	4.250	4.271
	C(2)-(2)	3.400	3.480
	C(1)-C(2)-C(1)	108.98	108.17

4.6 References

1. T. Takahashi, *J. Phys. Chem. Solids*, **62**, 105 (2001).
2. M. Bendikov, F. Wudl and D.F. Perepichka, *Chem. Rev.*, **104**, 4891 (2004).
3. J. Ferraris, D.O. Cowan, V. Walatka and J.H. Perlstein, *J. Am. Chem. Soc.*, **95**, 948-949 (1973).
4. H. Kobayashi, A. Kobayashi and P. Cassoux, *Chem. Soc. Rev.*, **29**, 325 (2000).
5. R.J. Hemley, *Annu. Rev. Phys. Chem.*, **51**, 763 (2000).
6. S.A. Baudron, P. Batail, C. Coulon, R. Clerac, E. Canadell, V. Laukhin, R. Melzi, P. Wzietek, D. Jerome, P. Auban-Senzier and S. Ravy, *J. Am. Chem. Soc.*, **127**, 11785 (2005).
7. F. Mila, *Phys. Rev. Lett*, **81**, 2356 (1998).
8. A. Harrison, *J. Phys. Condens. Matter*, **16**, S553 (2004).
9. K. Awaga, T. Inabe, Y. Maruyama, T. Nakamura and M. Matsumoto, *Chem. Phys. Lett.*, **195**, 21 (1992).
10. K. Awaga, T. Okuno, A. Yamaguchi, M. Hasegawa, T. Inabe, Y. Maruyama and N. Wada, *Phys. Rev. B*, **49**, 3975 (1994).
11. P. Batail, K. Boubekeur, M. Fourmigue and J.C.P. Gabriel, *Chem. Mater.*, **10**, 3005 (1998).
12. L. Merrill and W.A. Bassett, *Rev. Sci. Instr.*, **45**, 290 (1974).
13. H.K. Mao, J. Xu and P.M. Bell, *J. Geophys. Res.*, **91**, 4673 (1986).
14. A. Dawson, D.R. Allan, S. Parsons and M. Ruf, *J. Appl. Cryst.*, **37**, 410 (2004).
15. Siemens, *Area-Detector Integration Software*; Siemens Industrial Autom.: Madison, WI, 1995.
16. G.M. Sheldrick, University of Gottingen and Bruker AXS: Madison, WI, 2001.
17. S. Parsons, *SHADE*; The University of Edinburgh, UK, 2004.
18. P.W. Betteridge, J.R. Carruthers, R.I. Cooper, K. Prout and D.J. Watkin, *J. Appl. Cryst.*, **36**, 1487 (2003).
19. A. Le Bail, H. Duroy and J.L. Fourquet, *Mater. Res. Bull.*, **23**, 447 (1988).

Chapter 5

Neutron diffraction study of $KCrF_3$

5.1 Introduction

Perovskite-type compounds have been comprehensively studied during the past 50 years because of the remarkable properties they exhibit and their potential and actual applications as magnetoresistors, ferroelectrics, ionic-, semi- and superconductors. Whilst most of the research in this field has been focused almost solely on transition metal oxides, much less information is available in the literature about the chemistry and physics of the transition metal fluorides, possibly due to the difficulties involved in synthesising some of these materials. However, fluorides with the general formulae $M^{3+}F_3$, $AM^{2+}F_3$, $A_2M^{2+}F_4$ and $A'M^{2+}F_4$, where A = alkali metal, A' = alkaline earth and M = transition metal, have been known for a long time and several of them have been extensively studied, especially because of their interesting magnetic properties. The variable spatial distribution of the MF_6 octahedra gives rise to one-dimensional chain structures[1], two-dimensional layered arrangements as well as three-dimensional networks like those seen in perovskite, rutile and pyrochlore structures. For example, the $KM^{2+}F_3$ fluorides with M^{2+} = Mn, Fe, Co, Ni, Cu and Cr, which have been the subject of several studies since the early sixties[2-5] adopt perovskite-type structures and order antiferromagnetically with $KNiF_3$ having the highest Néel temperature of 280 K[2]. In particular, much interest has been generated by $KCuF_3$ as it behaves like a model one-dimensional, S = ½, Heisenberg antiferromagnet with the magnetic response caused by orbital ordering which in turn is stabilised by the Jahn-Teller distortions of the Cu^{2+} ions[6]. Likewise, the $A_2M^{2+}F_4$ fluorides form a K_2NiF_4 layered structure, closely related to La_2CuO_4 (the parent compound of the high T_C-superconductors)[7]. In this series, A_2CuF_4 is ferromagnetic whereas the Co, Ni, Fe and Mn compounds are all antiferromagnetic[8]. The interest in this family of materials has been revived since

the discovery of new characteristics such as the unusual example of the orbitally ordered two-dimensional, Heisenberg, ferromagnet, Cs_2AgF_4, which shows strongly correlated magnetic beaviour[9]. The unique electronic, magnetic and crystal features of the ternary transition metal fluorides make these systems an interesting alternative to the much studied oxide analogues both with respect to fundamental studies of strongly correlated electron systems and potential technological applications. One of the vital factors at the origin of the exciting effects in these compounds is the availability of degenerate electronic orbitals. Whether such orbital degrees-of-freedom is possible in a material is dependant on the nature of the atomic ions and the surrounding crystallographic structure. Well known examples of ions that display active orbital degrees of freedom include the Jahn-Teller Mn^{3+} and Cu^{2+} ions with the former found in many important transition metal oxides such as $LaMnO_3$, the parent compound of the colossal magnetoresistance manganites[10].

$KCrF_3$ is a ternary fluoride which incorporates the Jahn-Teller active Cr^{2+} (d^4) ion whose electronic and magnetic response is equivalent to those of Mn^{3+} and Cu^{2+}. Hence, the properties of $KCrF_3$ are closely related to those of both $LaMnO_3$ and $KCuF_3$. In $LaMnO_3$, the Jahn-Teller distortions leads to an antiferrodistortive orbital ordering in the basal plane that, in turn, results in an A-type antiferromagnetic spin configuration as shown in Figure 5.1[11].

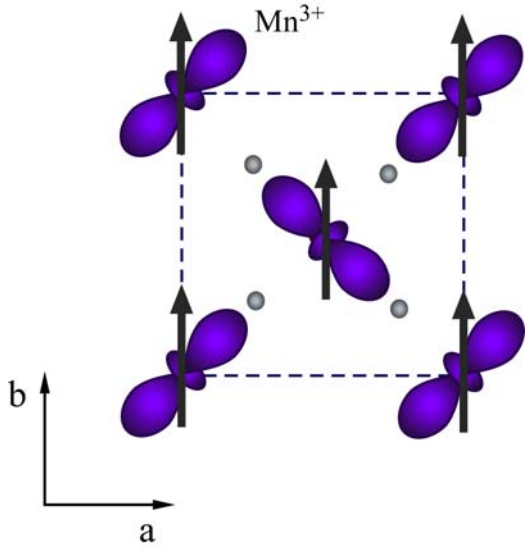

Figure 5.1 Schematic view of the orbital and spin ordering in the *a*-*b* plane of $LaMnO_3$. Antiferromagnetic coupling between planes along the *c*-axis yields the A-type structure.

The first structural studies of $KCrF_3$ were made in the late 1950s and early 60s and they proposed that the crystal structure was primitive tetragonal at room temperature, space group *P4/mmm* with a = 4.27 Å and c = 4.01 Å[5, 12, 13]. However, recent synchrotron X-ray diffraction studies have suggested that at ambient conditions the structure is body-centred tetragonal, space group *I4/mcm*, with $a = b \approx \sqrt{2}a_p$ and $c \approx 2a_p$, where a_p is the lattice constant for the pseudocubic perovskite cell. The lattice parameters were found to be reminiscent of those in $KCuF_3$ [14, 15] with a = 6.05230(2) Å, c = 8.02198(4) Å and $a = b > c/\sqrt{2}$. The Rietveld refinements showed the CrF_6 octahedra to be strongly axially distorted, consisting of short Cr-F bonds along the *c*-axis and alternating long and short Cr-F bonds in the *ab*-plane, providing evidence for the presence of cooperative Jan-Teller distortions. Consequently, the $3d_{x^2-r^2}$ and $3d_{y^2-r^2}$ orbitals are thought to be antiferrodistortively ordered in the *ab* plane (Figure 5.2(a)). Along the *c*-axis, the orbital ordering pattern is rotated by 90° in consecutive layers in an A-type arrangement.

The tetragonal room temperature phase remains stable upon heating up to 923 K when an abrupt phase transition occurs to an ideal cubic structure. Above this temperature the Jahn-Teller distortions of the Cr^{2+} ions are suppressed and the Cr-F bond distances become equivalent. Hence, the structure is made up of corner-sharing undistorted octahedral of F^- anions with Cr^{2+} at the centres. Due to the suppression of the Jahn-Teller distortions, the structural phase transformation is accompanied by an abrupt transition form an orbitally ordered to disordered state. There is also a sudden change in the unit cell parameters at the transition temperature, with a large negative thermal expansion ($\delta V/V$ = 0.44 %)[16]. This behaviour can be explained by the larger volume occupied by the CrF_6 octahedra when the Jahn-Teller distortions are present, leading in turn to a less efficiently packed arrangement. At present, there are no other related ternary perovskite-type fluorites that adopt the same orbitally disordered cubic phase at high temperatures but similar behaviour has been reported for the perovskite manganites[17].

Unlike $KCuF_3$, which remains tetragonal down to 4 K[15], $KCrF_3$ goes through a phase transition at 250 K to a monoclinic structure, space group *I*112/*m*,

with prominent tilting of the CrF_6 octahedra. This structural model has two crystallographically independent Cr^{2+} sites which is unusual for simple ABX_3-perovskite type materials with isovalent B-site cations but it is similar to the heavily distorted crystal structure of $NaCuF_3$[18], which contains four inequivalent Cu^{2+} sites. The bond ordering of long and short Cr-F bonds and the antiferro-type pattern of the $3d_{z^2}$ orbitals is preserved but now occurs in the plane defined by the *c*-axis and the $[1\bar{1}0]$ base diagonal, with a stacking of consecutive planes rotated by 90˚ in the [110] direction (Figure 5.2(b)).

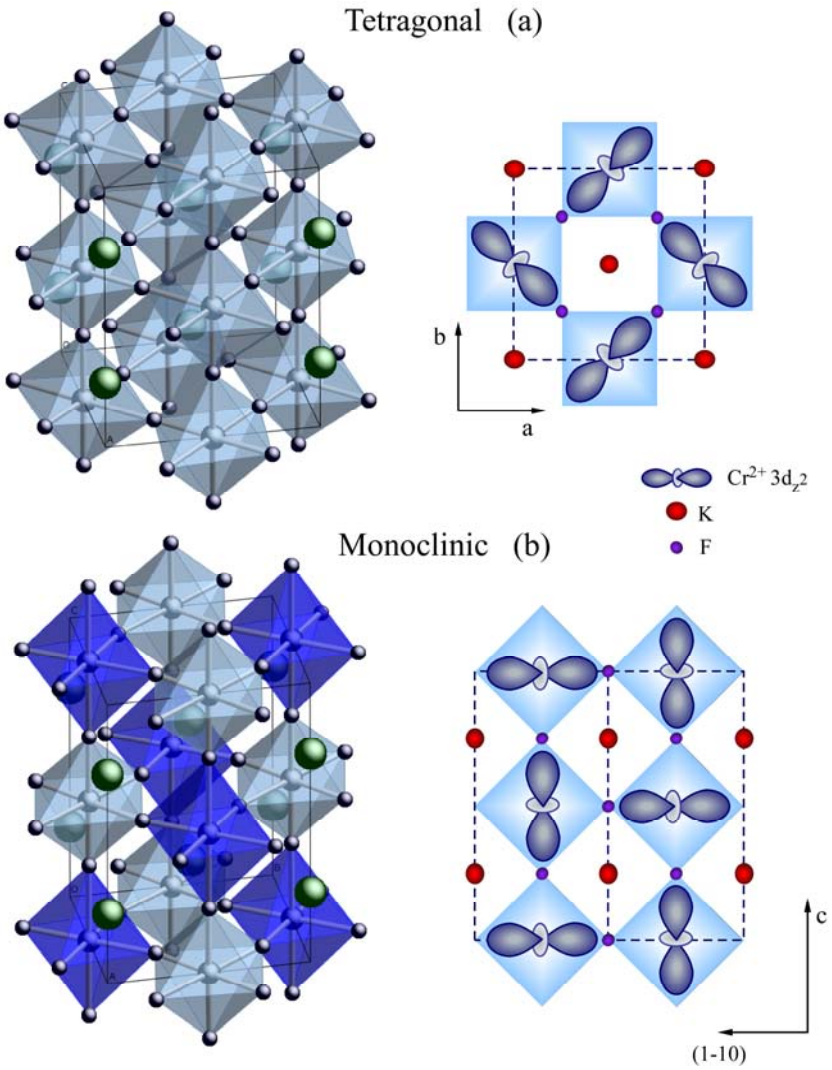

Figure 5.2 The room temperature tetragonal (a) and low temperature monoclinic (b) structures of $KCrF_3$ with the corresponding $3d_z^2$ orbital ordering schemes. The light and dark blue octahedra represent the two different chromium sites, Cr(1) and Cr(2).

It has been reported that $KCrF_3$ adopts an A-type antiferromagnetic structure[2]. Magnetic susceptibility measurements on $KCrF_3$ showed the onset of long range antiferromagnetic order at 46 K with a positive Weiss temperature, θ = 2.7(1) K, indicating the existence of ferromagnetic exchange interactions. The effective magnetic moment was reported to be 4.7 μ_B, consistent with that for high spin Cr^{2+}[19]. This study investigates the magnetic and crystal structure as well as the orbital ordering in $KCrF_3$ using variable temperature powder neutron diffraction.

5.2 Experimental

5.2.1 Synthesis

The polycrystalline $KCrF_3$ samples used were prepared by S. Margadonna *et al* at the University of Edinburgh[16]. Stoichiometric amounts of anhydrous KF (40 mg) and CrF_2 (62 mg) were mixed and cold pressed into 7 mm pellets inside an anaerobic moisture-free glove box after first being pre-dried under vacuum (10^{-5} torr) at high temperature. The pellets were then loaded into and sealed in a molybdenum cell which was put inside an evacuated quartz tube and heated at 550˚C for 2 days with one intermediate grinding.

5.2.2 Diffraction measurements

Constant wavelength high resolution neutron powder diffraction data were recorded using the instrument Super-D2B at the ILL, Grenoble, with a wavelength of λ = 1.594 Å selected from the (355) Bragg reflection of the Ge crystals. The sample was pre-sealed in a vanadium can in a nitrogen filled glove box and patterns were collected at 3.5, 10, 100 and 300 K over the range $10° < 2\theta < 149°$ with a step size of 0.05°. The collection times were 400 min for the 300 K data and 280 min for the other patterns. Data analysis was performed with the GSAS suite of Rietveld[20, 21] analysis programmes.

5.3 Results

The crystal structure for $KCrF_3$ was fitted at 300 K with the *I*4/*mcm* symmetry using a starting model from a previous X-ray diffraction study[19]. It is known that a phase transition occurs at 250 K and therefore the 100 K data was refined in the space group *I*112/*m* with a starting model from the same study. The peak shape was defined using a pseudo-Voigt function and the background described by a linear interpolation function with 36 terms. Due to the small sample volume and inclusion of unidentified impurities, the background was relatively high and the fit could not be significantly improved by using manual background points. The isotropic displacement parameters were refined independently and the fluoride content was confirmed as being stoichiometric by refinement of fractional occupancies. The refined structural models are in good agreement with those previously published. Figure 5.3 shows the Rietveld fits for the 300 K and 100 K data including the splitting of the (220) Bragg reflection into the (004) and ($\bar{2}$20) reflections that confirm the phase transition from a tetragonal to a monoclinic structure. Crystallographic parameters, calculated distances and angles, and *R*-factors are given in Table 5.1 and Table 5.2.

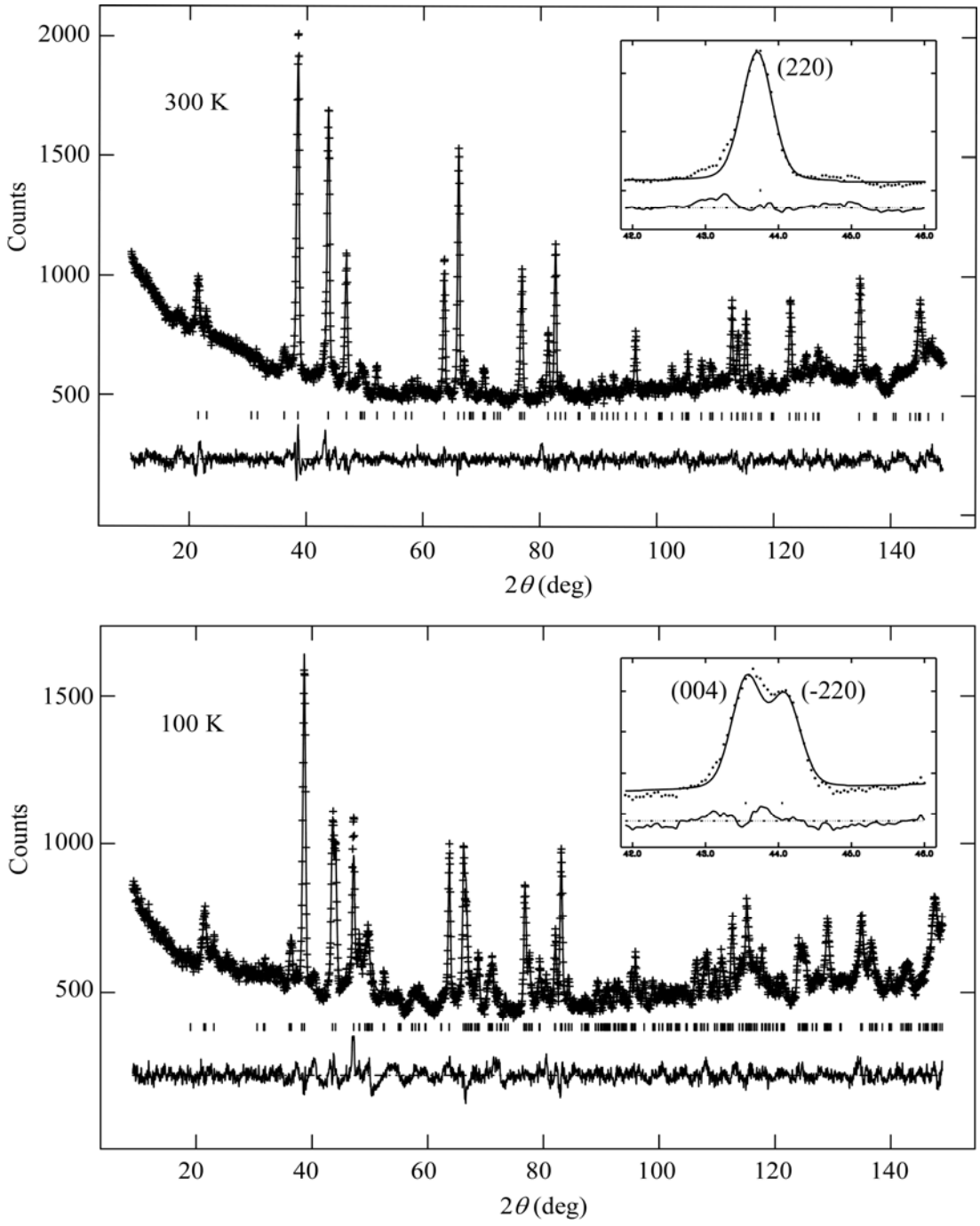

Figure 5.2 Observed calculated and difference plots for KCrF3 at 300 K (above) and 100 K (below) with a selected region of the profile inlaid to show the splitting of the tetragonal (002) reflection into the (004) and $(\bar{2}20)$ monoclinic reflections.

Table 5.1

Crystallographic parameters, calculated distances and Rietveld reliability factors for $KCrF_3$ at 300 K.

300 K; Space group *I4/mcm*, a = 6.0573(3) Å and c = 8.0279(4) Å					
Atom	Site	x	y	z	$U_{iso} \times 100$ (Å^2)
K	*4a*	0	0	0.25	2.83(17)
Cr	*4d*	0	0.5	0	0.81(8)
F(1)	*4b*	0	0.5	0.25	2.62(11)
F(2)	*8h*	0.2287(3)	0.7287(3)	0	2.47(7)
Distances					
Bond				Length (Å)	
Cr-F(1) (×2)				2.007(1)	
Cr-F(2) (×2)				1.959(3)	
Cr-F(2) (×2)				2.324(3)	
Reliability factors: χ^2 = 1.47, R_{wp} = 3.07 %, R_p = 2.38 %, R_{F2} = 9.77 %					

Table 5.2

Crystallographic parameters, calculated distances and angles and Rietveld reliability factors for $KCrF_3$ at 100 K.

100 K; Space group $I112/m$, a = 5.8099(4) Å, b = 5.8222(4) Å, c = 8.5839(4) Å and γ = 93.689(5)°					
Atom	Site	x	y	z	$U_{iso} \times 100$ (Å^2)
K	*4g*	0	0	0.251(1)	0.21(16)
Cr(1)	*2c*	0	0.5	0	0.06(13)
Cr(2)	*2d*	0	0.5	0.5	0.06(13)
F(1)	*4h*	0	0.5	0.232(1)	0.53(7)
F(2)	*4i*	0.280(2)	0.711(2)	0	0.53(7)
F(3)	*4i*	0.230(2)	0.194(1)	0	0.53(7)

Distances and angles			
Bond	Length (Å)	Angle	Angle (˚)
Cr(1)-F(1) (×2)	1.987(6)	Cr(1)-F(1)-Cr(2)	180
Cr(1)-F(2) (×2)	1.975(9)	Cr(1)-F(2)-Cr(2)	163.12(23)
Cr(1)-F(3) (×2)	2.295(7)	Cr(1)-F(3)-Cr(2)	163.65(27)
Cr(2)-F(1) (×2)	2.305(6)	F(2)-Cr(1)-F(3)	89.12(19)
Cr(2)-F(2) (×2)	2.047(9)	F(2)-Cr(2)-F(3)	89.65(19)
Cr(2)-F(3) (×2)	1.991(7)		

Reliability factors: χ^2 = 1.84, R_{wp} = 3.59 %, R_p = 2.78 %, R_{F2} = 12.67 %

On cooling, no further phase transitions were observed and good fits were achieved for both the 10 and 3.5 K data using the *I*112/*m* space group. However, several additional diffraction peaks emerge with the most prominent found at $2\theta = 11.4^{\circ}$ at 3.5 K as illustrated in Figure 5.4. These reflections arise from the long-range magnetic ordering of the $KCrF_3$ phase and could be indexed on the basis of a unit cell with twice the volume of the structural cell having the lattice parameters $a_m = 2\ a_n$, $b_m = b_n$ and $c_m = c_n$ where *m* and *n* refers to the magnetic and nuclear structure respectively. Only peaks with $h = 2n + 1$ and even values of *k* and *l* appear (Figure 5.5) indicating that the spins are parallel in the (100) plane but alternating in the [001] direction. The strongest magnetic peak can be indexed as the (100) reflection and is also an indication of the spins lying close to the (100) plane. The magnetic structure was refined as an independent phase where only the chromium positions were defined and only the magnetic scattering was calculated. A magnetic supercell was used for the fit, related to the structural cell by the following transformation matrix.

$$\begin{pmatrix} a_m \\ b_m \\ c_m \end{pmatrix} = \begin{pmatrix} 0 & \bar{1} & 0 \\ 1 & \bar{1} & 0 \\ 0 & 0 & 1 \end{pmatrix} \begin{pmatrix} a \\ b \\ c \end{pmatrix}$$

This cell has the space group symmetry *A*112/*m* with a volume twice as large as the structural cell. The magnetic model consists of one spin at each of the independent Cr(1) and Cr(2) sites and their equivalent positions under the *A*112/*m* symmetry group operations. Both the Cr moments were constrained to be parallel and of equal magnitude. Good fits were obtained to the data with a time reversal (spin inversion) operation on the 2 fold screw axis operation and hence, the Shubnikov group, or magnetic symmetry group, is *A*112'/*m*. This results in an A-type antiferromagnetic structure consisting of ferromagnetic planes coupled antiferromagnetically along *a* as illustrated in Figure 5.6. The thermal factors were constrained to be the same for Cr(1) and Cr(2) and the three fluoride atoms to stabilise the refinement.

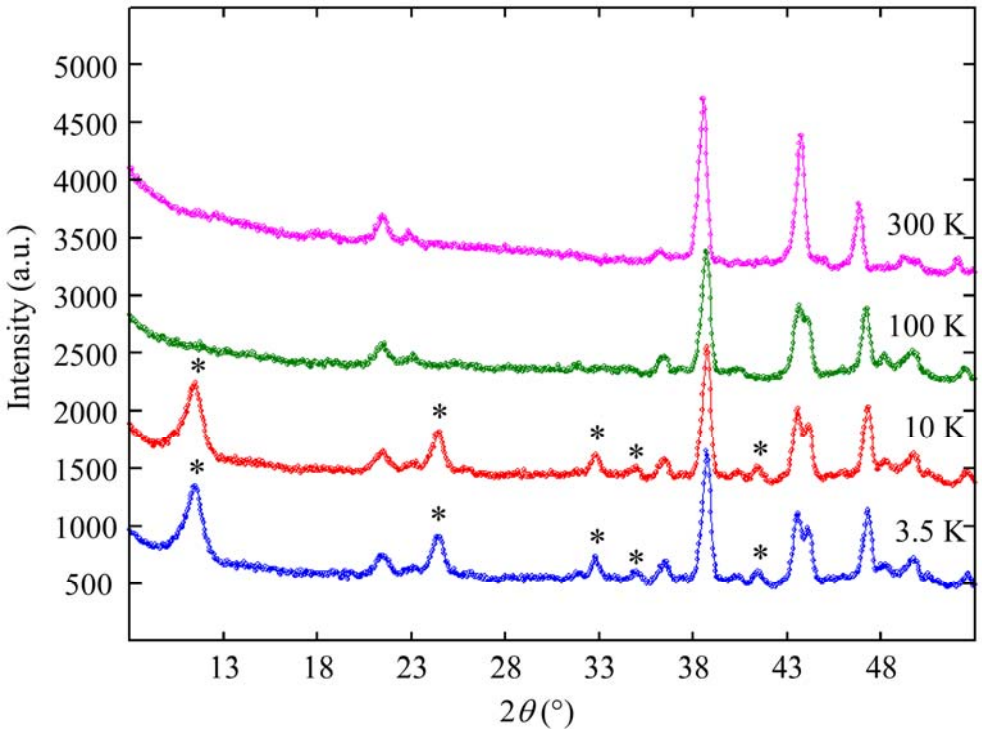

Figure 5.4 Neutron diffraction patterns of $KCrF_3$ at decreasing temperatures showing the appearance of magnetic peaks (marked *).

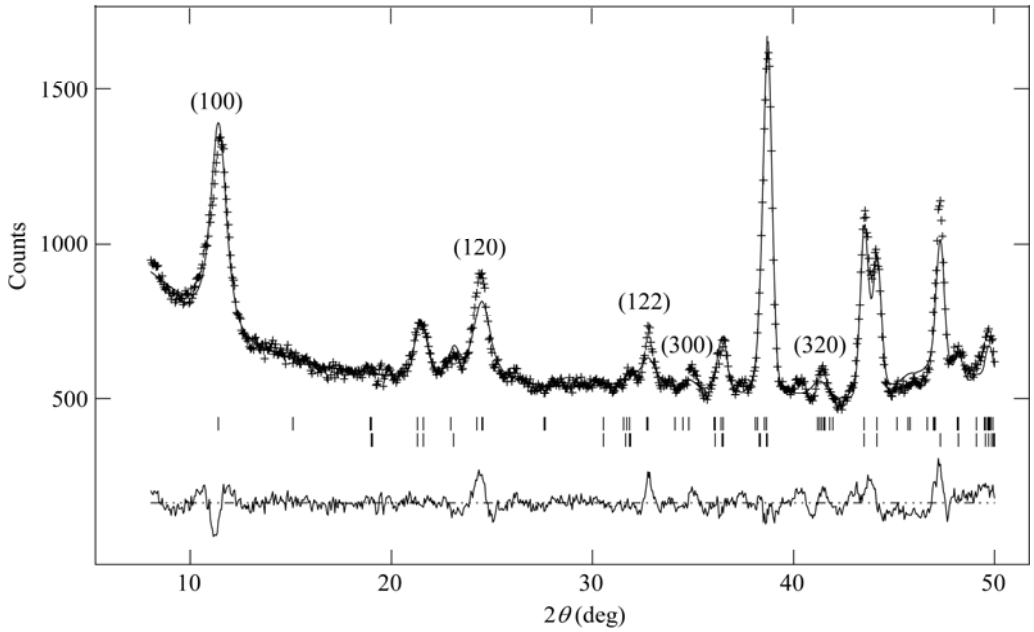

Figure 5.5 Rietveld fit of the low angle region of the crystal and magnetic structure at 3.5 K showing the (100), (120), (122), (300) and (320) reflections of the $KCrF_3$ magnetic cell.

The fit of this antiferromagnetic model to the 10 and 3.5 K data is shown in Figure 5.7 and the results of the converged refinement are listed in Table 5.3 and Table 5.4. The refined magnetic moments were 4.39(8) and 4.39(7) μ_B at 10 and 3.5 K respectively. An attempt was made to refine the magnetic structure using the same antiferromagnetic model but with the moments lying in the *ab*-plane. This was achieved by using the Shubnikov symmetry group *A*112/*m*' but there was no improvement of the fit or the refined residuals. The resulting Cr moment was 4.83(8) μ_B at 3.5 K.

The Lorentzian peak shape parameters for the structural and magnetic phase were refined independently and resulted in a larger value for the latter indicating that the coherence length for the magnetic structure is smaller than that of the crystal structure. A calculation of the extent of the magnetic ordering was made using the Scherrer equation for particle size broadening[22, 23]:

$$p = \frac{18000K\lambda}{\pi LX} \qquad (5.1)$$

where p is the particle size (in the unit Å) , $K \approx 0.9$ is the Scherrer constant, λ is the neutron wavelength and LX is the Lorentzian coefficient obtained from the Rietveld refinement. This gave p ~127 Å compared with ~930 Å for the crystal structure.

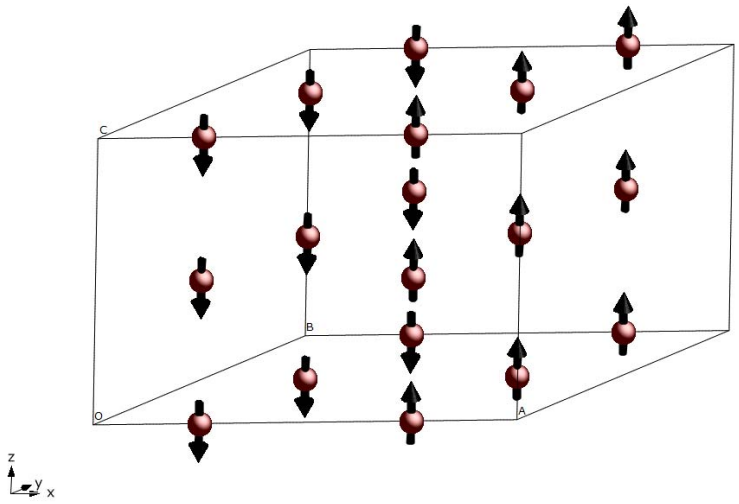

Figure 5.6 The antiferromagnetic arrangement of the Cr^{2+} moments in the *A*112'/*m* magnetic unit cell.

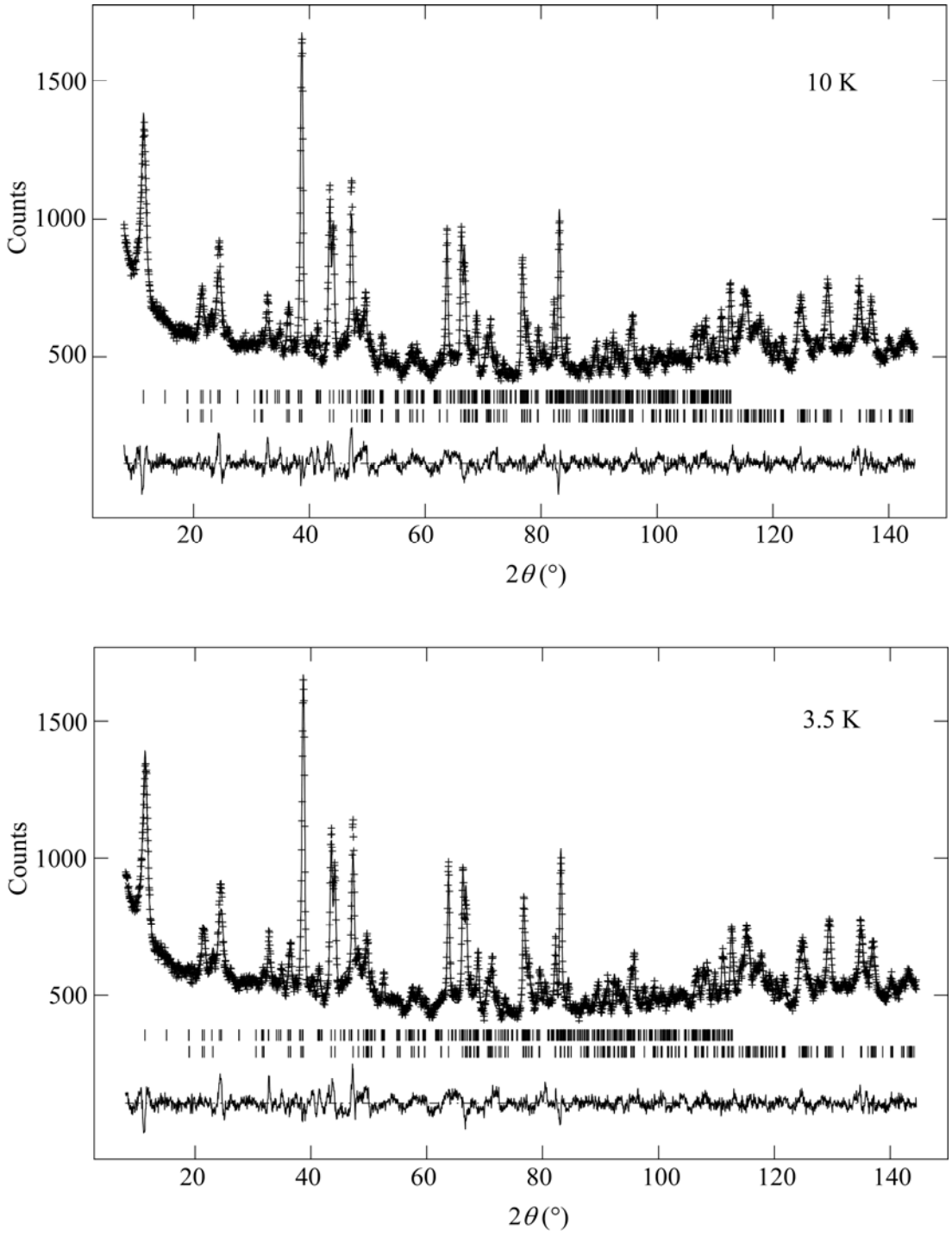

Figure 5.7 Observed calculated and difference plots for $KCrF_3$ at 10 (above) and 3.5 K (below) with the upper and lower reflection markers representing the magnetic and nuclear phase respectively.

Table 5.3

Refined crystallographic parameters and Rietveld reliability factors for $KCrF_3$ at 3.5 K.

3.5 K; Space group *I112/m*, with a = 5.8025(4) Å, b = 5.8115(4) Å, c = 8.5916(4) Å and γ = 93.726(4)°. The Cr magnetic moment = 4.39(7) μ_B.					
Atom	Site	x	y	z	$U_{iso}\times100$ (Å^2)
K	*4g*	0	0	0.249(1)	0.21(16)
Cr(1)	*2c*	0	0.5	0	0.06(13)
Cr(2)	*2d*	0	0.5	0.5	0.06(13)
F(1)	*4h*	0	0.5	0.232(1)	0.53(7)
F(2)	*4i*	0.283(2)	0.709(2)	0	0.53(7)
F(3)	*4i*	0.232(1)	0.190(1)	0	0.53(7)
Reliability factors: χ^2 = 2.23, R_{wp} = 3.85 %, R_p = 3.03 %, R_{F2} = 13.29 %					

Table 5.4

Refined crystallographic parameters and Rietveld reliability factors for $KCrF_3$ at 10 K.

10 K; Space group *I*112*/m*, with a = 5.8025(4) Å, b = 5.8121(4) Å, c = 8.5918(4) Å and γ = 93.725(4)°. The Cr magnetic moment = 4.39(8) μ_B.					
Atom	Site	x	y	z	$U_{iso}\times100$ (Å^2)
K	*4g*	0	0	0.249(1)	0.19(17)
Cr(1)	*2c*	0	0.5	0	0.07(13)
Cr(2)	*2d*	0	0	0.5	0.07(13)
F(1)	*4h*	0	0.5	0.2315(7)	0.50(8)
F(2)	*4i*	0.283(2)	0.710(2)	0	0.50(8)
F(3)	*4i*	0.232(1)	0.191(1)	0	0.50(8)
Reliability factors: χ^2 = 2.30, R_{wp} = 4.00 %, R_p = 3.15 %, R_{F2} = 14.27 %					

5.4 Discussion

This variable temperature neutron diffraction study confirms the basic structures and magnetic order model for $KCrF_3$. The presence of several magnetic peaks below T_C, indexing on a $2a \times b \times c$ supercell, provides evidence of long range magnetic order extending over ~127 Å domains. However, this value is small compared with ~930 Å for the crystal structure and this may be a result of site defects within the crystallites.

Figure 5.8 shows the variation of $KCrF_3$ lattice parameters with temperature. After the sharp reduction in the *a* and *b* parameters between 300 and 100 K due to the structural phase transition, there is only a slight gradual decrease on further cooling. The observed continuous increase of the *c*-axis is in accordance with the more pronounced octahedral tilting at lower temperature and there is an overall reduction in the unit cell volume between 100 and 3.5 K. Hence, the monoclinic structure remains stable throughout this temperature range and there is no indication of a re-entrant type phase transition below 30 K as has been previously suggested[19]. The bond lengths calculated from the 10 and 3.5 K data, listed in Table 5.5 and Table 5.6, show that the alternating long/short Cr-F bonds occur along the $[1\bar{1}0]$ and *c* directions and the orbital order motif found at 100 K is retained.

The magnetic properties are very similar to those of the weak ferromagnet $LaMnO_3$[24], and can be explained through the exchange interactions within and between the orbitally ordered planes. Superexchange interactions between the Cr ions across the Cr-O-Cr bond within the orbitally ordered planes lead to ferromagnetic exchange between adjacent Cr^{2+} spins. In turn, the long-range antiferromagnetic order observed below 46 K can be attributed to antiferromagnetic coupling between the ferromagnetic layers. The arrangement of the magnetic moments within the crystal structure is illustrated in Figure 5.9. The overall magnetic moment of 4.39(7) μ_B at 3.5 K is large (as is the moment for the *A*112/*m*' refinement at 4.83(8) μ_B). This may be an indication that the magnetic form factor for Cr^{2+} is underestimated. Magnetic susceptibility measurements[19] indicated the existence of weak ferromagnetism. It is thought that the Cr moments are canted in $KCrF_3$ due to either single-ion anisotropy effects and/or a Dzyaloshinsky-Morya interaction

between neighbouring Cr moments which is non-zero due to the small out of plane tilt of the $3d_{z^2}$ orbitals along the [110] stacking direction. However, a perpendicular ferromagnetic component cannot exist with the observed antiferromagnetic component in either of the two space groups used in this work (as it is not allowed by symmetry). Therefore, a classical canting of moments is not likely to be the cause of the weak ferromagnetism observed in the magnetic susceptibility measurements. An attempt was made to refine the data in different settings allowing for a component in the *xy* plane but this resulted in an unstable refinement.

Table 5.5

Selected bond distances and angles for $KCrF_3$ obtained from the refinement against 3.5 K data.

Bond	Length (Å)	Angle	Angle (˚)
Cr(1)-F(1) (×2)	1.994(6)	Cr(1)-F(1)-Cr(2)	180
Cr(1)-F(2) (×2)	1.977(12)	Cr(1)-F(2)-Cr(2)	162.0(3)
Cr(1)-F(3) (×2)	2.315(6)	Cr(1)-F(3)-Cr(2)	163.10(28)
Cr(2)-F(1) (×2)	2.302(6)	F(2)-Cr(1)-F(3)	88.73(21)
Cr(2)-F(2) (×2)	2.042(12)	F(2)-Cr(2)-F(3)	89.85(20)
Cr(2)-F(3) (×2)	1.968(6)		

Table 5.6

Selected bond distances and angles for $KCrF_3$ obtained from the refinement against 10 K data.

Bond	Length (Å)	Angle	Angle (˚)
Cr(1)-F(1) (×2)	1.989(6)	Cr(1)-F(1)-Cr(2)	180
Cr(1)-F(2) (×2)	1.982(12)	Cr(1)-F(2)-Cr(2)	162.07(27)
Cr(1)-F(3) (×2)	2.310(6)	Cr(1)-F(3)-Cr(2)	163.49(29)
Cr(2)-F(1) (×2)	2.307(6)	F(2)-Cr(1)-F(3)	88.60(22)
Cr(2)-F(2) (×2)	2.038(12)	F(2)-Cr(2)-F(3)	89.98(20)
Cr(2)-F(3) (×2)	1.972(6)		

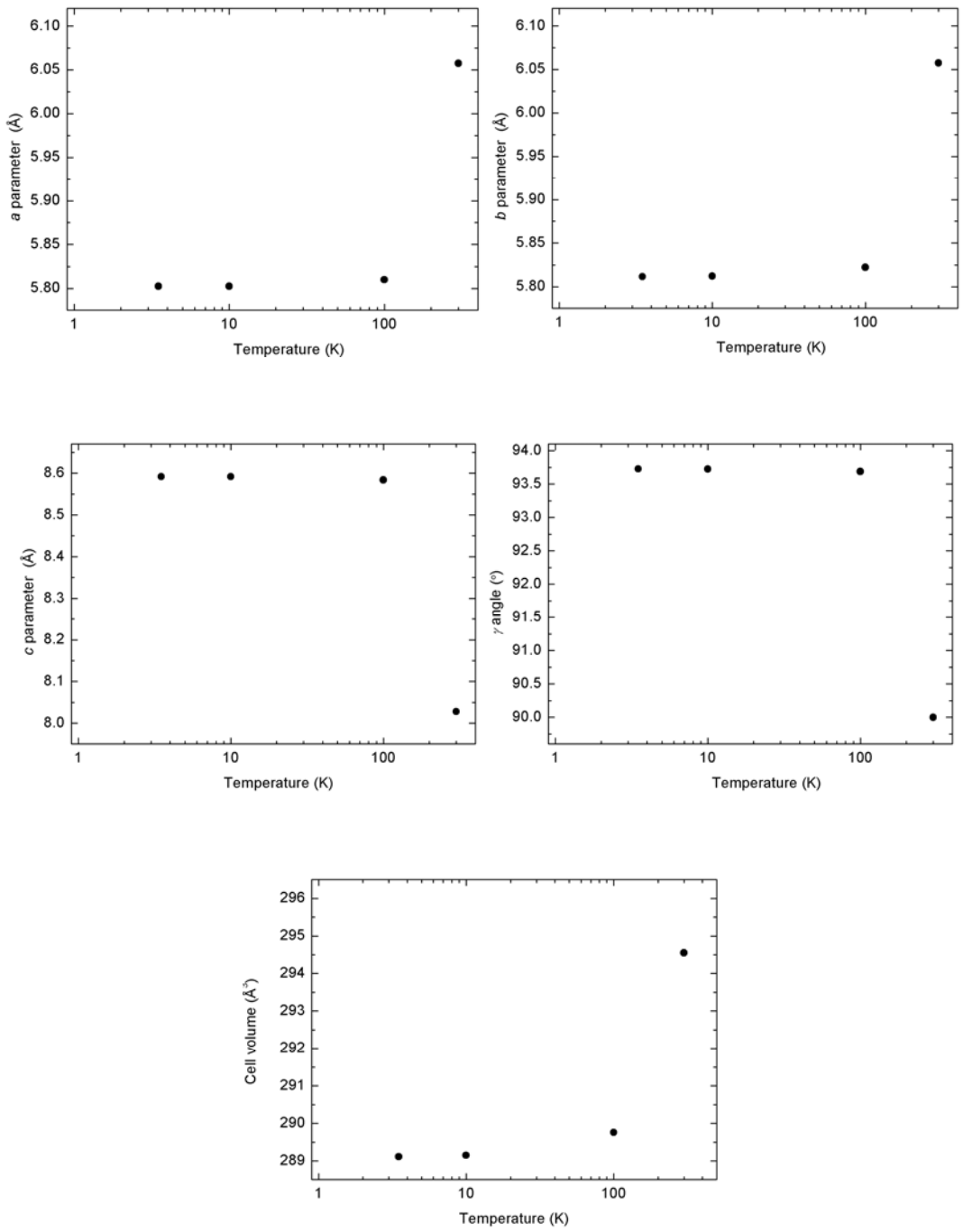

Figure 5.8 Plots showing the variation of the lattice parameters and unit cell volume of $KCrF_3$ with temperature.

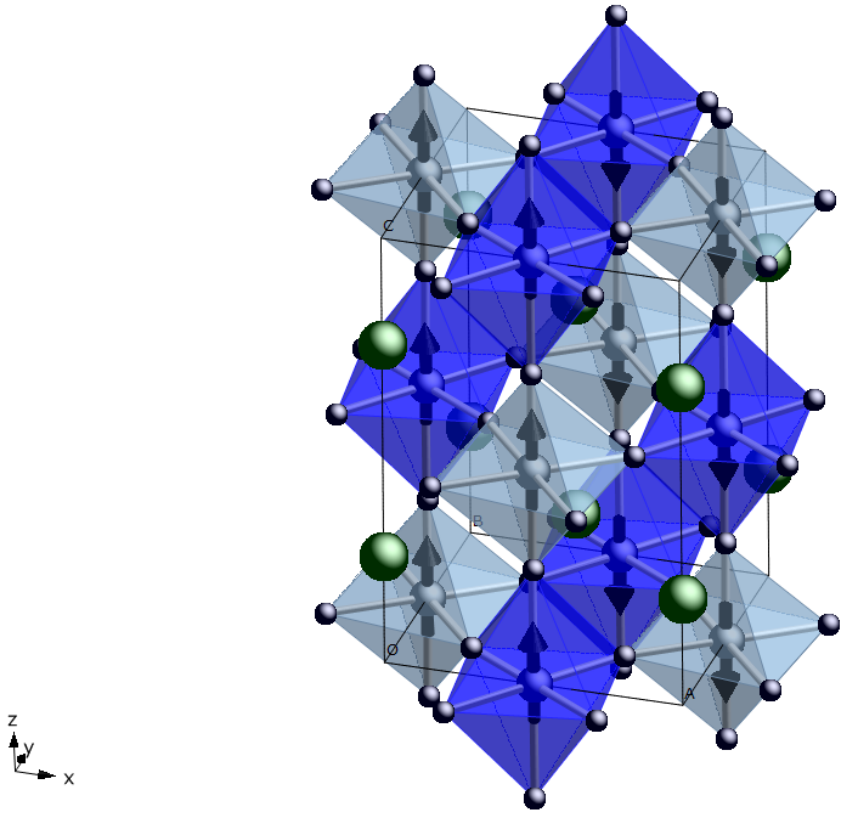

Figure 5.9 The crystal structure and ferromagnetic ordering of the Cr^{2+} spins within the orbitally ordered planes defined by the *c*-axis and the [1-10] direction at 3.5 K giving rise to an overall A-type antiferromagnetic order. Light and dark blue octahedra represent the two different chromium sites, Cr(1) and Cr(2).

5.5 Conclusions

In conclusion, the perovskite-type fluoride $KCrF_3$ is confirmed to undergo a phase transition below 250 K to a monoclinic structure with antiferrodistortive ordering of the $3d_z^2$ orbitals in the plane defined by the c-axis and $[1\bar{1}0]$ base diagonal. This structure and ordering pattern are retained down to 3.5 K. Below the magnetic ordering temperature of 46 K, these structural features gives rise to long range A-type antiferromagnetic order with an overall magnetic moment of 4.39(7) μ_B at 3.5 K.

5.6 References

1. A. Tressaud and J.M. Dance, *Struct. Bond.*, **52**, 87-146 (1982).
2. V. Scatturin, J. Hastings, L. Corliss and N. Elliott, *Acta Cryst.*, **14**, 19 (1961).
3. E.N. Maslen and N. Spadaccini, *Acta Cryst. B*, **45**, 45 (1989).
4. N. Kijima, K. Tanaka and F. Marumo, *Acta Cryst. B*, **39**, 557 (1983).
5. K. Knox, *Acta Cryst.*, **14**, 583 (1961).
6. N. Binggeli and M. Altarelli, *Phys. Rev. B*, **70**, 085117-10 (2004).
7. W.E. Pickett, *Rev. Mod. Phys.*, **61**, 433 (1989).
8. D.I. Khomskii and K.I. Kugel, *Solid State Com.*, **13**, 763-766 (1973).
9. S.E. McLain, M.R. Dolgos, D.A. Tennant, J.F.C. Turner, T. Barnes, T. Proffen, B.C. Sales and R.I. Bewley, *Nature Materials*, **5**, 561-566 (2006).
10. P. Schiffer, A.P. Ramirez, W. Bao and S.W. Cheong, *Phys. Rev. Lett.*, **75**, 3336 (1995).
11. Y. Murakami, J.P. Hill, D. Gibbs, M. Blume, I. Koyama, M. Tanaka, H. Kawata, T. Arima, Y. Tokura, K. Hirota and Y. Endoh, *Phys. Rev. Lett.*, **81**, 582 (1998).
12. A.J. Edwards and R.D. Peacock, *J. Chem. Soc.*, 4126-4127 (1959).
13. R. Hoppe, *Angew. Chem.*, **71**, 457 (1959).
14. R.H. Buttner, E.N. Maslen and N. Spadaccini, *Acta Cryst. B*, **46**, 131-138 (1990).
15. M.T. Hutchings, E.J. Samuelsen, G. Shirane and K. Hirakawa, *Phys. Rev.*, **188**, 919 (1969).
16. S. Margadonna and G. Karotsis, *J. Mat. Chem.*, **17**, 2013-2020 (2007).
17. J.B. Goodenough, *Phys. Rev.*, **100**, 564 (1955).
18. V. Kaiser, M. Otto, F. Binder and D. Babel, *Anorg. Allg. Chem.*, **585**, 93-104 (1990).
19. S. Margadonna and G. Karotsis, *J. Am. Chem. Soc.*, **128**, 16436-16437 (2006).
20. H.M. Rietveld, *J. Appl. Cryst.*, **2**, 65 (1969).
21. A.C. Larson and R.B.V. Dreele, *General Structural Analysis System (GSAS)*; Los Alamos National Laboratory: Los Alamos, 2000.

22. P. Karen and P.M. Woodward, *J. Solid State Chem.*, **141**, 78 (1998).

23. A.C. Larson and R.B.V. Dreele, *GSAS Manual*; Los Alamos National Laboratory: Los Alamos, 1994.

24. V. Skumryev, F. Ott, J.M.D. Coey, A. Anane, J.P. Renard, L. Pinsard-Gaudart and A. Revcolevschi, *Eur. Phys. J. B*, **11**, 401-406 (1999).

Chapter 6

Conclusions

The physical properties of materials are intimately linked with the structure and interatomic distances. Applying pressure can cause considerable variation of these distances and it therefore provides a very powerful tool of examining the relationship between structure and properties. In combination with neutron and X-ray diffraction, high pressure can be used to examine subtle lattice distortions such as those observed in charge ordered materials. This is exemplified in this research firstly by the investigation of the changes in valence state of $BiNiO_3$ under pressure using powder neutron diffraction. At ambient pressure, the structure is triclinic and highly distorted, with the unusual charge distribution $Bi^{3+}_{0.5}Bi^{5+}_{0.5}Ni^{2+}O_3$ and ordering of the Bi charges on the A-site. A phase transition occurs between 3-4 GPa to a higher symmetry, orthorhombic structure with one distinct Bi and Ni site. Bond valence sum calculations based on the Bi-O and Ni-O bond distances, shows that a pressure-induced melting of the charge ordered state has taken place through a simultaneous charge transfer from Ni to Bi, leading to the formation of a metallic $Bi^{3+}Ni^{3+}O_3$ phase.

Secondly, synchrotron X-ray diffraction has been used to examine the structural stability of $(EDT\text{-}TTF\text{-}CONH_2)_6[Re_6Se_8(CN)_6]$ under pressure. At ambient conditions the structure is made up from equivalent dimers in a Kagome type pattern with 4 holes shared between them promoting metallic behaviour. Between 0.4-0.8 GPa a phase transition occurs to a lower symmetry triclinic phase leading to the formation of three inequivalent dimers A, B and C in the structure. Differences in the intradimer angle and distances reveals that a sliding motion within dimer B means that it has become more eclipsed, caused by the localisation of the extra hole. Hence, this suggests the two dimensional Kagome symmetry is broken that high pressure induces a charge ordered insulating state similar to that observed at low temperature.

High pressure resistivity measurements will be required to confirm the changes in the physical properties and if a pressure-induced metal to insulator transition occurs. Further high pressure structural studies would be useful to pinpoint the pressure at which the phase transition occurs and, if better quality data can be acquired, the structural properties can be studied in more detail.

The structural properties of materials are also affected by changes in temperature and variable temperature neutron powder diffraction can be used to study charge, orbital and magnetic ordering in crystalline compounds. This technique was utilised to determine the charge and magnetic ordering in $BiNiO_3$. The antiferromagnetic ordering observed in $BiNiO_3$ below 300 K was found to be of the G-type with antiferromagnetic interactions between all neighbouring Ni^{2+} moments. Although $BiNiO_3$ is in fact ferromagnetic, neutron diffraction is not sensitive enough to detect the inexact cancellation of opposing inequivalent moments in the low symmetry cell. No structural phase transitions were observed on cooling and bond valence sum calculations confirmed that the $Bi^{3+}_{0.5}Bi^{5+}_{0.5}Ni^{3+}O_3$ charge distribution remains down to 5 K. Additional neutron diffraction studies of $BiNiO_3$ at high pressure in combination with both high and low temperature are currently being carried out in order to establish a complete picture of the phase diagram.

Furthermore, the orbital and magnetic ordering of $KCrF_3$ has been investigated using the same technique. Changes in the Cr-F distances with temperature shows that the Jahn-Teller distortions observed at ambient conditions remains below the phase transition at 250 K, and the antiferrodistortive orbital ordering pattern of the $3d_z^2$ orbitals is retained down to 3.5 K. However, below the transition temperature, the OO shifts from appearing in the *ab* plane to the plane defined by the *c*-axis and the $[1\bar{1}0]$ base diagonal. There was no indication of any phase transition in the temperature range 3.5-200 K. The long range antiferromagnetic order found below 46 K is of the A-type with ferromagnetic interactions between the Cr moments via superexchange within the orbitally ordered planes and antiferromagnetic coupling between the planes. The results also indicate that the weak ferromagnetism observed in the magnetic susceptibility measurements is not likely to be caused by a classical canting of moments. Single-crystal

measurements would be required to get a more exact picture of the direction of the moments. It would be interesting to investigate the effect of high pressure on the structural and physical properties of $KCrF_3$. Application of high pressure may induce phase transitions similar to those seen with changes in temperature or lead to the formation of new and different structures.

Appendix A

Supplementary material for Chapter 3: Rietveld refinement results for $BiNiO_3$

Crystallographic parameters and Rietveld reliability factors for $BiNiO_3$ at 2.1 GPa and 300 K.

Space group *P-1*, with a = 5.3614(4) Å, b = 5.6274(4) Å, c = 7.6562(5) Å, α = 91.972(6)°, β = 89.755(5)° and γ = 91.249(5)°

Atom	Site	x	y	z	$U_{iso}\times100$ (Å^2)
Bi1	2i	0.0028(13)	0.0458(9)	0.2343(7)	0.355(85)
Bi2	2i	0.5139(13)	0.4431(10)	0.7232(8)	0.355(85)
Ni1	1d	0.5	0	0	0.243(48)
Ni2	1c	0	0.5	0	0.243(48)
Ni3	1f	0.5	0	0.5	0.243(48)
Ni4	1g	0	0.5	0.5	0.243(48)
O1	2i	-0.1360(17)	0.4739(15)	0.2549(13)	0.290(54)
O2	2i	0.3898(17)	0.0787(15)	0.7584(11)	0.290(54)
O3	2i	0.8361(18)	0.1765(15)	-0.0332(11)	0.290(54)
O4	2i	0.3213(18)	0.3274(14)	0.0821(12)	0.290(54)
O5	2i	0.2147(17)	0.7681(17)	0.4133(12)	0.290(54)
O6	2i	0.6639(18)	0.6808(15)	0.5454(11)	0.290(54)

Reliability factors: χ^2 = 2.01, R_{wp} = 2.23 %, R_p = 3.86 %, R_{F2} = 3.74 %

Crystallographic parameters and Rietveld reliability factors for $BiNiO_3$ at 4.7 GPa and 300 K.

Space group *Pbnm*, with a = 5.3037(3) Å, b = 5.4774(3) Å and c = 7.5879(4) Å					
Atom	Site	x	y	z	U_{iso} ×100 (Å^2)
Bi1	4c	-0.0070(8)	0.05085(33)	0.25	0.47(4)
Ni1	4b	0	0.5	0	0.17(4)
O1	8d	0.6974(5)	0.2988(5)	0.0379(4)	0.42(3)
O2	4c	0.0878(7)	0.4778(7)	0.25	0.41(3)
Reliability factors: χ^2 = 2.251, R_{wp} = 2.37 %, R_p = 4.0 %, R_{F2} = 5.29 %					

Crystallographic parameters and Rietveld reliability factors for $BiNiO_3$ at 6.1 GPa and 300 K.

Space group *Pbnm*, with a = 5.2942(3) Å, b = 5.4557(4) Å and c = 7.5709(5) Å					
Atom	Site	x	y	z	U_{iso} ×100 (Å^2)
Bi1	4c	-0.0070(9)	0.0497(4)	0.25	0.529(50)
Ni1	4b	0	0.5	0	0.143(38)
O1	8d	0.6980(5)	0.2977(5)	0.0378(4)	0.469(37)
O2	4c	0.08363(8)	0.4786(8)	0.25	0.450(37)
Reliability factors: χ^2 = 2.183, R_{wp} = 2.6 %, R_p = 4.19 %, R_{F2} = 5.98 %					

Calculated bond distances and angles for $BiNiO_3$ at 2.1 GPa and 300 K

Distances (Å)					
Bond	Length	Bond	Length	Bond	Length
Bi1-O1	3.326	Bi2-O1	2.086	Ni1-O2 (x2)	2.011
Bi1-O1	2.561	Bi2-O1	3.371	Ni1-O3 (x2)	2.064
Bi1-O2	2.237	Bi2-O2	2.162	Ni1-O4 (x2)	2.178
Bi1-O2	3.366	Bi2-O2	3.655	Ni2-O1 (x2)	2.089
Bi1-O3	2.365	Bi2-O3	3.017	Ni2-O3 (x2)	2.005
Bi1-O3	2.165	Bi2-O3	3.686	Ni2-O4 (x2)	2.086
Bi1-O4	2.586	Bi2-O4	3.017	Ni3-O2 (x2)	2.101
Bi1-O4	3.603	Bi2-O4	2.135	Ni3-O5 (x2)	2.088
Bi1-O5	2.456	Bi2-O5	3.454	Ni3-O6 (x2)	2.059
Bi1-O5	3.16	Bi2-O5	2.151	Ni4-O1 (x2)	2.024
Bi1-O6	3.684	Bi2-O6	2.083	Ni4-O5 (x2)	2.008
Bi1-O6	2.864	Bi2-O6	2.335	Ni4-O6 (x2)	2.107
Average	*2.84*	*Average*	*2.76*	*Average*	*2.07*
Angles (˚)					
Bond	Angle	Bond	Angle	Bond	Angle
O2-Ni1-O3	91.5(4)	O2-Ni3-O5	101.9(4)	Ni2-O1-Ni4	137.7(5)
O2-Ni1-O4	94.8(4)	O2-Ni3-O6	97.1(3)	Ni1-O2-Ni3	137.4(5)
O3-Ni1-O4	91.4(3)	O5-Ni3-O6	99.4(3)	Ni1-O3-Ni2	141.6(5)
O1-Ni2-O3	96.7(4)	O1-Ni4-O5	96.7(4)	Ni1-O4-Ni2	133.7(4)
O1-Ni2-O4	92.4(4)	O1-Ni4-O6	92.4(4)	Ni3-O5-Ni4	139.9(5)
O3-Ni2-O4	92.3(3)	O5-Ni4-O6	99.31(3)	Ni3-O6-Ni4	141.0(5)

Calculated bond distances and angles for $BiNiO_3$ at 4.7 GPa and 300 K

Distances (Å)					
Bond	Length	Bond	Length	Bond	Length
Bi1-O3 (×2)	2.624	Bi1-O4	3.1733	Ni1-O1 (×2)	1.968
Bi1-O3 (×2)	2.3469	Bi1-O4	2.3953	Ni1-O1 (×2)	1.9643
Bi1-O3 (×2)	2.578	Bi1-O4	3.103	Ni1-O2 (×2)	1.95599
Bi1-O3 (×2)	3.336	Bi1-O4	2.261		
		Average	*2.73*	*Average*	*1.96*
Angles (°)					
Bond		Angle		Bond	Angle
Ni1-O1-Ni1		151.7(1)		Ni1-O2-Ni1	152.5(2)

Calculated bond distances and angles for $BiNiO_3$ at 6.1 GPa and 300 K

Distances (Å)					
Bond	Length	Bond	Length	Bond	Length
Bi1-O3 (×2)	2.614	Bi1-O4	3.154	Ni1-O1 (×2)	1.9664
Bi1-O3 (×2)	2.347	Bi1-O4	2.393	Ni1-O1 (×2)	1.9505
Bi1-O3 (×2)	2.575	Bi1-O4	3.093	Ni1-O2 (×2)	1.951
Bi1-O3 (×2)	3.317	Bi1-O4	2.258		
		Average	2.72	*Average*	1.96
Angles (°)					
Bond		Angle		Bond	Angle
Ni1-O1-Ni1		152.0(2)		Ni1-O2-Ni1	152.0(3)

Atomic parameters for $BiNiO_3$ from the Rietveld fit to 200 K neutron powder diffraction data.

Atom	Site	*x*	*y*	*z*	$U_{iso} \times 100$ (Å^2)
Bi1	2i	0.0066(6)	0.0497(4)	0.2308(4)	0.238(80)
Bi2	2i	0.5104(6)	0.4431(5)	0.7236(4)	0.238(80)
Ni1	1d	0.5	0	0	0.748(60)
Ni2	1c	0	0.5	0	0.748(60)
Ni3	1f	0.5	0	0.5	0.748(60)
Ni4	1g	0	0.5	0.5	0.748(60)
O1	2i	-0.1397(9)	0.4718(8)	0.2521(6)	0.487(60)
O2	2i	0.3957(9)	0.077(7)	0.7572(6)	0.487(60)
O3	2i	0.8337(8)	0.175(7)	-0.0323(6)	0.487(60)
O4	2i	0.3163(8)	0.3343(7)	0.0832(6)	0.487(60)
O5	2i	0.2128(9)	0.7704(8)	0.412(6)	0.487(60)
O6	2i	0.6742(8)	0.6867(7)	0.5464(6)	0.487(60)

Atomic parameters for $BiNiO_3$ from the Rietveld fit to 100 K neutron powder diffraction data.

Atom	Site	*x*	*y*	*z*	$U_{iso} \times 100$ (Å^2)
Bi1	2i	0.0063(6)	0.051(5)	0.2305(4)	0.104(80)
Bi2	2i	0.5105(6)	0.4434(5)	0.7227(4)	0.104(80)
Ni1	1d	0.5	0	0	0.561(60)
Ni2	1c	0	0.5	0	0.561(60)
Ni3	1f	0.5	0	0.5	0.561(60)
Ni4	1g	0	0.5	0.5	0.561(60)
O1	2i	-0.1398(9)	0.4712(8)	0.2521(6)	0.354(60)
O2	2i	0.3957(9)	0.0773(7)	0.7568(6)	0.354(60)
O3	2i	0.8336(8)	0.1749(7)	-0.0315(6)	0.354(60)
O4	2i	0.317(8)	0.334(7)	0.0836(6)	0.354(60)
O5	2i	0.2133(9)	0.7704(8)	0.4108(6)	0.354(60)
O6	2i	0.6732(8)	0.686(7)	0.5464(6)	0.354(60)

Appendix B

Supplementary material for Chapter 4: Refinement results for $(EDT\text{-}TTF\text{-}CONH_2)_6[Re_6Se_8(CN)_6]$

Parameters	**0.4 GPa**	**0.8 GPa**	**1.2 GPa**
Chemical formula	$C_{60}H_{42}N_{12}O_6Re_6S_{36}Se_8$	$C_{60}H_{30}N_{12}O_6Re_6S_{36}Se_8$	
M_r	3930.17	3918.23	3918.23
Cell setting, Space group	Rhombohedral, $R\bar{3}$	Triclinic, $P\bar{1}$	
a (Å)	14.8819(1)	14.606(10	14.585(1)
b (Å)	-	14.663(1)	14.602(1)
c (Å)	-	14.789(2)	14.805(2)
α (°)	61.078(1)	90.81(1)	90.87(1)
β (°)	-	119.15(1)	119.08(1)
γ (°)	-	118.971(6)	118.94(7)
V (Å^3)	2387.12(4)	2280.4(6)	2278.4(7)
Z	1		
D_x (mg m^{-3})	2.734	2.853	2.856
Radiation type	Mo $K\alpha$		
No. of reflections for cell parameters	4291	2546	2172
θ range (°)	4–25	3-26	
μ (mm^{-1})	*11.47*	12.01	12.02
Temperature (K)	295		
Crystal form, colour	Prism, black		
Crystal size (mm)	0.1x0.1x0.1		
Data collection			
Diffractometer	Bruker SMART		
Data collection method	ω scans		
Absorption correction	multi-scan SADABS (Siemens, 1996)		
No. of measured, independent and observed reflections	8643, 1919, 1550	8627, 1925, 1572	8699, 2737, 1618
Criterion for observed reflections	$I > 2.00\sigma(I)$		
R_{int}	*0*	0.093	0.079
θ_{max} (°)	*25*	26	
Range of *h, k, l*	$h = -6\rightarrow14$ $k = -5\rightarrow15$ $l = 2\rightarrow18$	$h = -18\rightarrow18$ $k = -19\rightarrow18$ l = -9→10	$h = -18\rightarrow18$ $k = -18\rightarrow19$ l = -9→9
Refinement			
Refinement on	F^2		
$R[F^2 > 2\sigma(F^2)]$, $wR(F^2)$, S	0.063, 0.197, 0.95	0.128, 0.143, 1.03	0.122, 0.330,1.09
No. of reflections	1891	1898	2766
No. of parameters	193	193	257
H-atom treatment	Riding independent and constrained refinement		
Weighting scheme	$w = 1/[\sigma^2(F^2) + (0.08P)^2 + P]$ $P = (\max(F_o^2,0) + 2F_c^2)/3$	$w = 1/[\sigma^2(F^2) + (0.2P)^2 + P]$ $P = (\max(F_o^2,0) + 2F_c^2)/3$	
$(\Delta/\sigma)_{max}$	0.0003	0.022	0.039
$\Delta\rho_{max}$, $\Delta\rho_{min}$ (e Å^{-3})	2.04, -2.21	5.19, -3.14	4.70, -4.42

Fractional atomic coordinates and isotropic or equivalent isotropic displacement parameters (Å^2) for (EDT-TTF-CONH$_2$)$_6$[Re$_6$Se$_8$(CN)$_6$]at 0 GPa.

Atom	*x*	*y*	*z*	*U*iso*/*U*eq
S1	0.5300 (7)	0.7163 (6)	0.9010 (6)	0.0464
S2	0.7063 (6)	0.5344 (6)	0.9669 (6)	0.0454
S3	0.5005 (6)	0.5771 (5)	0.8113 (6)	0.0416
S4	0.6748 (6)	0.3929 (6)	0.8849 (6)	0.0406
S5	0.5242 (9)	0.8541 (7)	0.9910 (9)	0.0731
S6	0.7478 (9)	0.6425 (9)	1.0566 (9)	0.0828
C2	0.610 (2)	0.586 (2)	0.9063 (19)	0.0319
C3	0.601 (2)	0.5251 (19)	0.8688 (17)	0.0274
C4	0.586 (3)	0.731 (2)	0.972 (3)	0.0489
C5	0.673 (3)	0.649 (3)	0.993 (3)	0.0573
C6	0.536 (2)	0.458 (2)	0.792 (2)	0.0341
C7	0.613 (2)	0.375 (2)	0.827 (2)	0.0388
C8	0.603 (3)	0.851 (3)	1.052 (3)	0.0908
C1	0.475 (2)	0.446 (2)	0.745 (2)	0.0381
O1	0.5102 (16)	0.3687 (16)	0.7179 (19)	0.0553
N2	0.3913 (18)	0.5274 (19)	0.7220 (17)	0.0391
Re1	1.10813 (7)	0.06285 (7)	0.91748 (7)	0.0227
Se1	1.24210 (19)	−0.1207 (2)	0.96446 (19)	0.0275
Se2	1.08474 (9)	0.08474 (9)	1.08474 (9)	0.0310
C11	1.2299 (19)	0.131 (2)	0.823 (2)	0.0312
N11	1.3035 (19)	0.1687 (19)	0.7646 (18)	0.0464
C9	0.719 (3)	0.7832 (16)	1.017 (4)	0.1018
H71	0.6326	0.3090	0.8198	0.0489*
H81	0.5732	0.8234	1.1295	0.1200*
H82	0.6003	0.9242	1.0308	0.1200*
H91	0.7468	0.8090	0.9395	0.1350*
H92	0.7570	0.7929	1.0471	0.1350*
H21	0.3504	0.5233	0.6916	0.0473*
H22	0.3703	0.5941	0.7329	0.0473*

Atomic displacement parameters (Å^2) for (EDT-TTF-CONH$_2$)$_6$[Re$_6$Se$_8$(CN)$_6$] at 0 GPa.

Atom	*U*11	*U*22	*U*33	*U*12	*U*13	*U*23
S1	0.064 (5)	0.035 (3)	0.051 (4)	−0.011 (3)	−0.033 (4)	−0.013 (4)
S2	0.047 (4)	0.049 (4)	0.055 (4)	−0.014 (3)	−0.026 (4)	−0.020 (4)
S3	0.054 (4)	0.032 (3)	0.056 (4)	−0.009 (3)	−0.034 (4)	−0.014 (4)
S4	0.040 (4)	0.034 (3)	0.053 (4)	−0.008 (3)	−0.023 (4)	−0.014 (4)
S5	0.099 (7)	0.055 (5)	0.088 (7)	−0.013 (5)	−0.042 (6)	−0.039 (5)
S6	0.092 (7)	0.093 (7)	0.115 (8)	−0.027 (6)	−0.063 (6)	−0.045 (6)
C2	0.039 (10)	0.035 (7)	0.025 (10)	−0.017 (6)	−0.010 (8)	−0.007 (9)
C3	0.045 (10)	0.022 (6)	0.015 (9)	−0.023 (6)	−0.013 (8)	0.010 (8)
C4	0.061 (12)	0.042 (8)	0.062 (14)	−0.020 (6)	−0.028 (10)	−0.019 (11)
C5	0.069 (13)	0.061 (9)	0.070 (14)	−0.010 (7)	−0.040 (11)	−0.034 (12)
C6	0.040 (11)	0.032 (7)	0.036 (12)	−0.012 (7)	−0.015 (9)	−0.012 (10)
C7	0.036 (11)	0.035 (7)	0.051 (14)	−0.007 (7)	−0.016 (10)	−0.020 (11)
C8	0.123 (16)	0.085 (13)	0.11 (2)	−0.039 (10)	−0.047 (15)	−0.054 (15)
C1	0.046 (12)	0.041 (10)	0.037 (13)	−0.010 (8)	−0.017 (11)	−0.021 (11)
O1	0.050 (11)	0.056 (11)	0.085 (16)	−0.013 (9)	−0.021 (12)	−0.046 (12)
N2	0.040 (11)	0.051 (12)	0.030 (11)	−0.009 (8)	−0.011 (10)	−0.022 (12)
Re1	0.0223 (6)	0.0233 (6)	0.0240 (6)	−0.0096 (4)	−0.0068 (4)	−0.0071 (4)
Se1	0.0213 (11)	0.0305 (12)	0.0302 (13)	−0.0057 (9)	−0.0091 (9)	−0.0114 (11)
Se2	0.0346 (13)	0.0346 (13)	0.0346 (13)	−0.0137 (8)	−0.0137 (8)	−0.0137 (8)
C11	0.028 (4)	0.037 (5)	0.034 (5)	−0.019 (4)	−0.010 (5)	−0.007 (6)
N11	0.050 (14)	0.042 (14)	0.037 (13)	−0.035 (12)	−0.008 (11)	0.008 (12)
C9	0.111 (13)	0.102 (8)	0.15 (2)	−0.046 (13)	−0.053 (17)	−0.059 (14)

Calculated distances and angles for (EDT-TTF-CONH$_2$)$_6$[Re$_6$Se$_8$(CN)$_6$] at 0 GPa.

Distances (Å)					
S1—C2	1.72 (3)	C2—C3	1.37 (3)	Re1—Se1i	2.524 (2)
S1—C4	1.77 (2)	C4—C5	1.34 (4)	Re1—Se1ii	2.523 (3)
S2—C2	1.73 (2)	C6—C7	1.32 (4)	Re1—Re1ii	2.6430 (16)
S2—C5	1.73 (3)	C6—C1	1.50 (3)	Re1—Re1iii	2.6430 (16)
S3—C3	1.77 (2)	C7—H71	0.931	Re1—Re1i	2.6314 (13)
S3—C6	1.73 (2)	C8—C9	1.509 (18)	Re1—Re1iv	2.6314 (13)
S4—C3	1.71 (2)	C8—H81	0.969	Re1—Se1	2.513 (3)
S4—C7	1.71 (2)	C8—H82	0.969	Re1—Se2	2.522 (3)

S5—C4	1.73 (3)	C1—O1	1.20 (3)	Re1—C11	2.08 (2)
S5—C8	1.784 (16)	C1—N2	1.32 (3)	C11—N11	1.22 (3)
S6—C5	1.73 (3)	N2—H21	0.957	C9—H91	0.970
S6—C9	1.780 (17)	N2—H22	0.966	C9—H92	0.970
		Angles (°)			
C2—S1—C4	96.1 (12)	C9—C8—H82	108.5	Se1i—Re1—Se2	175.93 (8)
C2—S2—C5	96.1 (13)	H81—C8—H82	109.7	Se1ii—Re1—Se2	89.46 (6)
C3—S3—C6	93.1 (11)	C6—C1—O1	120 (3)	Re1ii—Re1—Se2	58.40 (4)
C3—S4—C7	95.3 (12)	C6—C1—N2	118 (2)	Re1iii—Re1—Se2	58.40 (4)
C4—S5—C8	103.6 (15)	O1—C1—N2	121 (2)	Re1i—Re1—Se2	118.25 (5)
C5—S6—C9	96.9 (16)	C1—N2—H21	121.1	Se1i—Re1—C11	90.8 (6)
S2—C2—S1	114.6 (12)	C1—N2—H22	121.3	Se1ii—Re1—C11	92.4 (7)
S2—C2—C3	120.7 (20)	H21—N2—H22	117.6	Re1ii—Re1—C11	136.3 (7)
S1—C2—C3	124.7 (19)	Se1i—Re1—Se1ii	90.21 (6)	Re1iii—Re1—C11	135.5 (7)
S3—C3—C2	120.4 (19)	Se1i—Re1—Re1ii	118.16 (6)	Re1i—Re1—C11	134.4 (7)
S3—C3—S4	115.5 (11)	Se1ii—Re1—Re1ii	58.17 (7)	Re1iv—Re1—Se1	58.69 (5)
C2—C3—S4	123.8 (18)	Se1i—Re1—Re1iii	118.39 (6)	Re1iv—Re1—Se2	118.25 (5)
S1—C4—S5	113.2 (17)	Se1ii—Re1—Re1iii	118.17 (7)	Se1—Re1—Se2	89.67 (6)
S1—C4—C5	115.3 (20)	Re1ii—Re1—Re1iii	60.000	Re1iv—Re1—C11	133.7 (7)
S5—C4—C5	131.3 (20)	Se1i—Re1—Re1i	58.32 (6)	Se1—Re1—C11	91.1 (7)
S6—C5—S2	116.5 (19)	Se1ii—Re1—Re1i	58.59 (5)	Se2—Re1—C11	93.2 (6)
S6—C5—C4	126 (2)	Re1ii—Re1—Re1i	59.85 (2)	Re1iv—Se1—Re1iii	62.86 (6)
S2—C5—C4	117.3 (19)	Re1iii—Re1—Re1i	90.000	Re1iv—Se1—Re1	62.99 (6)
S3—C6—C7	118.6 (17)	Se1i—Re1—Re1iv	58.55 (6)	Re1iii—Se1—Re1	63.31 (7)
S3—C6—C1	121.6 (20)	Se1ii—Re1—Re1iv	118.86 (6)	Re1iii—Se2—Re1	63.19 (8)
C7—C6—C1	120 (2)	Re1ii—Re1—Re1iv	90.000	Re1iii—Se2—Re1ii	63.19 (8)
S4—C7—C6	117.4 (19)	Re1iii—Re1—Re1iv	59.85 (2)	Re1—Se2—Re1ii	63.19 (8)
S4—C7—H71	121.5	Re1i—Re1—Re1iv	60.29 (4)	Re1—C11—N11	177 (2)
C6—C7—H71	121.1	Se1i—Re1—Se1	90.42 (6)	C8—C9—S6	118 (2)
S5—C8—C9	113 (2)	Se1ii—Re1—Se1	176.40 (7)	C8—C9—H91	108.3
S5—C8—H81	109.7	Re1ii—Re1—Se1	118.51 (7)	S6—C9—H91	107.0
C9—C8—H81	108.7	Re1iii—Re1—Se1	58.52 (7)	C8—C9—H92	107.1
S5—C8—H82	107.6	Re1i—Re1—Se1	118.97 (6)	S6—C9—H92	106.8

Fractional atomic coordinates and isotropic or equivalent isotropic displacement parameters (Å^2) for (EDT-TTF-CONH$_2$)$_6$[Re$_6$Se$_8$(CN)$_6$]at 0.4 GPa.

Atom	*x*	*y*	*z*	*U*iso*/*U*eq
S1	0.2807 (5)	0.4659 (5)	0.1027 (5)	0.0463
S2	0.4682 (5)	0.2920 (5)	0.0300 (5)	0.0437
S3	0.4204 (4)	0.4965 (5)	0.1929 (5)	0.0429
S4	0.6096 (5)	0.3246 (5)	0.1115 (5)	0.0423
S5	0.1443 (5)	0.4739 (7)	0.0076 (7)	0.0738
S6	0.3613 (6)	0.2508 (7)	−0.0618 (7)	0.0810
C2	0.4136 (16)	0.3883 (17)	0.0922 (15)	0.0320
C3	0.4742 (16)	0.4004 (16)	0.1298 (17)	0.0327
C4	0.2703 (18)	0.411 (2)	0.028 (2)	0.0498
C5	0.355 (2)	0.324 (2)	0.005 (2)	0.0590
C6	0.5463 (16)	0.4652 (15)	0.2043 (16)	0.0310
C7	0.6271 (17)	0.3912 (18)	0.167 (2)	0.0433
C1	0.5530 (18)	0.5235 (16)	0.2587 (17)	0.0346
O1	0.6377 (13)	0.4869 (12)	0.2794 (15)	0.0527
N2	0.4704 (15)	0.6085 (16)	0.2816 (16)	0.0470
Re1	0.93588 (6)	−0.10867 (6)	0.08399 (6)	0.0234
Se1	1.12111 (16)	−0.24542 (16)	0.03779 (16)	0.0287
Se2	0.91493 (7)	−0.08507 (7)	−0.08507 (7)	0.0315
C11	0.8636 (16)	−0.2295 (15)	0.1790 (15)	0.0277
N11	0.8278 (15)	−0.3033 (14)	0.2366 (15)	0.0418
C8	0.146 (2)	0.388 (2)	−0.046 (3)	0.0906
C9	0.2198 (15)	0.272 (2)	−0.016 (3)	0.0995
H71	0.6980	0.3752	0.1652	0.0489*
H81	0.1755	0.4177	−0.1263	0.1280*
H82	0.0746	0.3893	−0.0249	0.1280*
H91	0.1954	0.2424	0.0648	0.1370*
H92	0.2093	0.2305	−0.0419	0.1370*
H21	0.4746	0.6475	0.3144	0.0576*
H22	0.4063	0.6320	0.2660	0.0576*

Atomic displacement parameters (Å^2) for (EDT-TTF-CONH$_2$)$_6$[Re$_6$Se$_8$(CN)$_6$] at 0.4 GPa.

Atom	*U*11	*U*22	*U*33	*U*12	*U*13	*U*23
S1	0.036 (3)	0.058 (4)	0.051 (4)	−0.005 (3)	−0.017 (3)	−0.029 (3)
S2	0.041 (3)	0.047 (3)	0.052 (4)	−0.013 (3)	−0.014 (3)	−0.025 (3)
S3	0.032 (3)	0.054 (3)	0.056 (4)	−0.010 (3)	−0.015 (3)	−0.030 (3)
S4	0.035 (3)	0.039 (3)	0.058 (4)	−0.006 (2)	−0.019 (3)	−0.023 (3)
S5	0.044 (3)	0.113 (6)	0.086 (6)	−0.012 (4)	−0.028 (4)	−0.055 (5)
S6	0.075 (5)	0.107 (6)	0.108 (6)	−0.028 (5)	−0.028 (5)	−0.070 (5)
C2	0.033 (6)	0.039 (9)	0.021 (9)	−0.012 (5)	−0.008 (8)	−0.009 (7)
C3	0.029 (5)	0.035 (9)	0.034 (10)	−0.016 (5)	−0.006 (8)	−0.010 (7)
C4	0.035 (7)	0.073 (11)	0.054 (12)	−0.016 (6)	−0.012 (9)	−0.033 (9)
C5	0.050 (8)	0.086 (12)	0.063 (12)	−0.006 (6)	−0.024 (10)	−0.049 (10)
C6	0.035 (5)	0.020 (8)	0.036 (10)	−0.005 (6)	−0.021 (8)	−0.002 (7)
C7	0.034 (6)	0.041 (11)	0.063 (13)	−0.003 (7)	−0.022 (10)	−0.026 (9)
C1	0.045 (9)	0.025 (9)	0.036 (11)	−0.006 (6)	−0.029 (10)	−0.001 (8)
O1	0.055 (8)	0.042 (9)	0.078 (12)	−0.003 (7)	−0.048 (9)	−0.017 (9)
N2	0.038 (9)	0.058 (11)	0.058 (12)	−0.004 (7)	−0.020 (10)	−0.035 (10)
Re1	0.0231 (5)	0.0225 (5)	0.0241 (5)	−0.0092 (4)	−0.0066 (4)	−0.0067 (3)
Se1	0.0295 (10)	0.0214 (10)	0.0309 (10)	−0.0061 (8)	−0.0095 (9)	−0.0081 (8)
Se2	0.0341 (10)	0.0341 (10)	0.0341 (10)	−0.0130 (6)	−0.0130 (6)	−0.0130 (6)
C11	0.030 (5)	0.022 (7)	0.031 (4)	−0.012 (6)	−0.005 (4)	−0.010 (3)
N11	0.037 (11)	0.030 (9)	0.049 (11)	−0.019 (8)	0.006 (10)	−0.017 (8)
C8	0.079 (10)	0.135 (14)	0.104 (17)	−0.028 (9)	−0.049 (13)	−0.058 (14)
C9	0.075 (7)	0.133 (13)	0.141 (19)	−0.023 (11)	−0.045 (11)	−0.081 (16)

Calculated distances and angles for (EDT-TTF-CONH$_2$)$_6$[Re$_6$Se$_8$(CN)$_6$] at 0.4 GPa

Distances (Å)					
S1—C2	1.71 (2)	C2—C3	1.38 (2)	Re1—Se1i	2.6420 (13)
S1—C4	1.75 (2)	C4—C5	1.35 (3)	Re1—Se1ii	2.6281 (10)
S2—C2	1.731 (19)	C6—C7	1.28 (3)	Re1—Re1ii	2.6281 (10)
S2—C5	1.70 (2)	C6—C1	1.50 (2)	Re1—Re1iii	2.511 (2)
S3—C3	1.742 (19)	C7—H71	0.953	Re1—Re1i	2.520 (2)
S3—C6	1.774 (19)	C8—C9	1.24 (2)	Re1—Re1iv	2.081 (17)
S4—C3	1.73 (2)	C8—H81	1.32 (3)	Re1—Se1	1.20 (2)
S4—C7	1.726 (19)	C8—H82	0.959	Re1—Se2	1.504 (18)
S5—C4	1.75 (2)	C1—O1	0.949	Re1—C11	0.996

S5—C8	1.785 (16)	C1—N2	2.524 (2)	C11—N11	0.950
S6—C5	1.74 (2)	N2—H21	2.5237 (18)	C9—H91	0.998
S6—C9	1.780 (16)	N2—H22	2.6420 (13)	C9—H92	0.970

Angles (°)

C2—S1—C4	96.0 (10)	C1—N2—H22	119.2	Re1i—Re1—C11	135.2 (5)
C2—S2—C5	93.0 (9)	H21—N2—H22	90.24 (5)	Re1iii—Re1—C11	135.7 (5)
C3—S3—C6	93.7 (10)	Se1i—Re1—Se1ii	58.12 (5)	Re1ii—Re1—C11	134.3 (5)
C3—S4—C7	103.2 (12)	Se1i—Re1—Re1i	118.12 (5)	Re1iv—Re1—Se1	58.76 (4)
C4—S5—C8	98.0 (12)	Se1ii—Re1—Re1i	118.12 (5)	Re1iv—Re1—Se2	118.19 (4)
C5—S6—C9	115.2 (10)	Se1i—Re1—Re1iii	118.43 (5)	Se1—Re1—Se2	89.64 (5)
S2—C2—S1	121.5 (16)	Se1ii—Re1—Re1iii	60.000	Re1iv—Re1—C11	134.8 (5)
S2—C2—C3	123.3 (15)	Re1i—Re1—Re1iii	58.62 (4)	Se1—Re1—C11	91.8 (6)
S1—C2—C3	116.3 (10)	Se1i—Re1—Re1ii	58.31 (5)	Se2—Re1—C11	92.6 (5)
S3—C3—S4	122.1 (16)	Se1ii—Re1—Re1ii	59.82 (2)	Re1iii—Se1—Re1iv	62.75 (5)
S3—C3—C2	121.5 (15)	Re1i—Re1—Re1ii	90.000	Re1iii—Se1—Re1	63.29 (6)
S4—C3—C2	112.8 (14)	Re1iii—Re1—Re1ii	118.95 (5)	Re1iv—Se1—Re1	62.93 (5)
S1—C4—S5	115.9 (16)	Se1i—Re1—Re1iv	58.63 (5)	Re1—Se2—Re1iii	63.24 (6)
S1—C4—C5	131.0 (16)	Se1ii—Re1—Re1iv	90.000	Re1—Se2—Re1i	63.24 (6)
S5—C4—C5	117.6 (15)	Re1iii—Re1—Re1iv	59.82 (2)	Re1iii—Se2—Re1i	63.24 (6)
S6—C5—S2	124.9 (17)	Re1ii—Re1—Re1iv	60.35 (3)	Re1—C11—N11	175.5 (18)
S6—C5—C4	117.2 (16)	Se1i—Re1—Se1	176.47 (6)	S5—C8—C9	115.6 (17)
S2—C5—C4	117.1 (14)	Se1ii—Re1—Se1	90.52 (5)	S5—C8—H81	107.2
S3—C6—C7	119.5 (15)	Re1i—Re1—Se1	118.58 (5)	C9—C8—H81	105.2
S3—C6—C1	123.4 (17)	Re1iii—Re1—Se1	58.58 (5)	S5—C8—H82	109.7
C7—C6—C1	119.9 (15)	Re1ii—Re1—Se1	119.10 (5)	C9—C8—H82	109.8
S4—C7—C6	119.3	Se1i—Re1—Se2	89.36 (5)	H81—C8—H82	109.1
S4—C7—H71	120.7	Se1ii—Re1—Se2	175.90 (6)	C8—C9—S6	117 (2)
C6—C7—H71	116.5 (19)	Re1i—Re1—Se2	58.38 (3)	C8—C9—H91	106.5
C6—C1—O1	119.3 (16)	Re1iii—Re1—Se2	58.38 (3)	S6—C9—H91	107.5
C6—C1—N2	124.2 (17)	Re1ii—Re1—Se2	118.19 (4)	C8—C9—H92	109.3
O1—C1—N2	120.0	Se1i—Re1—C11	91.6 (6)	S6—C9—H92	108.8
C1—N2—H21	120.8	Se1ii—Re1—C11	91.5 (5)	H91—C9—H92	107.4

Fractional atomic coordinates and isotropic or equivalent isotropic displacement parameters (Å^2) for (EDT-TTF-CONH$_2$)$_6$[Re$_6$Se$_8$(CN)$_6$] at 0.8 GPa

Atom	*x*	*y*	*z*	*U*iso*/*U*eq
Re1	−0.0205 (3)	0.0697 (2)	−0.1035 (7)	0.0310 (9)*
Re2	−0.1744 (3)	−0.0836 (2)	−0.0645 (7)	0.0274 (9)*
Re3	0.0215 (3)	0.1093 (3)	0.0870 (7)	0.0310 (10)*
Se1	0.1638 (8)	0.2504 (7)	0.0441 (17)	0.040 (2)*
Se2	−0.1663 (8)	0.0909 (7)	−0.0774 (17)	0.036 (2)*
Se3	−0.2058 (9)	−0.1163 (7)	−0.2402 (19)	0.043 (2)*
Se4	0.1287 (9)	0.0419 (7)	−0.1192 (18)	0.041 (2)*
C111	−0.034 (9)	0.162 (7)	−0.212 (7)	0.05 (2)*
N111	−0.067 (12)	0.170 (12)	−0.298 (5)	0.14 (5)*
C112	−0.367 (4)	−0.180 (4)	−0.119 (12)	0.023 (16)*
N112	−0.475 (4)	−0.228 (4)	−0.163 (12)	0.039 (17)*
C113	0.051 (7)	0.226 (6)	0.202 (6)	0.04 (2)*
N113	0.075 (5)	0.298 (4)	0.261 (6)	0.037 (16)*
S11	0.5642 (8)	0.7237 (8)	0.4536 (8)	0.037 (5)*
S21	0.3117 (8)	0.5250 (8)	0.2838 (7)	0.044 (6)*
S31	0.6830 (9)	0.5777 (10)	0.4850 (8)	0.041 (5)*
S41	0.4244 (11)	0.3826 (8)	0.3229 (9)	0.045 (6)*
S51	0.4705 (12)	0.8586 (9)	0.4527 (9)	0.059 (7)*
S61	0.1766 (11)	0.6336 (11)	0.2572 (10)	0.054 (6)*
C11	0.7815 (14)	0.4442 (14)	0.520 (3)	0.029 (18)*
O11	0.755 (2)	0.351 (3)	0.469 (5)	0.07 (2)*
N21	0.893 (2)	0.530 (3)	0.605 (5)	0.030 (15)*
C21	0.4728 (8)	0.5842 (8)	0.3780 (7)	0.014 (14)*
C31	0.5232 (9)	0.5249 (8)	0.3910 (6)	0.05 (2)*
C41	0.4347 (9)	0.7337 (8)	0.3899 (7)	0.04 (2)*
C51	0.3189 (9)	0.6449 (9)	0.3127 (7)	0.05 (2)*
C61	0.6701 (12)	0.4531 (11)	0.4664 (9)	0.026 (17)*
C71	0.5502 (13)	0.3681 (10)	0.3918 (10)	0.04 (2)*
C81	0.3310 (15)	0.8590 (13)	0.3684 (18)	0.06 (3)*
C91	0.2441 (13)	0.7741 (13)	0.2569 (15)	0.06 (3)*
S12	0.3777 (14)	0.5323 (15)	0.0998 (11)	0.046 (6)*
S22	0.5016 (15)	0.7107 (14)	0.0287 (11)	0.045 (6)*
S32	0.6112 (15)	0.5010 (14)	0.1975 (12)	0.047 (6)*
S42	0.7187 (14)	0.6713 (15)	0.1095 (13)	0.044 (6)*
S52	0.153 (2)	0.534 (2)	0.0152 (15)	0.067 (8)*

S62	0.303 (2)	0.7572 (19)	−0.0682 (14)	0.072 (8)*
C12	0.821 (9)	0.482 (8)	0.275 (12)	0.08 (4)*
O12	0.921 (5)	0.511 (4)	0.279 (10)	0.038 (14)*
N22	0.755 (6)	0.392 (5)	0.294 (11)	0.043 (18)*
C22	0.5055 (18)	0.6109 (14)	0.0899 (11)	0.024 (16)*
C32	0.5977 (18)	0.5932 (14)	0.1277 (10)	0.04 (2)*
C42	0.306 (3)	0.600 (2)	0.0370 (10)	0.04 (2)*
C52	0.3601 (18)	0.683 (2)	0.0039 (12)	0.06 (3)*
C62	0.7529 (17)	0.535 (4)	0.217 (3)	0.06 (3)*
C72	0.801 (5)	0.613 (3)	0.1767 (15)	0.035 (19)*
C82	0.091 (8)	0.617 (7)	−0.029 (11)	0.07 (3)*
C92	0.167 (8)	0.702 (7)	−0.063 (11)	0.05 (2)*
S13	0.7359 (10)	0.8901 (7)	0.2734 (17)	0.046 (6)*
S23	0.7586 (10)	0.9751 (7)	0.4708 (17)	0.032 (5)*
S33	0.9091 (12)	0.8015 (8)	0.4163 (19)	0.044 (6)*
S43	0.9386 (11)	0.9024 (9)	0.6107 (18)	0.054 (7)*
S53	0.6095 (9)	0.9882 (10)	0.1430 (18)	0.078 (9)*
S63	0.6238 (9)	1.0828 (7)	0.364 (2)	0.051 (6)*
C13	1.079 (2)	0.7417 (19)	0.548 (2)	0.023 (17)*
N23	1.080 (4)	0.713 (4)	0.462 (3)	0.048 (19)*
O13	1.124 (4)	0.721 (3)	0.642 (3)	0.052 (17)*
C23	0.7953 (10)	0.9065 (7)	0.4113 (17)	0.026 (17)*
C33	0.8662 (10)	0.8689 (6)	0.4695 (17)	0.10 (4)*
C43	0.6636 (8)	0.9584 (6)	0.2647 (17)	0.05 (2)*
C53	0.6708 (8)	0.9966 (6)	0.3524 (18)	0.05 (2)*
C63	1.0143 (12)	0.7982 (9)	0.539 (2)	0.04 (2)*
C73	1.0229 (12)	0.8453 (10)	0.624 (2)	0.04 (2)*
C83	0.522 (2)	1.043 (2)	0.142 (2)	0.05 (2)*
C93	0.4889 (13)	1.0170 (15)	0.224 (2)	0.16 (7)*
H711	0.5332	0.2955	0.3777	0.0455*
H811	0.3529	0.9300	0.3604	0.0319*
H812	0.2889	0.8421	0.4056	0.0319*
H911	0.1755	0.7817	0.2130	0.0761*
H912	0.2906	0.7866	0.2242	0.0761*
H721	0.8781	0.6332	0.1835	0.0612*
H821	0.1273	0.6764	0.0333	0.0470*
H822	0.0001	0.5759	−0.0692	0.0470*
H921	0.1427	0.7531	−0.0741	0.0560*

H922	0.1190	0.6450	−0.1310	0.0560*
H731	1.0807	0.8504	0.6961	0.0391*
H831	0.5756	1.1217	0.1615	0.0805*
H832	0.4466	1.0131	0.0701	0.0805*
H931	0.4354	1.0411	0.2152	0.1491*
H932	0.4432	0.9384	0.2079	0.1491*

Calculated distances and angles for $(EDT\text{-}TTF\text{-}CONH_2)_6[Re_6Se_8(CN)_6]$ at 0.8 GPa.

Distances (Å)					
Re1—Re3i	2.626 (4)	S51—C41	1.740 (5)	C42—C52	1.341 (9)
Re1—Re2i	2.617 (8)	S51—C81	1.800 (6)	C62—C72	0.963
Re1—Re2	2.613 (8)	S61—C51	1.739 (6)	C72—H721	1.499 (9)
Re1—Re3	2.565 (12)	S61—C91	1.799 (6)	C82—C92	0.964
Re1—Se1	2.493 (13)	C11—O11	1.330 (9)	C82—H821	0.959
Re1—Se2	2.493 (11)	C11—N21	1.339 (6)	C82—H822	0.957
Re1—Se3	2.488 (12)	C11—C61	1.498 (6)	C92—H921	0.963
Re1—Se4	2.513 (10)	C21—C31	1.348 (6)	C92—H922	1.741 (5)
Re1—C111	2.110 (9)	C41—C51	1.341 (5)	S13—C23	1.739 (5)
Re2—Se1i	2.530 (10)	C61—C71	1.341 (5)	S13—C43	1.739 (5)
Re2—Re3i	2.603 (5)	C71—H711	0.959	S23—C23	1.740 (5)
Re2—Se4i	2.45 (3)	C81—C91	1.500 (6)	S23—C53	1.744 (5)
Re2—Re3	2.631 (6)	C81—H811	0.955	S33—C33	1.741 (5)
Re2—Se2	2.512 (10)	C81—H812	0.963	S33—C63	1.743 (5)
Re2—Se3	2.41 (3)	C91—H911	0.956	S43—C33	1.737 (5)
Re2—C112	2.111 (9)	C91—H912	0.964	S43—C73	1.738 (6)
Re3—Se4i	2.505 (16)	S12—C22	1.737 (9)	S53—C43	1.799 (6)
Re3—Se3i	2.485 (17)	S12—C42	1.739 (9)	S53—C83	1.742 (6)
Re3—Se1	2.479 (16)	S22—C22	1.738 (9)	S63—C53	1.800 (6)
Re3—Se2	2.505 (16)	S22—C52	1.740 (9)	S63—C93	1.339 (6)
Re3—C113	2.111 (9)	S32—C32	1.738 (9)	C13—N23	1.330 (9)
C111—N111	1.151 (9)	S32—C62	1.740 (9)	C13—O13	1.498 (6)
C112—N112	1.151 (9)	S42—C32	1.738 (9)	C13—C63	1.346 (6)
C113—N113	1.151 (9)	S42—C72	1.738 (9)	C23—C33	1.341 (5)
S11—C21	1.742 (5)	S52—C42	1.80 (5)	C43—C53	1.340 (5)
S11—C41	1.738 (5)	S52—C82	1.799 (9)	C63—C73	0.954

S21—C21	1.739 (5)	S62—C52	1.740 (9)	C73—H731	1.501 (6)
S21—C51	1.740 (5)	S62—C92	1.799 (9)	C83—C93	0.958
S31—C31	1.744 (5)	C12—O12	1.28 (10)	C83—H831	0.956
S31—C61	1.743 (5)	C12—N22	1.340 (9)	C83—H832	0.961

Angles (°)

Re3i—Re1—Re2i	60.24 (17)	Re1—C111—N111	153 (13)
Re3i—Re1—Re2	59.58 (15)	Re2—C112—N112	169 (12)
Re2i—Re1—Re2	90.9 (3)	Re3—C113—N113	173 (9)
Re3i—Re1—Re3	90.1 (3)	C21—S11—C41	93.05 (8)
Re2i—Re1—Re3	60.3 (2)	C21—S21—C51	95.32 (8)
Re2—Re1—Re3	61.1 (3)	C31—S31—C61	97.23 (8)
Re3i—Re1—Se1	119.5 (4)	C31—S41—C71	92.12 (8)
Re2i—Re1—Se1	59.3 (3)	C41—S51—C81	105.96 (9)
Re2—Re1—Se1	119.8 (6)	C51—S61—C91	93.19 (9)
Re3—Re1—Se1	58.7 (5)	O11—C11—N21	128.22 (9)
Re3i—Re1—Se2	118.4 (4)	O11—C11—C61	112.86 (9)
Re2i—Re1—Se2	119.7 (6)	N21—C11—C61	118.80 (9)
Re2—Re1—Se2	58.9 (3)	S11—C21—S21	116.28 (7)
Re3—Re1—Se2	59.4 (5)	S11—C21—C31	122.31 (7)
Se1—Re1—Se2	90.1 (4)	S21—C21—C31	121.41 (7)
Re3i—Re1—Se3	58.1 (4)	S41—C31—S31	115.45 (7)
Re2i—Re1—Se3	118.3 (4)	S41—C31—C21	120.00 (8)
Re2—Re1—Se3	56.2 (6)	S31—C31—C21	124.14 (8)
Re3—Re1—Se3	117.3 (5)	S51—C41—S11	112.54 (8)
Se1—Re1—Se3	175.8 (8)	S51—C41—C51	126.46 (8)
Re3i—Re1—Se4	58.3 (3)	S11—C41—C51	120.19 (8)
Re2i—Re1—Se4	56.9 (6)	S21—C51—S61	117.81 (8)
Re2—Re1—Se4	117.9 (4)	S21—C51—C41	115.16 (8)
Re3—Re1—Se4	117.2 (6)	S61—C51—C41	126.16 (8)
Se1—Re1—Se4	89.7 (4)	C11—C61—S31	123.71 (9)
Re3i—Re1—C111	139 (3)	C11—C61—C71	124.28 (9)
Re2i—Re1—C111	132 (2)	S31—C61—C71	111.79 (8)
Re2—Re1—C111	137 (2)	S41—C71—C61	123.41 (8)
Re3—Re1—C111	131 (3)	S41—C71—H711	118.7
Se1—Re1—C111	86 (3)	C61—C71—H711	117.9
Se2—Re1—Se3	88.4 (4)	S51—C81—C91	111.37 (9)
Se2—Re1—Se4	175.9 (8)	S51—C81—H811	111.2
Se3—Re1—Se4	91.5 (4)	C91—C81—H811	108.9

Se2—Re1—C111	90 (2)	S51—C81—H812	106.5
Se3—Re1—C111	98 (3)	C91—C81—H812	109.9
Se4—Re1—C111	94 (2)	H811—C81—H812	109.0
Se1i—Re2—Re1i	57.9 (4)	C81—C91—S61	114.08 (9)
Se1i—Re2—Re1	118.2 (3)	C81—C91—H911	108.5
Re1i—Re2—Re1	89.1 (3)	S61—C91—H911	107.4
Se1i—Re2—Re3i	57.8 (3)	C81—C91—H912	109.0
Re1i—Re2—Re3i	58.8 (3)	S61—C91—H912	107.9
Re1—Re2—Re3i	60.46 (16)	H911—C91—H912	109.9
Se1i—Re2—Se4i	90.3 (6)	C22—S12—C42	93.9 (20)
Re1i—Re2—Se4i	59.4 (3)	C22—S22—C52	97.5 (16)
Re1—Re2—Se4i	117.5 (3)	C32—S32—C62	95 (3)
Re3i—Re2—Se4i	118.2 (4)	C32—S42—C72	94 (3)
Se1i—Re2—Re3	118.0 (4)	C42—S52—C82	110 (3)
Re1i—Re2—Re3	60.06 (17)	C52—S62—C92	97 (3)
Re1—Re2—Re3	58.5 (2)	O12—C12—N22	125 (6)
Re3i—Re2—Re3	89.15 (18)	O12—C12—C62	117 (7)
Se4i—Re2—Re3	59.0 (3)	N22—C12—C62	116 (7)
Se1i—Re2—Se2	175.5 (3)	S22—C22—S12	114.5 (17)
Re1i—Re2—Se2	118.3 (4)	S22—C22—C32	124.6 (17)
Re1—Re2—Se2	58.2 (3)	S12—C22—C32	120.9 (18)
Re3i—Re2—Se2	118.6 (4)	S42—C32—S32	115.6 (18)
Se4i—Re2—Se2	89.4 (6)	S42—C32—C22	118.1 (17)
Se1i—Re2—Se3	90.2 (6)	S32—C32—C22	126.3 (18)
Re1i—Re2—Se3	118.2 (3)	S52—C42—S12	110 (2)
Re1—Re2—Se3	59.3 (3)	S52—C42—C52	128 (2)
Re3i—Re2—Se3	59.3 (3)	S12—C42—C52	121 (3)
Se4i—Re2—Se3	176.5 (3)	S22—C52—S62	116.9 (19)
Se1i—Re2—C112	89.8 (19)	S22—C52—C42	113 (3)
Re1i—Re2—C112	129 (4)	S62—C52—C42	129.9 (19)
Re1—Re2—C112	142 (4)	C12—C62—S32	124 (5)
Re3i—Re2—C112	137 (2)	C12—C62—C72	120 (4)
Se4i—Re2—C112	85 (4)	S32—C62—C72	117 (5)
Re3—Re2—Se2	58.2 (4)	S42—C72—C62	118 (5)
Re3—Re2—Se3	117.8 (4)	S42—C72—H721	121.9
Se2—Re2—Se3	89.8 (6)	C62—C72—H721	119.9
Re3—Re2—C112	133 (3)	S52—C82—C92	109 (5)
Se2—Re2—C112	94.7 (18)	S52—C82—H821	110.4

Se3—Re2—C112	98 (4)	C92—C82—H821	88.3
Se4i—Re3—Re2	56.8 (5)	S52—C82—H822	113.7
Se4i—Re3—Re1i	58.6 (2)	C92—C82—H822	123.6
Re2—Re3—Re1i	59.71 (18)	H821—C82—H822	109.2
Se4i—Re3—Se3i	91.8 (6)	C82—C92—S62	143 (6)
Re2—Re3—Se3i	117.9 (3)	C82—C92—H921	107.9
Re1i—Re3—Se3i	58.2 (2)	S62—C92—H921	107.5
Se4i—Re3—Re2i	118.5 (3)	C82—C92—H922	88.1
Re2—Re3—Re2i	90.85 (18)	S62—C92—H922	88.1
Re1i—Re3—Re2i	59.97 (18)	H921—C92—H922	110.0
Se3i—Re3—Re2i	56.4 (5)	C23—S13—C43	93.05 (8)
Se4i—Re3—Re1	117.2 (5)	C23—S23—C53	95.31 (8)
Re2—Re3—Re1	60.4 (2)	C33—S33—C63	97.25 (8)
Re1i—Re3—Re1	89.9 (3)	C33—S43—C73	92.11 (8)
Se3i—Re3—Re1	117.2 (5)	C43—S53—C83	105.95 (9)
Re2i—Re3—Re1	60.8 (2)	C53—S63—C93	93.20 (9)
Se4i—Re3—Se1	176.4 (7)	N23—C13—O13	128.22 (9)
Re2—Re3—Se1	119.6 (6)	N23—C13—C63	118.80 (9)
Re1i—Re3—Se1	119.6 (3)	O13—C13—C63	112.87 (9)
Se3i—Re3—Se1	89.5 (5)	S13—C23—S23	116.29 (7)
Re2i—Re3—Se1	59.6 (2)	S13—C23—C33	122.31 (7)
Se4i—Re3—Se2	88.3 (5)	S23—C23—C33	121.41 (7)
Re2—Re3—Se2	58.5 (3)	S33—C33—S43	115.43 (7)
Re1i—Re3—Se2	118.2 (3)	S33—C33—C23	124.10 (8)
Se3i—Re3—Se2	175.4 (5)	S43—C33—C23	119.96 (8)
Re2i—Re3—Se2	119.7 (5)	S13—C43—S53	112.53 (8)
Se4i—Re3—C113	89 (3)	S13—C43—C53	120.19 (7)
Re2—Re3—C113	135.2 (20)	S53—C43—C53	126.45 (8)
Re1i—Re3—C113	129 (3)	S63—C53—S23	117.81 (8)
Se3i—Re3—C113	88 (3)	S63—C53—C43	126.16 (8)
Re2i—Re3—C113	133.1 (19)	S23—C53—C43	115.15 (8)
Re1—Re3—Se1	59.2 (5)	C13—C63—S33	123.73 (8)
Re1—Re3—Se2	58.9 (4)	C13—C63—C73	124.31 (8)
Se1—Re3—Se2	90.2 (5)	S33—C63—C73	111.81 (7)
Re1—Re3—C113	141 (3)	S43—C73—C63	123.40 (8)
Se1—Re3—C113	95 (3)	S43—C73—H731	118.0
Se2—Re3—C113	97 (3)	C63—C73—H731	118.6
Re2i—Se1—Re1	62.8 (3)	S53—C83—C93	111.37 (9)

Re2i—Se1—Re3	62.6 (3)	S53—C83—H831	107.4
Re1—Se1—Re3	62.1 (3)	C93—C83—H831	108.6
Re2—Se2—Re3	63.3 (4)	S53—C83—H832	109.6
Re2—Se2—Re1	63.0 (2)	C93—C83—H832	109.8
Re3—Se2—Re1	61.7 (3)	H831—C83—H832	109.9
Re1—Se3—Re3i	63.8 (4)	C83—C93—S63	114.08 (9)
Re1—Se3—Re2	64.5 (5)	C83—C93—H931	108.5
Re3i—Se3—Re2	64.3 (6)	S63—C93—H931	107.9
Re1—Se4—Re3i	63.1 (3)	C83—C93—H932	107.9
Re1—Se4—Re2i	63.7 (5)	S63—C93—H932	109.0
Re3i—Se4—Re2i	64.2 (6)	H931—C93—H932	109.4

Symmetry codes: (i) −*x*, −*y*, −*z*.

Fractional atomic coordinates and isotropic or equivalent isotropic displacement parameters (Å^2) for at (EDT-TTF-CONH$_2$)$_6$[Re$_6$Se$_8$(CN)$_6$] 1.2 GPa.

Atom	*x*	*y*	*z*	*U*iso*/*U*eq
Re1	−0.02071 (19)	0.06980 (17)	−0.1035 (7)	*U*iso*/*U*eq
Re2	−0.17418 (19)	−0.08385 (17)	−0.0645 (7)	0.0275 (6)*
Re3	0.02199 (19)	0.10943 (17)	0.0870 (7)	0.0263 (6)*
Se1	0.1654 (5)	0.2508 (4)	0.0441 (17)	0.0269 (6)*
Se2	−0.1655 (5)	0.0926 (4)	−0.0774 (17)	0.0313 (13)*
Se3	−0.2071 (5)	−0.1149 (5)	−0.2402 (19)	0.0339 (14)*
Se4	0.1271 (5)	0.0418 (4)	−0.1192 (18)	0.0369 (14)*
C111	−0.040 (6)	0.147 (5)	−0.212 (7)	0.0336 (13)*
N111	−0.059 (4)	0.178 (4)	−0.298 (5)	0.06 (2)*
C112	−0.3740 (11)	−0.175 (3)	−0.119 (12)	0.039 (12)*
N112	−0.478 (3)	−0.231 (3)	−0.163 (12)	0.024 (11)*
C113	0.055 (4)	0.234 (3)	0.202 (6)	0.038 (11)*
N113	0.074 (3)	0.312 (3)	0.261 (6)	0.023 (11)*
S11	0.5644 (6)	0.7242 (6)	0.4536 (8)	0.027 (10)*
S21	0.3118 (6)	0.5246 (6)	0.2838 (7)	0.033 (3)*
S31	0.6843 (7)	0.5786 (6)	0.4850 (8)	0.038 (4)*
S41	0.4251 (7)	0.3823 (6)	0.3229 (9)	0.031 (3)*
S51	0.4699 (9)	0.8592 (7)	0.4527 (9)	0.038 (4)*
S61	0.1767 (8)	0.6335 (8)	0.2557 (8)	0.058 (5)*
C11	0.7820 (11)	0.4437 (11)	0.525 (2)	0.041 (14)*
O11	0.7542 (16)	0.3492 (18)	0.483 (4)	0.058 (12)*

N21	0.8916 (19)	0.527 (2)	0.614 (3)	0.047 (13)*
C21	0.4730 (6)	0.5844 (5)	0.3784 (6)	0.023 (11)*
C31	0.5236 (6)	0.5252 (5)	0.3911 (5)	0.047 (15)*
C41	0.4345 (7)	0.7339 (6)	0.3918 (5)	0.049 (16)*
C51	0.3191 (6)	0.6448 (6)	0.3144 (5)	0.058 (18)*
C61	0.6714 (8)	0.4538 (8)	0.4670 (8)	0.049 (16)*
C71	0.5515 (9)	0.3685 (7)	0.3937 (8)	0.018 (10)*
C81	0.3319 (11)	0.8600 (11)	0.3667 (16)	0.058 (18)*
C91	0.2473 (10)	0.7745 (10)	0.2559 (14)	0.07 (2)*
S12	0.3776 (10)	0.5324 (11)	0.1045 (10)	0.049 (4)*
S22	0.5011 (11)	0.7091 (11)	0.0310 (10)	0.048 (4)*
S32	0.6119 (11)	0.5031 (11)	0.1938 (11)	0.048 (4)*
S42	0.7204 (10)	0.6731 (11)	0.1069 (11)	0.045 (4)*
S52	0.1484 (12)	0.5309 (13)	0.0123 (12)	0.051 (4)*
S62	0.7539 (13)	0.537 (2)	0.2131 (17)	0.030 (12)*
C12	0.804 (3)	0.615 (2)	0.1737 (11)	0.048 (16)*
O12	0.108 (6)	0.622 (5)	−0.050 (6)	0.09 (3)*
N22	0.140 (3)	0.692 (5)	−0.117 (5)	0.09 (3)*
C22	0.7357 (8)	0.8884 (6)	0.2792 (11)	0.043 (4)*
C32	0.7627 (8)	0.9791 (6)	0.4772 (11)	0.037 (3)*
C42	0.9116 (9)	0.8023 (6)	0.4238 (12)	0.037 (3)*
C52	0.9402 (8)	0.9033 (7)	0.6173 (12)	0.038 (4)*
C62	0.6111 (8)	0.9879 (7)	0.1474 (12)	0.066 (5)*
C72	0.6236 (8)	1.0829 (6)	0.3687 (13)	0.045 (4)*
C82	1.0839 (18)	0.7449 (17)	0.5568 (15)	0.053 (17)*
C92	1.086 (3)	0.716 (3)	0.4716 (19)	0.051 (14)*
S13	1.129 (3)	0.727 (2)	0.6481 (19)	0.057 (12)*
S23	0.7974 (9)	0.9078 (7)	0.4176 (11)	0.027 (12)*
S33	0.8682 (8)	0.8698 (5)	0.4762 (11)	0.057 (18)*
S43	0.6666 (7)	0.9600 (5)	0.2702 (11)	0.07 (2)*
S53	0.6745 (7)	0.9995 (5)	0.3583 (12)	0.026 (12)*
S63	1.0146 (10)	0.7974 (8)	0.5468 (13)	0.029 (12)*
C13	1.0233 (10)	0.8450 (8)	0.6308 (13)	0.032 (13)*
N23	0.521 (2)	1.0398 (18)	0.1459 (15)	0.07 (2)*
O13	0.4889 (11)	1.0136 (13)	0.2284 (14)	0.047 (16)*
C23	0.5346	0.2959	0.3795	0.0455*
C33	0.3537	0.9311	0.3589	0.0319*
C43	0.2895	0.8428	0.4037	0.0319*

C53	0.7539 (13)	0.537 (2)	0.2131 (17)	0.030 (12)*
C63	0.804 (3)	0.615 (2)	0.1737 (11)	0.048 (16)*
C73	0.108 (6)	0.622 (5)	−0.050 (6)	0.09 (3)*
C83	0.140 (3)	0.692 (5)	−0.117 (5)	0.09 (3)*
C93	0.7357 (8)	0.8884 (6)	0.2792 (11)	0.043 (4)*
H711	0.7627 (8)	0.9791 (6)	0.4772 (11)	0.037 (3)*
H811	0.9116 (9)	0.8023 (6)	0.4238 (12)	0.037 (3)*
H812	0.9402 (8)	0.9033 (7)	0.6173 (12)	0.038 (4)*
H911	0.1787	0.7820	0.2120	0.0761*
H912	0.2940	0.7872	0.2233	0.0761*
H721	0.8813	0.6358	0.1806	0.0612*
H821	0.1440	0.6809	0.0118	0.0470*
H822	0.0169	0.5806	−0.0910	0.0470*
H921	0.1154	0.7435	−0.1280	0.0560*
H922	0.0918	0.6357	−0.1852	0.0560*
H731	1.0809	0.8500	0.7027	0.0391*
H831	0.5746	1.1186	0.1658	0.0805*
H832	0.4457	1.0101	0.0741	0.0805*
H931	0.4353	1.0376	0.2199	0.1491*
H932	0.4432	0.9349	0.2123	0.1491*

Calculated distances and angles for $(EDT\text{-}TTF\text{-}CONH_2)_6[Re_6Se_8(CN)_6]$ at 1.2 GPa.

Distances (Å)					
Re1—Re3i	2.622 (3)	S41—C31	1.745 (5)	C12—O12	1.21 (4)
Re1—Re2i	2.619 (5)	S41—C71	1.737 (5)	C12—N22	1.337 (10)
Re1—Re2	2.642 (5)	S51—C41	1.747 (6)	C12—C62	1.495 (10)
Re1—Re3	2.634 (7)	S51—C81	1.796 (6)	C22—C32	1.341 (9)
Re1—Se1	2.519 (7)	S61—C51	1.733 (6)	C42—C52	1.341 (9)
Re1—Se2	2.520 (6)	S61—C91	1.801 (6)	C62—C72	1.342 (10)
Re1—Se3	2.509 (7)	C11—O11	1.279 (9)	C72—H721	0.962
Re1—Se4	2.533 (5)	C11—N21	1.340 (7)	C82—C92	1.501 (10)
Re1—C111	2.109 (10)	C11—C61	1.499 (7)	C82—H821	0.964
Re2—Se4i	2.522 (14)	C21—C31	1.348 (6)	C82—H822	0.959
Re2—Se1i	2.512 (7)	C41—C51	1.342 (5)	C92—H921	0.956
Re2—Re3i	2.626 (3)	C61—C71	1.339 (5)	C92—H922	0.964
Re2—Re3	2.641 (3)	C71—H711	0.958	S13—C23	1.742 (5)
Re2—Se2	2.531 (7)	C81—C91	1.501 (7)	S13—C43	1.738 (5)

Re2—Se3	2.545 (14)	C81—H811	0.954	S23—C23	1.743 (5)
Re2—C112	2.113 (9)	C81—H812	0.963	S23—C53	1.739 (5)
Re3—Se3i	2.535 (11)	C91—H911	0.955	S33—C33	1.742 (5)
Re3—Se4i	2.531 (10)	C91—H912	0.964	S33—C63	1.740 (5)
Re3—Se1	2.496 (10)	S12—C22	1.738 (9)	S43—C33	1.744 (5)
Re3—Se2	2.521 (11)	S12—C42	1.736 (9)	S43—C73	1.732 (5)
Re3—C113	2.110 (9)	S22—C22	1.737 (9)	S53—C43	1.743 (6)
C111—N111	1.149 (10)	S22—C52	1.742 (9)	S53—C83	1.797 (6)
C112—N112	1.153 (9)	S32—C32	1.740 (9)	S63—C53	1.743 (6)
C113—N113	1.148 (9)	S32—C62	1.742 (9)	S63—C93	1.802 (6)
S11—C21	1.742 (5)	S42—C32	1.736 (9)	C13—N23	1.337 (7)
S11—C41	1.740 (5)	S42—C72	1.742 (10)	C13—O13	1.280 (10)
S21—C21	1.737 (5)	S52—C42	1.81 (3)	C13—C63	1.497 (7)
S21—C51	1.740 (5)	S52—C82	1.802 (10)	C23—C33	1.351 (6)
S31—C31	1.748 (5)	S62—C52	1.740 (9)	C43—C53	1.346 (5)
S31—C61	1.742 (5)	S62—C92	1.800 (10)	C63—C73	1.336 (6)

Angles (°)

Re3i—Re1—Re2i	60.52 (11)	Re1—C111—N111	173 (7)
Re3i—Re1—Re2	59.86 (10)	Re2—C112—N112	165 (7)
Re2i—Re1—Re2	90.25 (17)	Re3—C113—N113	166 (7)
Re3i—Re1—Re3	90.13 (17)	C21—S11—C41	93.17 (8)
Re2i—Re1—Re3	59.99 (14)	C21—S21—C51	95.15 (8)
Re2—Re1—Re3	60.07 (15)	C31—S31—C61	97.20 (8)
Re3i—Re1—Se1	119.0 (3)	C31—S41—C71	92.17 (9)
Re2i—Re1—Se1	58.5 (2)	C41—S51—C81	105.17 (9)
Re2—Re1—Se1	118.0 (3)	C51—S61—C91	92.51 (10)
Re3—Re1—Se1	57.9 (3)	O11—C11—N21	128.07 (10)
Re3i—Re1—Se2	118.5 (3)	O11—C11—C61	112.70 (10)
Re2i—Re1—Se2	118.5 (4)	N21—C11—C61	119.09 (10)
Re2—Re1—Se2	58.7 (2)	S11—C21—S21	116.36 (7)
Re3—Re1—Se2	58.5 (3)	S11—C21—C31	122.29 (8)
Se1—Re1—Se2	89.1 (2)	S21—C21—C31	121.35 (8)
Re3i—Re1—Se3	59.2 (2)	S31—C31—S41	115.27 (8)
Re2i—Re1—Se3	119.7 (2)	S31—C31—C21	124.14 (9)
Re2—Re1—Se3	59.1 (3)	S41—C31—C21	120.11 (9)
Re3—Re1—Se3	119.2 (3)	S51—C41—S11	112.90 (9)
Se1—Re1—Se3	177.0 (5)	S51—C41—C51	126.72 (9)
Re3i—Re1—Se4	58.8 (2)	S11—C41—C51	119.74 (8)
Re2i—Re1—Se4	58.6 (3)	S21—C51—S61	117.47 (9)
Re2—Re1—Se4	118.6 (2)	S21—C51—C41	115.57 (8)

Re3—Re1—Se4	118.6 (3)	S61—C51—C41	126.34 (9)
Se1—Re1—Se4	90.58 (19)	C11—C61—S31	123.99 (8)
Re3^{i}—Re1—C111	132.7 (19)	C11—C61—C71	124.12 (8)
Re2^{i}—Re1—C111	133.0 (17)	S31—C61—C71	111.86 (8)
Re2—Re1—C111	136.7 (18)	S41—C71—C61	123.49 (8)
Re3—Re1—C111	137.1 (18)	S41—C71—H711	118.4
Se1—Re1—C111	92.4 (20)	C61—C71—H711	118.1
Se2—Re1—Se3	89.9 (2)	S51—C81—C91	111.50 (10)
Se2—Re1—Se4	176.6 (5)	S51—C81—H811	111.9
Se3—Re1—Se4	90.26 (19)	C91—C81—H811	109.6
Se2—Re1—C111	94.5 (16)	S51—C81—H812	104.2
Se3—Re1—C111	90.5 (20)	C91—C81—H812	110.5
Se4—Re1—C111	88.9 (16)	H811—C81—H812	109.1
Se4^{i}—Re2—Re1	118.48 (19)	C81—C91—S61	114.48 (10)
Se4^{i}—Re2—Se1^{i}	91.0 (4)	C81—C91—H911	107.3
Re1—Re2—Se1^{i}	117.75 (19)	S61—C91—H911	106.3
Se4^{i}—Re2—Re3^{i}	119.3 (2)	C81—C91—H912	109.8
Re1—Re2—Re3^{i}	59.69 (11)	S61—C91—H912	109.0
Se1^{i}—Re2—Re3^{i}	58.1 (2)	H911—C91—H912	109.8
Se4^{i}—Re2—Re1^{i}	58.99 (18)	C22—S12—C42	93.6 (14)
Re1—Re2—Re1^{i}	89.75 (17)	C22—S22—C52	97.0 (12)
Se1^{i}—Re2—Re1^{i}	58.8 (2)	C32—S32—C62	94.9 (17)
Re3^{i}—Re2—Re1^{i}	60.29 (15)	C32—S42—C72	95.6 (17)
Se4^{i}—Re2—Re3	58.66 (18)	C42—S52—C82	98 (2)
Re1—Re2—Re3	59.82 (15)	C52—S62—C92	111 (2)
Se1^{i}—Re2—Re3	118.5 (2)	O12—C12—N22	123 (4)
Re3^{i}—Re2—Re3	89.89 (10)	O12—C12—C62	118 (4)
Re1^{i}—Re2—Re3	59.79 (11)	N22—C12—C62	118 (3)
Se4^{i}—Re2—Se2	89.6 (3)	S12—C22—S22	114.9 (12)
Re1—Re2—Se2	58.3 (2)	S12—C22—C32	125.5 (14)
Se1^{i}—Re2—Se2	175.57 (17)	S22—C22—C32	119.6 (14)
Re3^{i}—Re2—Se2	117.9 (2)	S32—C32—S42	115.1 (13)
Re1^{i}—Re2—Se2	118.1 (2)	S32—C32—C22	121.6 (14)
Se4^{i}—Re2—Se3	176.20 (18)	S42—C32—C22	123.2 (14)
Re1—Re2—Se3	57.8 (2)	S52—C42—S12	110.7 (15)
Se1^{i}—Re2—Se3	90.3 (3)	S52—C42—C52	127.6 (15)
Re3^{i}—Re2—Se3	58.70 (18)	S12—C42—C52	121 (2)
Re1^{i}—Re2—Se3	118.95 (17)	S22—C52—S62	116.3 (13)
Se4^{i}—Re2—C112	97 (2)	S22—C52—C42	113.3 (18)
Re1—Re2—C112	129 (2)	S62—C52—C42	129.8 (14)
Se1^{i}—Re2—C112	94.5 (14)	C12—C62—S32	123 (2)
Re3^{i}—Re2—C112	132.3 (15)	C12—C62—C72	118 (2)

Re1^{i}—Re2—C112	141 (2)	S32—C62—C72	118 (3)
Re3—Re2—Se2	58.3 (2)	S42—C72—C62	116 (3)
Re3—Re2—Se3	117.6 (2)	S42—C72—H721	122.5
Se2—Re2—Se3	88.8 (4)	C62—C72—H721	121.0
Re3—Re2—C112	137.2 (12)	S52—C82—C92	136 (5)
Se2—Re2—C112	89.7 (14)	S52—C82—H821	102.7
Se3—Re2—C112	86 (2)	C92—C82—H821	97.3
Se3^{i}—Re3—Se4^{i}	89.7 (3)	S52—C82—H822	105.2
Se3^{i}—Re3—Re2	117.88 (17)	C92—C82—H822	104.0
Se2—Re1—Se4	176.6 (5)	S51—C81—H811	111.9
Se4^{i}—Re3—Re2	58.3 (3)	H821—C82—H822	109.2
Se3^{i}—Re3—Re1	118.7 (2)	C82—C92—S62	109 (4)
Se4^{i}—Re3—Re1	118.4 (3)	C82—C92—H921	117.3
Re2—Re3—Re1	60.11 (14)	S62—C92—H921	112.5
Se3^{i}—Re3—Re2^{i}	59.0 (3)	C82—C92—H922	100.1
Se4^{i}—Re3—Re2^{i}	119.29 (16)	S62—C92—H922	106.7
Re2—Re3—Re2^{i}	90.11 (10)	H921—C92—H922	109.9
Re1—Re3—Re2^{i}	59.72 (14)	C23—S13—C43	93.20 (8)
Se3^{i}—Re3—Re1^{i}	58.19 (15)	C23—S23—C53	95.07 (8)
Se4^{i}—Re3—Re1^{i}	58.85 (14)	C33—S33—C63	97.21 (8)
Re2—Re3—Re1^{i}	59.69 (11)	C33—S43—C73	92.19 (8)
Re1—Re3—Re1^{i}	89.87 (17)	C43—S53—C83	105.16 (9)
Re2^{i}—Re3—Re1^{i}	60.45 (11)	C53—S63—C93	92.53 (10)
Se3^{i}—Re3—Se1	90.9 (3)	N23—C13—O13	128.08 (10)
Se4^{i}—Re3—Se1	176.9 (3)	N23—C13—C63	119.08 (10)
Re2—Re3—Se1	118.9 (3)	O13—C13—C63	112.70 (10)
Re1—Re3—Se1	58.7 (3)	S23—C23—S13	116.35 (7)
Re2^{i}—Re3—Se1	58.66 (14)	S23—C23—C33	121.41 (8)
Se3^{i}—Re3—Se2	176.1 (2)	S13—C23—C33	122.24 (8)
Se4^{i}—Re3—Se2	89.6 (3)	S43—C33—S33	115.25 (8)
Re2—Re3—Se2	58.67 (16)	S43—C33—C23	120.14 (9)
Re1—Re3—Se2	58.5 (2)	S33—C33—C23	124.09 (9)
Re2^{i}—Re3—Se2	118.2 (3)	S53—C43—S13	112.89 (8)
Se3^{i}—Re3—C113	88.7 (15)	S53—C43—C53	126.76 (9)
Se4^{i}—Re3—C113	91.5 (16)	S13—C43—C53	119.77 (8)
Re2—Re3—C113	137.2 (10)	S63—C53—S23	117.51 (8)
Re1—Re3—C113	137.5 (19)	S63—C53—C43	126.38 (8)
Re2^{i}—Re3—C113	132.6 (10)	S23—C53—C43	115.55 (8)
Re1^{i}—Re3—Se1	119.11 (14)	C13—C63—S33	123.99 (8)
Re1^{i}—Re3—Se2	118.35 (16)	C13—C63—C73	124.13 (8)
Se1—Re3—Se2	89.6 (3)	S33—C63—C73	111.87 (7)
Re1^{i}—Re3—C113	132.6 (19)	S43—C73—C63	123.48 (8)

Se1—Re3—C113	91.5 (16)	S43—C73—H731	118.1
Se2—Re3—C113	95.2 (15)	C63—C73—H731	118.4
Re1—Se1—Re2^{i}	62.75 (16)	S53—C83—C93	111.49 (10)
Re1—Se1—Re3	63.4 (2)	S53—C83—H831	106.2
Re2^{i}—Se1—Re3	63.3 (2)	C93—C83—H831	108.5
Re2—Se2—Re3	63.0 (2)	S53—C83—H832	110.0
Re2—Se2—Re1	63.07 (15)	C93—C83—H832	110.6
Re3—Se2—Re1	63.00 (19)	H831—C83—H832	109.9
Re2—Se3—Re3^{i}	62.3 (3)	C83—C93—S63	114.48 (10)
Re2—Se3—Re1	63.0 (3)	C83—C93—H931	107.9
Re3^{i}—Se3—Re1	62.6 (2)	S63—C93—H931	106.6
Re1—Se4—Re3^{i}	62.4 (2)	C83—C93—H932	107.8
Re1—Se4—Re2^{i}	62.4 (2)	S63—C93—H932	110.6

Symmetry codes: (i) −*x*, −*y*, −*z*.

Fractional atomic coordinates and isotropic or equivalent isotropic displacement parameters (Å^2) for (EDT-TTF-CONH$_2$)$_6$[Re$_6$Se$_8$(CN)$_6$] at 1.8 GPa

Atom	*x*	*y*	*z*	*U*iso*/*U*eq
Re1	−0.0198 (2)	0.07209 (17)	−0.1049 (4)	0.0213 (7)*
Re2	−0.1754 (2)	−0.08442 (17)	−0.0636 (4)	0.0213 (7)*
Re3	0.0224 (2)	0.10915 (17)	0.0941 (4)	0.0209 (7)*
Se1	0.1678 (6)	0.2538 (4)	0.0527 (11)	0.0276 (15)*
Se2	−0.1651 (6)	0.0929 (4)	−0.0693 (11)	0.0268 (14)*
Se3	−0.2100 (6)	−0.1151 (5)	−0.2564 (11)	0.0280 (15)*
Se4	0.1314 (6)	0.0454 (5)	−0.1257 (11)	0.0287 (15)*
C111	−0.027 (9)	0.178 (7)	−0.201 (7)	0.08 (3)*
N111	−0.056 (8)	0.171 (6)	−0.290 (6)	0.09 (3)*
C112	−0.372 (3)	−0.183 (3)	−0.126 (9)	0.024 (13)*
N112	−0.481 (2)	−0.237 (3)	−0.168 (8)	0.039 (14)*
C113	0.058 (6)	0.238 (5)	0.204 (6)	0.040 (17)*
N113	0.080 (4)	0.307 (4)	0.268 (4)	0.037 (13)*
S11	0.5622 (6)	0.7256 (5)	0.4469 (7)	0.027 (3)*
S21	0.3050 (7)	0.5204 (6)	0.2864 (7)	0.030 (4)*
S31	0.6806 (7)	0.5769 (6)	0.4818 (7)	0.029 (4)*
S41	0.4195 (8)	0.3779 (6)	0.3270 (8)	0.031 (4)*
S51	0.4669 (9)	0.8630 (7)	0.4463 (7)	0.042 (4)*
S61	0.1692 (9)	0.6308 (8)	0.2571 (8)	0.045 (5)*
C11	0.7813 (11)	0.4430 (10)	0.520 (2)	0.032 (15)*

O11	0.7537 (16)	0.3488 (18)	0.478 (4)	0.021 (9)*
N21	0.8946 (18)	0.530 (2)	0.605 (4)	0.020 (10)*
C21	0.4685 (6)	0.5823 (5)	0.3765 (7)	0.028 (14)*
C31	0.5192 (7)	0.5225 (5)	0.3905 (5)	0.036 (16)*
C41	0.4303 (7)	0.7343 (5)	0.3853 (5)	0.046 (18)*
C51	0.3125 (7)	0.6424 (6)	0.3112 (5)	0.036 (16)*
C61	0.6686 (9)	0.4514 (8)	0.4666 (8)	0.023 (13)*
C71	0.5471 (10)	0.3644 (7)	0.3950 (8)	0.035 (15)*
C81	0.3234 (11)	0.8598 (11)	0.3649 (18)	0.028 (14)*
C91	0.2342 (11)	0.7712 (10)	0.2530 (15)	0.07 (2)*
S12	0.3761 (13)	0.5361 (12)	0.1036 (11)	0.044 (5)*
S22	0.4991 (13)	0.7087 (11)	0.0272 (10)	0.037 (4)*
S32	0.6095 (13)	0.5014 (11)	0.1995 (11)	0.041 (4)*
S42	0.7205 (12)	0.6719 (10)	0.1092 (11)	0.030 (4)*
S52	0.1492 (18)	0.5381 (16)	0.0153 (13)	0.064 (6)*
S62	0.3093 (18)	0.7625 (15)	−0.0663 (12)	0.071 (7)*
C12	0.808 (7)	0.469 (5)	0.249 (8)	0.07 (2)*
O12	0.922 (3)	0.515 (3)	0.292 (6)	0.020 (8)*
N22	0.752 (4)	0.389 (3)	0.285 (7)	0.024 (11)*
C22	0.5054 (16)	0.6114 (12)	0.0924 (10)	0.020 (12)*
C32	0.5999 (15)	0.5955 (11)	0.1306 (9)	0.012 (11)*
C42	0.300 (2)	0.6006 (16)	0.0375 (9)	0.019 (12)*
C52	0.3570 (15)	0.6825 (17)	0.0038 (11)	0.022 (13)*
C62	0.7499 (15)	0.535 (3)	0.214 (2)	0.012 (11)*
C72	0.803 (3)	0.612 (2)	0.1740 (12)	0.049 (19)*
C82	0.110 (6)	0.634 (4)	−0.038 (6)	0.044 (18)*
C92	0.144 (3)	0.686 (5)	−0.113 (6)	0.048 (19)*
S13	0.7314 (8)	0.8862 (6)	0.2745 (11)	0.032 (4)*
S23	0.7623 (9)	0.9819 (6)	0.4761 (11)	0.030 (4)*
S33	0.9103 (9)	0.8022 (6)	0.4200 (12)	0.034 (4)*
S43	0.9446 (9)	0.9105 (7)	0.6168 (12)	0.030 (4)*
S53	0.6080 (8)	0.9880 (8)	0.1442 (12)	0.056 (5)*
S63	0.6233 (8)	1.0863 (6)	0.3679 (13)	0.038 (4)*
C13	1.081 (2)	0.7416 (18)	0.5518 (16)	0.032 (15)*
N23	1.096 (4)	0.723 (3)	0.471 (2)	0.050 (16)*
O13	1.119 (3)	0.719 (3)	0.640 (2)	0.064 (15)*
C23	0.7968 (9)	0.9095 (7)	0.4153 (11)	0.036 (16)*
C33	0.8690 (8)	0.8728 (5)	0.4740 (11)	0.046 (19)*

C43	0.6614 (7)	0.9582 (5)	0.2667 (11)	0.06 (2)*
C53	0.6708 (7)	0.9995 (5)	0.3562 (12)	0.06 (2)*
C63	1.0176 (10)	0.8007 (8)	0.5438 (14)	0.029 (14)*
C73	1.0287 (10)	0.8516 (9)	0.6300 (13)	0.034 (15)*
C83	0.522 (2)	1.0460 (19)	0.1439 (16)	0.07 (2)*
C93	0.4871 (12)	1.0203 (14)	0.2263 (15)	0.13 (5)*
H711	0.5301	0.2918	0.3808	0.0455*
H811	0.3453	0.9308	0.3571	0.0319*
H812	0.2811	0.8425	0.4019	0.0319*
H911	0.1655	0.7788	0.2092	0.0761*
H912	0.2808	0.7839	0.2205	0.0761*
H721	0.8800	0.6326	0.1809	0.0612*
H821	0.1459	0.6926	0.0243	0.0470*
H822	0.0189	0.5922	−0.0784	0.0470*
H921	0.1194	0.7375	−0.1247	0.0560*
H922	0.0958	0.6296	−0.1818	0.0560*
H731	1.0863	0.8566	0.7018	0.0391*
H831	0.5752	1.1248	0.1638	0.0805*
H832	0.4463	1.0163	0.0721	0.0805*
H931	0.4335	1.0443	0.2178	0.1491*
H932	0.4414	0.9416	0.2103	0.1491*

Calculated distances and angles for $(EDT\text{-}TTF\text{-}CONH_2)_6[Re_6Se_8(CN)_6]$ at 1.8 GPa.

Distances (Å)					
Re1—Re3i	2.622 (6)	S41—C31	1.742 (5)	C12—O12	1.21 (6)
Re1—Re2i	2.621 (3)	S41—C71	1.738 (5)	C12—N22	1.339 (10)
Re1—Re2	2.646 (6)	S51—C41	1.752 (5)	C12—C62	1.499 (10)
Re1—Re3	2.650 (8)	S51—C81	1.800 (7)	C22—C32	1.343 (9)
Re1—Se1	2.530 (7)	S61—C51	1.735 (6)	C42—C52	1.342 (10)
Re1—Se2	2.526 (8)	S61—C91	1.802 (6)	C62—C72	1.343 (10)
Re1—Se3	2.545 (7)	C11—O11	1.262 (9)	C72—H721	0.950
Re1—Se4	2.535 (7)	C11—N21	1.339 (7)	C82—C92	1.500 (10)
Re1—C111	2.110 (10)	C11—C61	1.497 (7)	C82—H821	0.950
Re2—Se4i	2.518 (7)	C21—C31	1.344 (6)	C82—H822	0.950
Re2—Se1i	2.505 (16)	C41—C51	1.346 (5)	C92—H921	0.950
Re2—Re3i	2.620 (4)	C61—C71	1.341 (5)	C92—H922	0.950

Re2—Re3	2.639 (4)	C71—H711	0.950	S13—C23	1.743 (5)
Re2—Se2	2.510 (7)	C81—C91	1.503 (6)	S13—C43	1.743 (5)
Re2—Se3	2.600 (16)	C81—H811	0.950	S23—C23	1.735 (5)
Re2—C112	2.109 (9)	C81—H812	0.950	S23—C53	1.737 (5)
Re3—Se3i	2.563 (11)	C91—H911	0.950	S33—C33	1.737 (5)
Re3—Se4i	2.529 (11)	C91—H912	0.950	S33—C63	1.739 (5)
Re3—Se1	2.489 (11)	S12—C22	1.800 (7)	S43—C33	1.741 (5)
Re3—Se2	2.499 (11)	S12—C42	1.735 (6)	S43—C73	1.738 (5)
Re3—C113	2.108 (10)	S22—C22	1.739 (9)	S53—C43	1.743 (6)
C111—N111	1.151 (10)	S22—C52	1.739 (9)	S53—C83	1.803 (6)
C112—N112	1.152 (10)	S32—C32	1.739 (9)	S63—C53	1.735 (6)
C113—N113	1.150 (10)	S32—C62	1.739 (9)	S63—C93	1.801 (6)
S11—C21	1.746 (5)	S42—C32	1.738 (9)	C13—N23	1.336 (7)
S11—C41	1.743 (5)	S42—C72	1.737 (9)	C13—O13	1.259 (10)
S21—C21	1.737 (5)	S52—C42	1.739 (9)	C13—C63	1.498 (7)
S21—C51	1.736 (5)	S52—C82	1.738 (10)	C23—C33	1.344 (6)
S31—C31	1.736 (5)	S62—C52	1.75 (4)	C43—C53	1.341 (5)
S31—C61	1.741 (5)	S62—C92	1.801 (10)	C63—C73	1.341 (6)

Angles (°)

Re2i—Re1—Re3i	60.44 (11)	Re1—C111—N111	135 (9)
Re2i—Re1—Re2	89.72 (17)	Re2—C112—N112	174 (11)
Re3i—Re1—Re2	59.66 (11)	Re3—C113—N113	177 (7)
Re2i—Re1—Re3	59.59 (15)	C21—S11—C41	92.94 (8)
Re3i—Re1—Re3	89.81 (18)	C21—S21—C51	95.42 (8)
Re2—Re1—Re3	59.77 (17)	C31—S31—C61	97.64 (8)
Re2i—Re1—Se1	58.5 (2)	C31—S41—C71	92.33 (8)
Re3i—Re1—Se1	118.9 (3)	C41—S51—C81	106.12 (9)
Re2—Re1—Se1	117.1 (4)	C51—S61—C91	94.00 (10)
Re3—Re1—Se1	57.4 (3)	O11—C11—N21	127.70 (9)
Re2i—Re1—Se2	117.2 (4)	O11—C11—C61	113.15 (9)
Re3i—Re1—Se2	117.7 (3)	N21—C11—C61	119.09 (9)
Re2—Re1—Se2	58.0 (2)	S11—C21—S21	116.36 (7)
Re3—Re1—Se2	57.7 (3)	S11—C21—C31	122.29 (8)
Se1—Re1—Se2	88.4 (2)	S21—C21—C31	121.35 (8)
Re2i—Re1—Se3	119.9 (2)	S41—C31—S31	115.25 (8)
Re3i—Re1—Se3	59.5 (2)	S41—C31—C21	120.07 (8)
Re2—Re1—Se3	60.1 (3)	S31—C31—C21	124.26 (8)
Re3—Re1—Se3	119.9 (3)	S51—C41—S11	112.91 (9)

Se1—Re1—Se3	177.1 (5)	S51—C41—C51	126.39 (9)
Re2i—Re1—Se4	58.1 (3)	S11—C41—C51	119.88 (8)
Re3i—Re1—Se4	58.7 (2)	S21—C51—S61	117.74 (9)
Re2—Re1—Se4	118.3 (2)	S21—C51—C41	115.38 (8)
Re3—Re1—Se4	117.7 (3)	S61—C51—C41	126.03 (9)
Se1—Re1—Se4	90.6 (2)	C11—C61—S31	124.04 (9)
Re2i—Re1—C111	131 (3)	C11—C61—C71	124.20 (9)
Re3i—Re1—C111	144 (3)	S31—C61—C71	111.57 (8)
Re2—Re1—C111	138 (3)	S41—C71—C61	123.21 (8)
Re3—Re1—C111	126 (3)	S41—C71—H711	118.5
Se1—Re1—C111	84 (3)	C61—C71—H711	118.3
Se2—Re1—Se3	90.5 (2)	S51—C81—C91	110.89 (10)
Se2—Re1—Se4	174.9 (5)	S51—C81—H811	109.5
Se3—Re1—Se4	90.3 (2)	C91—C81—H811	110.1
Se2—Re1—C111	88 (3)	S51—C81—H812	108.6
Se3—Re1—C111	99 (3)	C91—C81—H812	108.3
Se4—Re1—C111	96 (3)	H811—C81—H812	109.5
Se1i—Re2—Re1	117.6 (2)	C81—C91—S61	113.85 (10)
Se1i—Re2—Se4i	91.5 (4)	C81—C91—H911	108.4
Re1—Re2—Se4i	119.0 (2)	S61—C91—H911	108.8
Se1i—Re2—Re1i	58.9 (2)	C81—C91—H912	107.6
Re1—Re2—Re1i	90.28 (17)	S61—C91—H912	108.7
Se4i—Re2—Re1i	59.2 (2)	H911—C91—H912	109.5
Se1i—Re2—Re3i	57.9 (2)	C22—S12—C42	95.8 (16)
Re1—Re2—Re3i	59.71 (12)	C22—S22—C52	97.7 (14)
Se4i—Re2—Re3i	119.9 (2)	C32—S32—C62	92.4 (18)
Re1i—Re2—Re3i	60.75 (16)	C32—S42—C72	94.7 (19)
Se1i—Re2—Re3	118.6 (3)	C42—S52—C82	100 (3)
Re1—Re2—Re3	60.20 (16)	C52—S62—C92	102 (3)
Se4i—Re2—Re3	58.83 (19)	O12—C12—N22	117 (5)
Re1i—Re2—Re3	59.77 (11)	O12—C12—C62	120 (5)
Re3i—Re2—Re3	90.09 (11)	N22—C12—C62	115 (5)
Se1i—Re2—Se2	175.6 (2)	S22—C22—S12	113.1 (14)
Re1—Re2—Se2	58.6 (2)	S22—C22—C32	123.9 (15)
Se4i—Re2—Se2	88.8 (4)	S12—C22—C32	123.0 (15)
Re1i—Re2—Se2	117.8 (2)	S42—C32—S32	117.1 (14)
Re3i—Re2—Se2	118.3 (3)	S42—C32—C22	118.7 (15)
Se1i—Re2—Se3	89.8 (4)	S32—C32—C22	124.2 (15)

Re1—Re2—Se3	58.0 (2)	S52—C42—S12	112.3 (17)
Se4i—Re2—Se3	177.1 (2)	S52—C42—C52	128.8 (17)
Re1i—Re2—Se3	119.54 (19)	S12—C42—C52	119 (2)
Re3i—Re2—Se3	58.81 (19)	S62—C52—S22	113.7 (15)
Se1i—Re2—C112	90.2 (16)	S62—C52—C42	131.6 (17)
Re1—Re2—C112	139 (3)	S22—C52—C42	115 (2)
Se4i—Re2—C112	87 (3)	C12—C62—S32	124 (4)
Re1i—Re2—C112	131 (3)	C12—C62—C72	114 (3)
Re3i—Re2—C112	135.9 (16)	S32—C62—C72	121 (3)
Re3—Re2—Se2	58.0 (2)	S42—C72—C62	115 (3)
Re3—Re2—Se3	118.2 (2)	S42—C72—H721	122.4
Se2—Re2—Se3	89.6 (4)	C62—C72—H721	122.4
Re3—Re2—C112	133.8 (19)	S52—C82—C92	123 (5)
Se2—Re2—C112	94.2 (16)	S52—C82—H821	106.8
Se3—Re2—C112	95 (3)	C92—C82—H821	107.0
Se3i—Re3—Se4i	90.1 (3)	S52—C82—H822	105.1
Se3i—Re3—Re1	119.8 (3)	C92—C82—H822	105.3
Se4i—Re3—Re1	118.0 (3)	H821—C82—H822	109.5
Se3i—Re3—Re2	118.58 (17)	C82—C92—S62	117 (5)
Se4i—Re3—Re2	57.9 (3)	C82—C92—H921	106.9
Re1—Re3—Re2	60.03 (16)	S62—C92—H921	107.0
Se3i—Re3—Re1i	58.79 (15)	C82—C92—H922	108.6
Se4i—Re3—Re1i	58.93 (15)	S62—C92—H922	107.5
Re1—Re3—Re1i	90.19 (18)	H921—C92—H922	109.5
Re2—Re3—Re1i	59.79 (12)	C23—S13—C43	92.96 (8)
Se3i—Re3—Re2i	60.2 (3)	C23—S23—C53	95.37 (8)
Se4i—Re3—Re2i	119.52 (17)	C33—S33—C63	97.66 (8)
Re1—Re3—Re2i	59.66 (16)	C33—S43—C73	92.33 (8)
Re2—Re3—Re2i	89.91 (11)	C43—S53—C83	106.13 (9)
Re1i—Re3—Re2i	60.64 (12)	C53—S63—C93	93.99 (10)
Se3i—Re3—Se1	91.4 (3)	N23—C13—O13	127.70 (9)
Se4i—Re3—Se1	176.8 (4)	N23—C13—C63	119.08 (9)
Re1—Re3—Se1	58.9 (3)	O13—C13—C63	113.15 (9)
Re2—Re3—Se1	118.9 (3)	S13—C23—S23	116.35 (7)
Re1i—Re3—Se1	119.63 (17)	S13—C23—C33	122.26 (8)
Se3i—Re3—Se2	176.95 (18)	S23—C23—C33	121.39 (8)
Se4i—Re3—Se2	88.5 (3)	S43—C33—S33	115.23 (8)
Re1—Re3—Se2	58.7 (3)	S43—C33—C23	120.07 (9)

Re2—Re3—Se2	58.42 (16)	S33—C33—C23	124.21 (9)
Re1i—Re3—Se2	118.21 (17)	S13—C43—S53	112.87 (9)
Se3i—Re3—C113	89 (2)	S13—C43—C53	119.88 (8)
Se4i—Re3—C113	94 (2)	S53—C43—C53	126.35 (9)
Re1—Re3—C113	135 (3)	S23—C53—S63	117.76 (9)
Re2—Re3—C113	138.3 (16)	S23—C53—C43	115.36 (8)
Re1i—Re3—C113	135 (3)	S63—C53—C43	125.99 (9)
Re2i—Re3—Se1	59.00 (16)	C13—C63—S33	124.04 (9)
Re2i—Re3—Se2	118.3 (3)	C13—C63—C73	124.21 (9)
Se1—Re3—Se2	89.9 (4)	S33—C63—C73	111.57 (8)
Re2i—Re3—C113	131.8 (16)	S43—C73—C63	123.21 (8)
Se1—Re3—C113	89 (2)	S43—C73—H731	118.5
Se2—Re3—C113	94 (2)	C63—C73—H731	118.3
Re1—Se1—Re2i	62.57 (16)	S53—C83—C93	110.89 (10)
Re1—Se1—Re3	63.7 (2)	S53—C83—H831	108.5
Re2i—Se1—Re3	63.1 (2)	S53—C83—H831	108.6
Re1—Se2—Re2	63.38 (16)	S53—C83—H832	109.5
Re1—Se2—Re3	63.7 (2)	C93—C83—H832	109.8
Re2—Se2—Re3	63.6 (2)	H831—C83—H832	109.5
Re2—Se3—Re3i	61.0 (3)	C83—C93—S63	113.84 (10)
Re2—Se3—Re1	61.9 (3)	C83—C93—H931	108.4
Re3i—Se3—Re1	61.7 (2)	S63—C93—H931	108.6
Re1—Se4—Re3i	62.3 (	C83—C93—H932	107.9
Re1—Se4—Re2i	62.7 (	S63—C93—H932	108.5
Re3i—Se4—Re2i	63.2 (	H931—C93—H932	109.5

Symmetry codes: (i) −*x*, −*y*, −*z*.

Appendix C

Publications arising from this thesis

"Neutron powder diffraction study of the crystal and magnetic structures of $BiNiO_3$ at low temperature" Sandra J. E. Carlsson, Masaki Azuma, Yuichi Shimakawa, Mikio Takano, Alan Hewat and J. Paul Attfield, *J. Solid State Chem.*, **181**, 611(2008).

"Pressure-Induced Intermetallic Valence Transition in $BiNiO_3$" Masaki Azuma, Sandra Carlsson, Jennifer Rodgers, Mathew G. Tucker, Masahiko Tsujimoto, Shintaro Ishiwata, Seiji Isoda, Yuichi Shimakawa, Mikio Takano and J. Paul Attfield, *J. Am. Chem. Soc.*, **129**, 14433 (2007).